University of São Paulo

Institute of Astronomy Geophysics and Atmospheric Sciences

Department of Atmospheric Sciences

José Leandro Pereira Silveira Campos

South America Last Millennium Precipitation Variability in the Little Ice Age and in the Medieval Climate Anomaly Periods Through Speleothems

Revised Version

The original is available at the unity

São Paulo

2019

José Leandro Pereira Silveira Campos

South America Last Millennium Precipitation Variability in the Little Ice Age and in the Medieval Climate Anomaly Periods Through Speleothems

Ph.D. Thesis presented to the Atmospheric Sciences Department of the Institute of Astronomy, Geophysics and Atmospheric Sciences of the University of São Paulo as a partial requirement to obtain the title of Doctor in Sciences.

Areas of Concentration: Atmospheric Sciences

Advisor: Prof. Dr. Tercio Ambrizzi

São Paulo

2019

Abstract

Campos, J.L.P.S. (2019). South America last millennium precipitation variability in the Little Ice Age and in the Medieval Climate Anomaly periods through speleothems (Ph.D. Thesis). Institute of Astronomy, Geophysics and Atmospheric Sciences, University of São Paulo.

In the last decades across the South America the number of last millennia paleoclimatic studies and isotopic time series rose substantially allowing the study of the paleo-precipitation on different sites along the Tropical South America or on the monsoon region. However, most of previous works studied the South American Monsoon System (SAMS) in a punctual or very localized region, just assessing the precipitation variability on the records' site. In this work a new approach is applied to eleven $\delta^{18}O$ isotopic and one Sr/Ca trace element paleoclimatic time series using Monte-Carlo Principal Component Analysis, accounting the uncertainty of the individual records. This approach allows us to reduce the set of 12 time series into a set of fewer physically significant variables. Just the two leading Principal Component Loadings were found physically and statistically significant. The 1st Principal Component mode representing 30±2% of the data variability, depicts the monsoon intensity variability, presenting a dipole between the South Atlantic Convergence Zone (SACZ) and the Andes region to the Northeast of Brazil (NEB) and Northern of Brazil. The 2nd Principal Component mode representing 13±1% of the data variability shows the South American Monsoon shape parameter, presenting a tripole between the Southeast south America (SESA), the SACZ domain and the NEB regions, coherent with the footprint of extreme South American Low Level Jets (SALLJ) episodes. Composite analysis based on a regime shift test based on sample means, reveals an enhanced monsoon during the early Little Ice Age (LIA) period with a monsoon axis or SACZ wider than in the Current Warm Period (CWP) and Mediaeval Climate Anomaly (MCA), rather than a southward SACZ displacement, contrasting to previous interpretations. The MCA period is found the driest period in all the South America domain except Eastern Amazonia region. Time series analysis suggest coupled behaviour between the 2nd Principal Component mode and the Atlantic Multidecadal Oscillation (AMO) during the MCA period and the Southern Annular Mode (SAM) during the Transitional Period (TRANS) between the MCA and LIA. Future efforts to sample paleoclimatic data over the continent, particularly over the Amazonia and the La Plata basin as well as over the ocean, where reliable paleoclimatic proxy time series is still scarce, is urgently needed to improve the South America last millennium climate variability understanding. A climate without anthropic forcings.

Keywords: South America Monsoon; Last Millennium; Paleoclimate; Speleothems; Climate Dynamics.

Resumo

Campos, J.L.P.S. (2019). Variabilidade da Precipitação sobre a América do Sul nos períodos da Pequena Idade do Gelo e Medieval através de espeleotemas (Tese de Doutorado). Instituto de Astronomia, Geofísica e Ciências Atmosféricas da Universidade de São Paulo.

Nas últimas décadas o número de estudos e registros paleoclimáticos teve um grande aumento, permitindo o estudo da paleo-precipitação sobre diferentes lugares da América do Sul tropical ou sobre a região das monções. Porém, maior parte dos estudos anteriores, mostram o Sistema de Monções da América do Sul de um modo muito pontual ou localizado, somente analisando a variabilidade da precipitação sobre a região onde o registro foi coletado. Neste trabalho uma nova abordagem é aplicada às 11 séries de tempo de isótopos estáveis de oxigênio ($\delta^{18}O$) e uma série de elementos traço (Sr/Ca), usando métodos de Monte-Carlo à Análise de Componentes Principais para levar em conta a incerteza de cada registro. Esta abordagem permite reduzir o conjunto de 12 variáveis em um conjunto de poucas variáveis com significado físico. Somente duas Componentes Principais foram achadas estatisticamente significativas e com interpretação física. A 1ª Componente Principal, representando 30±2%, da variabilidade dos dados, mostra a intensidade da monção, representando um dipolo entre as regiões de atuação da Zona de Convergência do Atlântico Sul (SACZ) e Andes com o Nordeste do Brasil (NEB). A 2ª Componente Principal, representando 13±1% da variabilidade, representa o parâmetro de forma da monção, mostrando um tripolo entre as regiões do Sudeste da América do Sul, com a região da SACZ, com o NEB, coerente com o padrão espacial de episódios extremos do Jato de Baixos Níveis da América do Sul (SALLJ). Análises de compostos baseadas em um teste de detecção de mudança de regime aplicados às Componentes Principais, levando em conta somente a média amostral, revela o eixo das monções ou SACZ espacialmente mais disperso durante a Pequena Idade do Gelo (LIA) que durante a Anomalia Climática Medieval (MCA) e que o Corrente Período Quente (CWP), ao invés de um deslocamento a sul da SACZ, contrastando com interpretações anteriores sobre a variabilidade da monção. O período MCA foi o período mais seco para toda a América do Sul exceto para o leste da Amazônia. Análise de séries de temporais sugere um comportamento acoplado ente a 2ª Componente Principal com a Oscilação Multidecenal do Atlântico Sul (AMO) durante o período MCA e com o Modo Anular Sul (SAM) durante o período Transacional (TRANS) entre o MCA e a LIA. Esforços para amostrar dados paleoclimático no continente, particularmente sobre regiões onde dados paleoclimáticos do último milênio são escassos como Amazônia e Bacia do Prata, assim como sobre os oceanos são necessários para

melhorar o entendimento da variabilidade climática do último milênio. Um clima sem forçantes antrópicas.

Palavras Chave: Monsões da América do Sul, Último Milênio, Paleoclimatologia, Espeleotemas, Dinâmica do Clima.

Acknowledgements

Foremost, I would like to express my sincere gratitude to my advisor Prof. Ambrizzi for the continuous support of my studies since of the undergraduation, for his patience, motivation, support and knowledge. His guidance helped me in all the time of research.

Besides my advisor, I would like to thank Prof. Francisco Cruz Jr, for his guidance, advices and by the paleoclimate, without his help and assistance, this thesis would not be possible.

I would not forget to thank the University of São Paulo for affording me the opportunity to complete my study, and the Conselho Nacional de Ciencia e Tecnologia (CNPQ) which granted me a scholarship during all the graduation period.

Finally, I would like to thank my family, my parents for giving birth to me at the first place and supporting me all these long years, and to our Lord Jesus Christ that allowed me to get here.

Summary

Chapter 1 - Introduction

Chapter 2 - Methods and Data sets

Chapter 3 - Monte-Carlo Principal Component Analysis and South America Isotopic Time Series

Figures List

Figure 3.4 – Multi-taper Power Density Estimate for the South America Climate Proxies. The blue curve represents the time series power density estimate, the heavy red line represents the theoretical red noise estimate, the cyan and the lighter red curves represent the 95% bounds of the time series and red noise estimates respectively. Only values above the red curve can be considered statistically significant at the level of 95% or different from the red noise.

Figure 3.5 – Speleothems $\delta^{18}O$ isotopic time series after the Monte-Carlo simulations. The blue and orange represent the time series before and after 30 years low pass filtering. The shaded around delimits the upper and low quartile

Figure 3.6 - Monte-Carlo Principal Component Eigenvalues Spectrum or Explained Variance. The vertical bars represent the explained variance, or the latent values and the error bars represent the inter-sample variability and the Monte-Carlo simulation dispersion as a measure of uncertainty.

Figure 3.7 - Monte-Carlo Principal Component Analysis - Loading coefficients boxplots. The box and whiskers represent the dispersion of the 1000 simulations. The greater is the box and the whiskers, the greater is the uncertainty of the loading.

Figure 3.8 - Monte-Carlo Principal Component Analysis Loading Coefficients Spatial Distribution. The size of the dots corresponds to the loading's magnitude, warm colours means positive loadings and colder, negative ones or $\delta^{18}O$ enrichment and impoverishment respectively. The magnitude of the loadings was computed through the extraction of the median of the 1000 Monte-Carlo simulations.

Figure 3.9 - Monte-Carlo Principal Component Scores or Time Series. The shaded around represents the upper and lower quartile of the Monte-Carlo Simulations and the heavy curves represent the median of the simulations.

Figure 4.10- Low Frequency South America Leading Variability Modes. The shaded represent the correlation of the Principal Component to the TCRW variable. The stream lines represent the correlation of the PC to the 850hPa circulation.

Figure 4.11 – Speleothems' Coherency, (a) 1st $PC_{\delta^{18}O}$ and 1st PC_{TCRW}, and (b)2nd $PC_{\delta^{18}O}$ and 3rd PC_{TCRW}. The dots as in the fig. 4.4 represent the $PC_{\delta^{18}O}$ loading magnitude with red and blue dots representing $\delta^{18}O$ enrichment and depletion respectively, and the shaded represent the PC_{TCRW} loading patterns represented here as the correlation between the Principal Component to the original gridded data. The yellow strips represent the South Atlantic Convergence Zone (SACZ), the Intertropical Convergence Zone (ITCZ) and the Low-Level Jet (LLJ).

Figure 5.19 - Empirical Mode Decomposition Analysis between the 2nd $PC_{\delta}{}^{18}O$ t and the SAM mode. (a) 2nd $PC_{\delta}{}^{18}O$, (b) SAM mode as in the Fig.5.1. (c) 2nd $PC_{\delta}{}^{18}O$ and SAM modes reconstructed with the first 3 IMFs and (d) reconstructed with the last 3 IMFs. The blue curve represents the 2nd $PC_{\delta}{}^{18}O$ and the orange one, the SAM mode. A figure showing all the IMFs separately is provided in the appendix XXX.

Figure 5.20 – Spectral analysis and Empirical Mode Decomposition between the 1st $PC_{\delta}{}^{18}O$ and the AMO time series. (a) Wavelet Coherence Analysis, between the 1st $PC_{\delta}{}^{18}O$ and AMO index, statistically significant values at the level of 95% are presented inside the contours, and the arrows indicate the phase angle between the signals. (b) 1st $PC_{\delta}{}^{18}O$, (c) AMO time series, (d) High frequency IMFs reconstruction and (e) Low frequency IMFs reconstruction. The green curves represent the 1st $PC_{\delta}{}^{18}O$ reconstruction and the brown curve is referent to the AMO reconstruction.

Fig. 6.1 – Biplot or scatter plot of the leading two Monte-Carlo Principal Component Analysis based on the proxy data. The x axis represents the monsoon activity mode and the y axis represent the tripole SESA-SACZ-NEB mode or simply the SESA mode. The roman algorisms represent the quadrants of the biplot. The periods studied are represented by the assorted colours as showed in the legend on the left side inside the figure.

Figure A.21 – LISAM, Large Scale South America Monson Index. (a) 1st LISAM mode, representing the monsoon precipitation, (b) 2nd LISAM mode, representing the SACZ-SESA precipitation pattern and (c) Explained Variance or Loadings latent values. The LISAM consists of the Principal Component of the low-level circulation, temperature, specific humidity and surface precipitation. Here the annual mean was taken through a 13-year running mean filter. da Silva et al. (2007) removed the annual component using just a linear trend.

Figure A.22 - Explained Variance for the TCRW principal component analysis, the error bars were computed through the North et al. (1982) rule of thumb.

Figure A.3 – Morlet Wavelet Analysis, the shaded inside the contour represent statistically significant values at the level of 95%. The light shaded represent the Cone of Influence. (a) 1st PC, (b) 2nd PC, (c) GeoB13814 sediment, (d)Cariaco Basin, (e) SAM, (f) NH temperatures and (g) ENSO variance

Figure A.4 -Wavelet Coherency Analysis, values inside the black contours, represent statistically significant values at the level of 95%, the arrows represent the leads and lags between the time series. Coherency between the 1stPC and (a) GeoB13413, (b) SAM, (c) Cariaco Basin, (d) AMO index, (e) Northern Hemisphere Temperature and (f) ENSO variance.

Figure A.5 -The same as to the fig. A.3.2 but for the 2ndPC.

Figure A.6 - Intrinsic Mode Functions for the 1st PC. The last component (bottom plot) represent the trend component and the others, the IMFs.

Tables List

Abbreviations List

AMO – Atlantic Multidecadal Oscillation

AMV – Atlantic Multidecadal Variability

CH – Chaco Low

BH - Bolivian High

CWP – Current Warm Period

ERA – European Reanalysis

CERA20C - Coupled European Reanalysis of 20th Century

CMIP – Coupled Modelling Intercomparison Project

ITCZ – Intertropical Convergence Zone

LGM – Last Glacial Maximum

LIA – Little Ice Age

MCA – Medieval Climate Anomaly

NT – Northeast Through

PMIP - Palaeoclimate Modelling Intercomparison Project

SACZ – South Atlantic Convergence Zone

SALLJ – South America Low-Level Jet

SESA – Southeast South America

SH – Subtropical High

TRANS – Transitional Period

Chapter I

Introduction

In tropical latitudes, during the summer, South America presents a low-level circulation flowing from the Tropical Atlantic Ocean towards the continent. As the flow come across the Andes, it changes its longitudinal orientation, becoming more meridional and parallel to the Andes, forming the South Atlantic Low-Level Jet, which brings moisture from low latitudes toward higher latitudes like a conveyor belt. The surface heating over the Amazonia and Central Brazil gives rise to the formation of the Chaco Low in the Northern of Argentina (Figueroa et al. 1995), where together to the moisture supply generates a northwest-southeastward convection-oriented band, extending from the east of Amazon towards the Brazilian southeast, the South Atlantic Convergence Zone, responsible by most of interannual precipitation over the Tropical South America, characterizing the South American Monsoon (Vuille et al. 2012; Carvalho et al. 2016).

In the last four decades, the South American Monsoon System (SAMS) dynamics and interannual variability were a widely studied issue, due to its importance in water supply and disasters, causing extreme precipitation events and extensive droughts. However, the shortness of meteorological station-based data (e.g. 40 years in an average sense), turn decadal to centennial climate variability studies difficult. So, indirect methods to study the monsoon, like paleoclimatic proxies' records, became a possibility just in the last two decades (after 2000's).

Nowadays there is an extensive network of paleoclimate records, paleo-precipitation proxies, across the tropical South America allowing studies of the SAMS from decadal to multi-centennial time scales. One of the motivations of the present work is to evaluate this type of study, through the compilation of paleo-precipitation proxies along the Tropical South America. In this chapter a brief review of the SAMS and its interannual variability is presented. A review of the monsoon variability in the last millennium, important climate events and climate proxies is discussed. The motivation and the objectives of the present study is shown at the end of this chapter.

1.1– The South American Monsoon System (SAMS)

1.1.1 – Global Monsoon Overview and Intertropical Convergence Zone (ITCZ)

Following the classical definitions of monsoons, during the summer, the different heat capacity of the upper ocean in relation to the adjacent land, as the land have lesser heat capacity than the ocean, the land warms faster during the summer which induces a low-level circulation from the ocean into the continent, carrying moisture, favouring convection and precipitation. During the winter the opposite is found, the circulation is completely reversed, flowing from the continent towards the ocean, do not favouring convection and precipitation. This reversal of circulation during the summer and winter characterizes the monsoon circulation.

The above definition applies just for some tropical regions (from 0° to ±30° latitude) around the globe, like the India, Oceania and Africa. The upper ocean to land temperature gradient in the South American Continent is not so intense to create this "giant breeze" with a complete reversal of the wind. Nevertheless, Zhou and Lau (1998) through the removal of the annual mean of the low-level (e.g. 850hPa) wind, observed a reversal in the wind anomaly field between the austral summer (DJF) and winter (JJA) seasons. Another characteristic of the monsoon is the formation of a thermal low inside the continent, in regions like the Asia, where a thermal low forms over the Indian continent which leads to a cyclonic circulation inducing precipitation (Zhou and Lau,

1998). In the South America, previous works before the decade of 1990 argue that due to the narrowness of the continent away from the equator can limit areas in which stationary lows/highs form, and the persistence of oceanic upwelling water along the west South America (SA) coast will limit the Sea Surface Temperature (SST) colder than the adjacent continental surface temperature (Ramage 1971, Zhou and Lau, 1998).

Developments in the observations and the advent of reanalysis, led researchers toward the importance of the thermal impact of the South America Plateau Altiplano (Rao and Erdogan, 1989). During the austral summer, over the Plateau Altiplano, a warm core upper-level (300 hPa) high develops and at lower-levels (850 hPa) over the Chaco region (North Argentina/Southern Bolivia) as a response of the Amazonia latent heat release, a thermal low forms (Silva-Dias et al, 1983), which together mid-latitudes disturbances on the Southeastern Brazil's coast, induces a circulation northwest-southeastward circulation pattern, carrying moisture from the Amazonia towards the South and Southeast of Brazil.

A more concise criterion to define a monsoon region is proposed by Wang and Ding (2006), who modified the DSI index, which is the evaluation of the difference between the summer minus the winter mean precipitation. If the difference is more than 2 mm/days, one can consider this region part of the monsoons. In Fig.1.1 the global monsoon domain is shown. One can see that there are various monsoon domains, in the Northern Hemisphere (NH), the Central-North America (Douglas et al. 1993), the Sahel, the Indian and Northeast Asian (Webster et al. 1998, Goswami et al 2003) domains. In the Southern Hemisphere (SH), it is observed the South America (Zhou and Lau 1998), Southern Africa (Ramage 1971) and Oceania (Ramage 1971) domains.

The global monsoons are intimately related to the Intertropical Convergence Zone (ITCZ) that can be defined as the region where the northerly and southerly easterlies or trade winds converge or the upward branch of the Hadley circulation. Cloudiness is observed in the ITCZ due to the upward motion and precipitation, where the maximum precipitation occurs as it can be seen in Fig.1.1, around the tropics. Comparing figs.1.1a, b, the seasonality of the monsoon is accompanied by the north-south ITCZ displacement. In interannual time scales, due to the obliquity of the ecliptic, the ITCZ follows the sun's path. During the boreal summer the maximum insolation is

located northward and during the austral summer, southward. However, as suggested by Walister and Gautier (1993), the ITCZ variability is distinct across the globe as observed on the Indian Ocean.

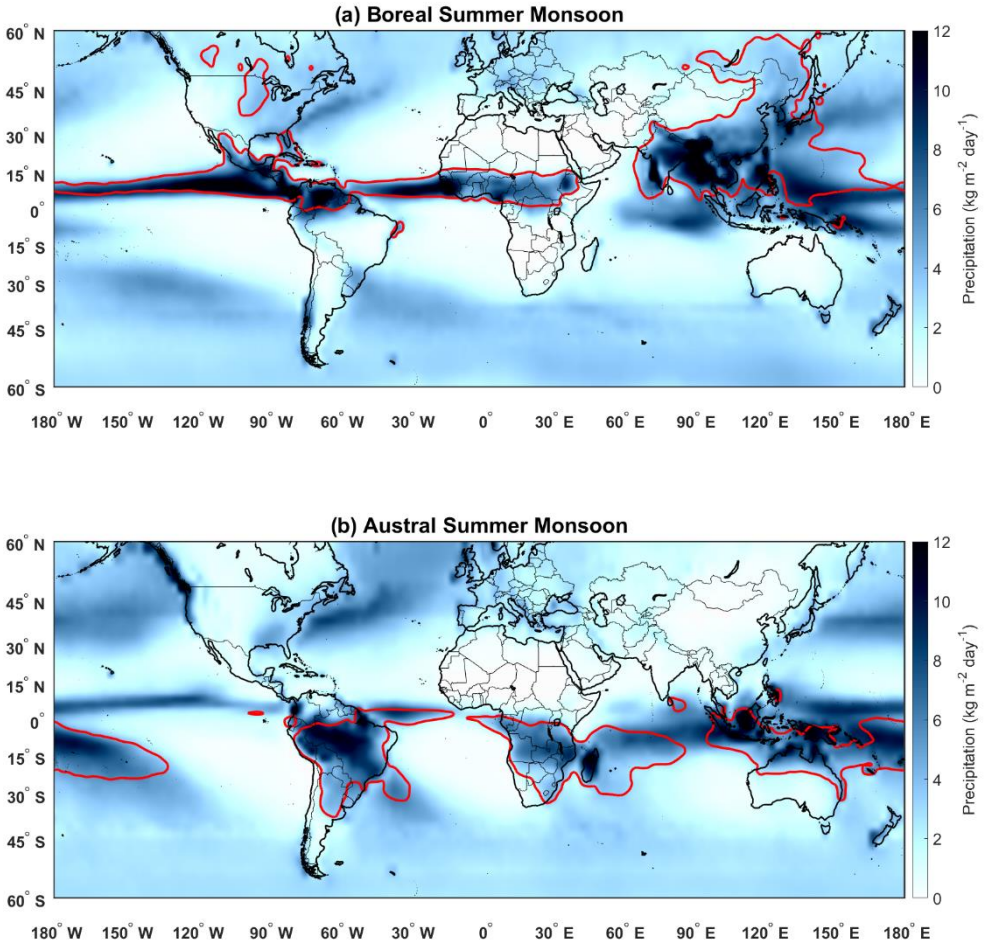

Figure 1.1 - Monsoon Domain *(a) Boreal and (b) Austral summer monsoon. The shaded represent the boreal summer (JJA) and the austral summer (DJF) precipitation, extracted from 30 years (1981-2010) GPCP precipitation data. The red area delimits the monsoon domain, defined as the summer minus winter precipitation above or equal to 2 mm/day.*

Aquaplanet experiments shows that to the onset of the monsoons the ITCZ passes from an equatorial trough regime, where the equatorial trade easterlies converge towards the ITCZ, to the monsoon trough regime, that is characterized by the low-level westerly wind field in the region of the ITCZ and a prominent cross-equatorial

flow (Chao, 2000). This change of regime is possible due to two balancing “forces” acting on the ITCZ, one toward the equator, which depends on the convection and earth’s rotation, and other toward the latitude where the Sea Surface Temperature (SST) peaks (Chao, 2000). In paleoclimate context (e.g. time scales longer than decadal) the mean ITCZ position is an indicative of the interhemispheric energy transport, which forces the ITCZ to migrate towards the relative warming hemisphere (Schneider et al. 2014).

Another feature to the monsoon circulation is the existence of the Subtropical Highs also known as subtropical anticyclones, consequence of the Hadley circulation descending branches. These semi-permanent weather systems are located over the ocean, and due to its anticyclonic circulation, they support easterly winds influencing the ITCZ intensity, location and the moisture supply into the continents.

1.1.2 – South America Summer Monsoon (SASM)

Over South America the monsoon begins on the mid to late austral spring during the months of October to November lasting up to the early to mid-austral autumn during the months of March and April (Gan et al. 2004; da Silva et al. 2007; Bombardi and Carvalho, 2009). To characterize the South American Monsoon System (SAMS) seasonality and variability, some authors such as da Silva et al. (2007) propose a monsoon index based on the low-level (e.g. 850hPa) circulation, specific humidity, temperature and precipitation, called Large Scale Index for South America Monsoon (LISAM), shown in appendix A.1 (fig. A.1.1).

The LISAM partition the SAMS into two modes, one representing the seasonality of the South America precipitation, called monsoonal mode and other representing the dipole Southeast-South America (SESA) – oceanic South Atlantic Convergence Zone (SACZ) mode. In Fig.1.2 the index or the time series corresponding to the seasonal component of the LISAM is presented. From the index, the mean duration of the monsoon is about 36 pentads (180 days) and the mean onset of the monsoon occur at the 58th pentad (16th October) and the mean demise at the 23rd pentad (16th April), with a dispersion of 3.5 and 3 pentads respectively, as shown by the figs1.2.b-d .

To depict the low and upper level circulation, fig.1.2e and f shows the upper and low-level circulation and the precipitation field for the mature phase of the SAMS, defined as the 1980 to 2010, December to February climatological wind and precipitation fields.

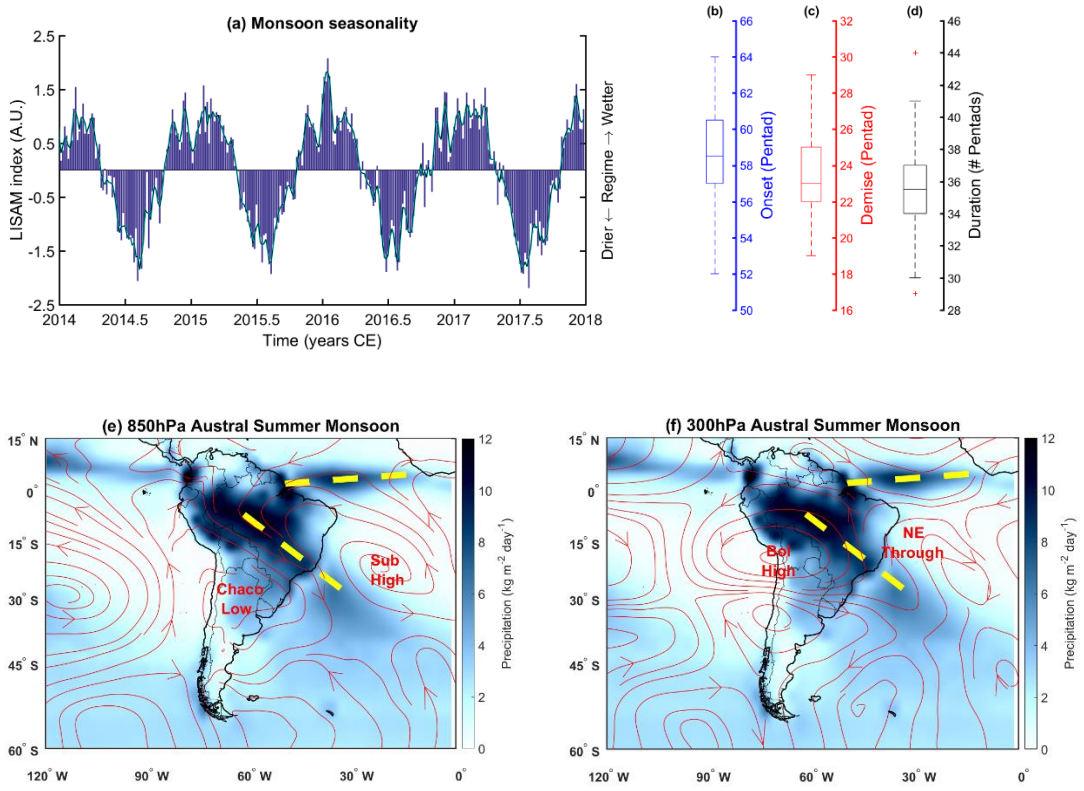

Figure 1.2 – South America Summer Monsoon Precipitation, wind and seasonality. *(a) Monsoon index showing the monsoon seasonality (details see Silva et al. 2007), (b), (c) and (d) onset, demise and duration of the rainy season, (e) low level and (f) upper level DJF summer circulation. In the figs. e and f, the zonal mean was taken from the 1981-2010 climatology. The yellow strips represent the ITCZ and SACZ from top to bottom respectively.*

During the onset phase of the monsoon, at upper levels, the double Jetstream (subtropical and polar) merges into one single Jetstream in midlatitudes, followed by the formation of an upper level high over the southeast of the Andean altiplano, accompanied by heavy rainfall over subtropical eastern Brazil. The upper level flux that was laminar, now, it becomes undulating, where there is the formation of an upper level

trough or upper troposphere cyclonic vortex over the Northeast of Brazil (Zhou and Lau, 1998; Gan et al. 2004).

The ITCZ located about 10°N, now displaces southward carrying more humidity toward the Amazon region, causing precipitation and low-level convergence due to the diabatic heating. Also, over the continent a thermal low forms in tropical middle latitudes over the Chaco region (Northern Argentina, Paraguay and Southern Bolivia), leading to a low-level circulation regime northwest-southeastward oriented, with wind velocities peaking about 850hPa called the Low-Level Jet (LLJ).

The LLJ is responsible to the moisture transport from the Amazon towards the South and Southeast region of the Brazil, like a conveyor belt (Zhou and Lau, 1998; Vuille et al. 2012) during the monsoon season, supporting the South Atlantic Convergence Zone, that traditionally is defined as an elongated northwest-southeastward nebulosity/precipitation band located from the eastern Amazon and Brazilian Midi-western to the Brazilian Southeastern region, characterizing the SAMS mature phase (December to February).

The SACZ also called here as monsoon axis, can be divided into three components, continental, coastal and oceanic (Carvalho et al. 2002; Carvalho et al. 2004). Either, the continental, the coastal or the oceanic components do not necessarily are coupled. The oceanic component is dependent of mid-latitudes wave trains propagating from the Pacific Ocean (Carvalho et al. 2004; Ferreira Sanchez and Silva Dias, 2004; van der Wiel et al. 2015) while over the continent the convective activity is more dependent of the Amazon continental heating that leads to the formation of the Chaco Low in lower levels and the Bolivian High in upper levels (Silva Dias et al., 1989) which together to the Subtropical High and the Northeast trough channels the moisture from lower latitudes toward higher latitudes, forming the SALLJ and the SACZ. Wave trains also interact in displacing the SALLJ creating a precipitation see-saw between the SACZ domain to the Southeastern South America ([SESA], South of Brazil and Rio de la Plata regions), observed during active warm and cold phase of the El-Niño Southern Oscillation (Carvalho et al., 2004; Ferreira Sanchez & Silva Dias, 2004).

Other important SACZ and monsoon driver is the South Atlantic Sea Surface Temperature ([SASST]Chavez & Nobre, 2004; Jorgetti et al., 2014; Bombardi et al., 2014). Following Bombardi et al. (2014) the subtropical SASST forms a north-south SST dipole coupled with the sea level pressure, where in its positive phase there is warm SST southward and cool SST northward, favouring mid-latitude transient propagation and leading to an enhanced SACZ. Similar results were found by Chavez and Nobre (2004) through numerical experiments.

The low-level humidity convergence due to the SACZ formation leads to an upper level convergence northeastward and southwestward of the SACZ, which maintains the upper level Bolivian High – Monsoon ridge – Northeast High system (BH-NT). Following Chen et al. (1999), the BH – NT system is formed by a short-wave train across the South America, modulated by a long-wave regime and maintained by the diabatic heating prevenient from the monsoon precipitation and by remote forcing from the Tropical Pacific region.

The demise of the SAMS is marked by the split of the jet stream and a weakening of the cross-equatorial flux, reducing the moisture influx into the continent and the humidity transport to higher latitudes, retreating the precipitation towards the equator, and therefore the onset of the winter regime.

1.2 – South America Summer Monsoon in the Last Millennium

1.1.1 – Last Millennium Climate – Overview

The last millennium is marked by three anomalous periods, one warm called Medieval Climate Anomaly (MCA), occurred between CE (Common Era) 850 to CE 1200 followed by a cold period called Little Ice Age (LIA), occurred between CE 1450 to CE 1850, followed by a warm period, the Industrial Period or the Current Warm Period (CWP), after CE 1850 (IPCC 2013).

Due to the lack of observations and historical documentations in the Southern Hemisphere, most researchers believed that the MCA and the LIA were just climate

anomalies of the Northern Hemisphere. However, in the last decades, Antarctic and Andean Ice cores studies, presented similar patterns as those observed in the Northern Hemisphere counterpart, showing the existence of the LIA signal on the Southern Hemisphere, which turned the LIA a global climate anomaly (Villalba et al. 1994).

The Medieval Climate Anomaly as a temperature phenomenon is just seem in some parts of the globe such as the Greenland and Europe (Broecker et al. 2001). However, tree rings sampled over the southwestern North America, in California State, and in the South America Andes, indicated long periods of drought preceded and followed by wet periods (Stine, 1994). So, Bradley et al. (2003) in his review study considered the MCA as a global hydrological anomaly, rather than a temperature one.

The transition between the MCA and LIA, called here of Transitional period (TRANS) are marked by greater volcanic eruptions, such as the Samalas (CE 1257) volcano in Indonesia which loads 64.5 Tg of SO_2 into the stratosphere (Toohey and Singl, 2017), followed and preceded by others minors eruptions (Scheleussner and Feulner, 2013) during this period (CE 1200-1450). Earth System models' simulations suggest that one of the causes for the LIA onset was the higher frequency and successive of intense volcanic eruptions, greenhouse gases and solar variability during the TRANS period (Schleusner and Feulner, 2013; Schurer et al. 2014; Stevenson et al. 2016; Slawinska and Robock, 2017).

Volcanic eruption contributes to the troposphere cooling through the injection of greater amount of sulphur rich gases such as SO_2 into the lower stratosphere, were the ejected aerosols are globally scattered through strong stratospheric zonal winds which circles the globe in few weeks. The volcanic aerosols scatter the incoming solar radiation increasing the planetary albedo (Robock and Mao, 1995), then cooling the troposphere. However, a greater sulphate aerosols concentration leads to a stratosphere warming due to emergent long-wave radiation absorption emitted from the surface and troposphere. The downward long-wave radiation emitted by stratospheric aerosols toward the surface, does not significantly contribute to minimize the cooling due to long-wave radiation loss, and the lower incoming short-wave radiation in the troposphere leads to negative net radiation budget, leading to a generalized cooling in the troposphere.

Transient climate simulations evaluated by Schleussner and Feulner (2013), show that successive volcanic eruptions during the late TRANS to early LIA period also lead to a rise in the ice sheets over the Arctic and Northern Atlantic Ocean, triggering a cascade of ice-ocean feedbacks, changing the subpolar gyre and at decadal time scale slowing the Atlantic Meridional Overturning Circulation (AMOC), cooling the North America and Europe due to the lesser heat transport from tropical latitudes transported by the gulf current and other components of the AMOC.

Some works such as by Usoskin et al. (2009), Steinhilbert et al. (2007) and Muscheller et al. (2007) retrieves last millennia time series of total solar irradiance from radionuclides in tree rings and ice cores. During the LIA, the solar activity was lower than in the MCA and today, due to the Maunder Minimum that was a period between CE 1600 – 1700 where the solar activity was very low (Eddy, 1976; Shindel et al. 2001). Global Atmospheric Models, only forced with the TSI of Maunder Minimum presents changes in the circulation of the North Atlantic Oscillation (Swingedow et al. 2010), in the Atlantic Multidecadal Variability (Ottera et al. 2010) and an indirect impact on the Southern Annular Mode phase through the higher stratospheric O_3 concentration (Abram et al. 2014), impacting the climate over the Southern Hemisphere.

Schurer et al. (2014) using a Global Circulation Model (GCM) forced with volcanic eruptions and solar forcing of the same magnitude of past millennia, mentioned that the main driver of Northern Hemisphere last millennium climate variability were the volcanic eruptions and greenhouse gases concentration rather than the solar variability which is one order of magnitude lower than the volcanic forcing.

The Current Warm Period (CWP) also known as Industrial Period, is considered the warmer period in last millennium (IPCC, 2013; Abram et al. 2016), attributed to the anthropic greenhouse gases emission such as CO_2, NO_X species and others (Abram et al. 2016). Following Abram et al. (2016), the onset of the CWP is not synchronous along the globe as well as the LIA and MCA onset and demise around the globe and along the South America (Novello et al. 2018, Apaéstegui et al. 2014).

1.1.2 – Last Millennium South America Climate

Over the South America due to the seasonality of the circulation and the low meridional temperature gradient, last millennia stable oxygen isotope paleoclimate records are better proxies of precipitation than temperature (Vuille et al., 2012; Thomson et al., 2013). The earlier South America paleoclimate works dated from the 1990's, among them, Villalba et al. (1994), using tree ring data sampled from the Chilean Patagonia to the North of Chile, show evidences of the MCA and LIA period through glacial advances imprinted in radiocarbons dating and drier and wetter periods in the tree rings.

In the 2000's, lake sediments (Bird et al., 2011), ice cores (Kanner et al., 2013; Thompson et al., 2013) and speleothems (Vuille et al., 2010) works appear, over the Tropical Andes, revealing that precipitation over the Tropical Andes follows the ITCZ north-south displacement and in centennial to millennial time scales reflects precipitation changes due to precessional forcings.

Stable isotopes speleothems studies in the core of the SAMS domain (Vuille et al., 2012; Novello et al., 2016; Bernal et al., 2016; Wortham et al., 2017; Novello et al., 2018), show that the last millennium precipitation variability on the Western South America (WSA) and Andes are in antiphase with the Northeastern Brazil (NEB) precipitation in some periods (Novello et al., 2016, Bernal et al., 2016). Both the WSA and the NEB presents a dry MCA. However, during the LIA the WSA presents wetter conditions and the NEB presents dryer conditions, revealing a precipitation see-saw between the two regions. Cruz et al. (2009), comparing NEB speleothem data to others WSA records in orbital time scales, shows this same precipitation antiphase see-saw between the two regions, indicating that the South America precipitation variability can be not only attributed to changes in hemispheric insolation but also by remote forcings through teleconnections (Ambrizzi & Hoskins, 1995).

Novello et al. (2018) and Bernal et al. (2016) studying speleothems in the core of the SAMS and in the SESA regions, through a latitudinal cross-section of the normalized isotopic records' data showed that during the LIA the southern speleothems present

wetter conditions than the northern ones, leading them to conclude that during the LIA the SACZ was southward displaced than in the MCA and CWP periods.

South America records composites evaluated for the positive and negative phase of the Atlantic Multidecadal Oscillation (Mann et al. 2001; Wang et al. 2017) shows that during the MCA, the AMO probably influenced the precipitation regime over the foothills of the Andes; over Peru (Apaéstegui et al., 2014). Novello et al. (2014) also found periodicities about 64 years, attributed to the AMO variability (Chiessi et al., 2009) over the NEB and over the La Plata Basin (Perez et al. 2016). Almost all the previous works compare its proxy data to the AMO reconstruction of Mann et al (2005). Nowadays, there is new AMO reconstruction by Wang et al. (2017), presenting different results than the former reconstructions, so the AMO footprint over South America is not a closed issue.

Other possible driver of the last millennium South America climate variability is the South Atlantic Sea Surface Temperature (SASST) variability. In a paleoclimate context Utida et al. (2019) retrieves the northern of NEB variability through lake levels, showing the dependence of NEB precipitation to ITCZ displacement and suggesting the role of the tropical South Atlantic SST on the NEB precipitation variability.

Further details of South Atlantic Climate variability and possible drivers are given in the chapters 3 to 5.

1.3 – $\delta^{18}O$ stable Isotope

Most of the data used in this work are paleo-precipitation proxies derived from oxygen isotopes ^{18}O. So, in this section a detailed description of the ^{18}O is given and an overview of the other data. The other paleoclimatic data are described in the coming sections.

The stable isotopes of interest are the ^{18}O and ^{16}O. Their variation is measured by a mass spectrometer relative to a standard that for carbonates is the Pee Dee Belemnite (PDB) and that for waters is Vienna Standard Mean Ocean Waters (SMOW) (Gonfiantini,

1978; Lachniet et al., 2006; and Fairchild et al., 2012). The δ notation (Sharp, 2007) is expressed as:

$$\delta^{18}O = \left(\frac{{}^{18}O/{}^{16}O_{sample} - {}^{18}O/{}^{16}O_{standard}}{{}^{18}O/{}^{16}O_{standard}} \right) \qquad (eq.1.1)$$

The isotopic ratio is expressed as per thousand or per mile (‰). When a sample have $\delta^{18}O$ higher than another, the sample is called "enriched" in ^{18}O or "heavier" and otherwise "depleted" or "lighter" in ^{18}O.

There are many processes that cause ^{18}O isotopes contained in an air parcel, in the fig.1.3 some processes related to the ^{18}O isotopic depletion and enrichment are depicted. The hydrological process that enriches ^{18}O into the atmosphere (air parcel) is the evaporation from the ocean water ending with the ^{18}O depletion through the precipitation. The process that favours one isotope over the other during the water phase change is called fractionation (Lachniet et al., 2006, Fairchild et al. 2012).

Fractionation may be either in equilibrium or kinetic, the former can obscure the climatic signal (Lachniet et al., 2006). The first δ^{18}O control is the isotopic ^{18}O relative quantity on the ocean where the evaporation takes place, being dependent of ocean salinity and temperature as well as whether the evaporation source is near of an estuary or not, and the evaporation-precipitation budget (salinity). The fig.1.4 shows the δ^{18}O values over the oceans.

During ocean evaporation, equilibrium fractionation results in ^{18}O are incorporated into the water vapour than originally presented at the ocean, leading to δ^{18}O values in the air parcel lower than over the ocean (Lachniet et al., 2006; LeGrande & Schmidt, 2006; Fairchild et al., 2012), being dependent on the ocean temperature. The relative humidity also affects the δ^{18}O value at the air parcel, this humidity

dependent process is called of kinetic fraction (Lachniet et al., 2006; Fairchild et al., 2012).

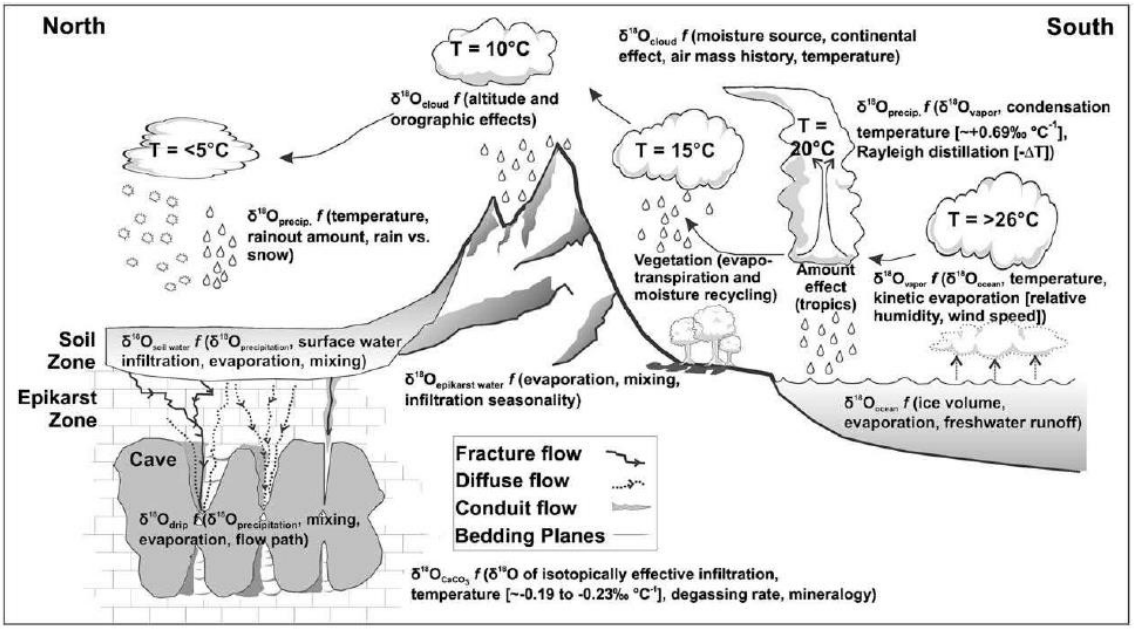

***Figure 1.3 – $\delta^{18}O$ controls**. Diagram illustrating the primary processes related to $\delta^{18}O$ variations relevant to speleothems paleoclimatology. The dominant controls are related to temperature, precipitation and relative humidity. Adapted from Lachniet et al. (2006).*

As the air parcels evaporates, it condenses, forming clouds and precipitates. In contrast to the evaporation, precipitation is just an equilibrium process. ^{18}O due to its greater atomic mass (in relation to ^{16}O), it is preferentially incorporated on the condensation, so the $\delta^{18}O$ rain are higher than in the remaining air parcel's water vapour, lowering the ^{18}O quantity in the atmosphere. Thus, to condense more moisture the cloud temperature must decrease, and this can take place due to fronts, orographic lifting or convection, which becomes the temperature drop and the cloud moisture quantity the main controls of the $\delta^{18}O$ values inside the air parcel, this process of progressive condensation and $\delta^{18}O$ lowering is called of Rayleigh distillation (Lachniet et al., 2006; Fairchild et al., 2012). In the fig.1.5 the precipitation $\delta^{18}O$ values inside the continent is showed.

As one can observe in the fig.1.5 the $\delta^{18}O$ value across the continents is lower to higher latitudes, this shows the $\delta^{18}O$ dependence to the temperature and to the air

parcel history. Over higher latitudes regions such as Europe, $\delta^{18}O$ is a better proxy of temperature variability than precipitation amount (Deininger et al. 2017) and do not present a seasonality in the circulation, where the air parcels can come from various sources. However, over the tropical South America, the circulation presents a monsoonal climate, with clear precipitation peaks during the summer season, where most of air parcels come from the Tropical Atlantic Ocean. As across the continent there is not a high temperature gradient. The $\delta^{18}O$ is a better precipitation proxy than temperature over the Tropical South America or SASM region (Vuille et al. 2012).

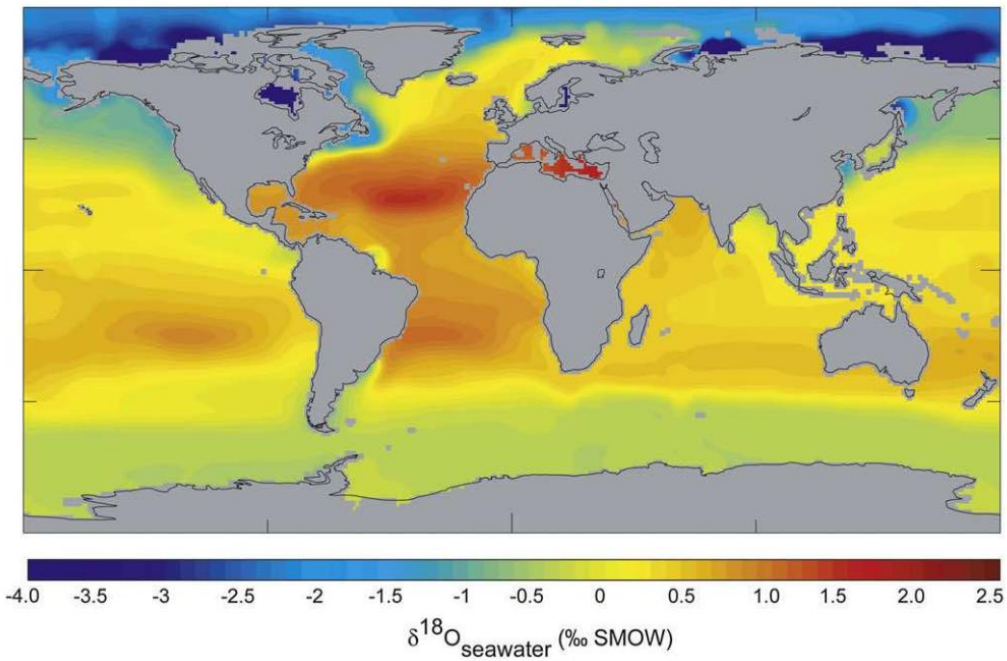

Figure 1.4 – $\delta^{18}O$ of the Ocean. *Gridded $\delta^{18}O$ data of the ocean from LeGrande and Schmidt (2006). Adapted from Lachniet et al (2006).*

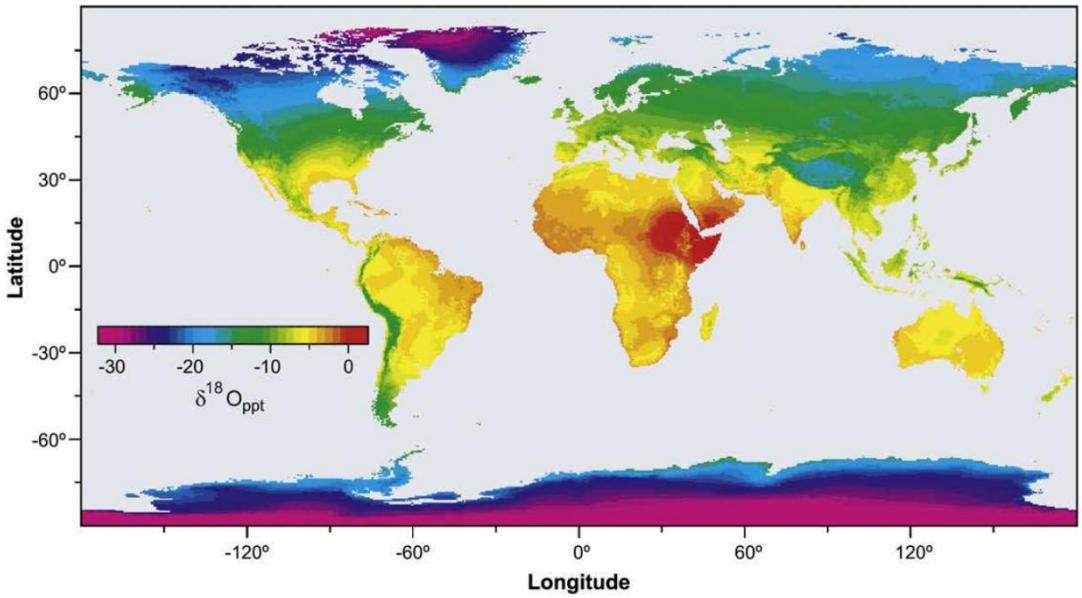

Figure 1.5 – $\delta^{18}O$ of precipitation. *Mean annual $\delta^{18}O$ interpolated from GNIP stations. Adapted from Lachniet et al. (2006).*

Other relevant hydrologic process inside the continent is the biota evapotranspiration that does not fractionate the $\delta^{18}O$. As the moisture precipitates over the continent, it evaporates back into the atmosphere, without changing the $\delta^{18}O$ values. So, over tropical areas the $\delta^{18}O$ spatial variability can be attributed just to the precipitation which is depleted as the parcel goes further inside the continent and precipitates and evaporates. This process is called continental effect and the depletion due to precipitation amount is called amount effect.

Before the rainwater percolates into the cave system, it is submitted to canopy interception, evaporation and runoff, which can enrich ^{18}O in the soil water. Vegetation characteristic also affects the $\delta^{18}O$ values, related to the soil water evaporation as well as anthropic influences such as urbanisation (Lachniet et al., 2006).

The cave drip water $\delta^{18}O$ value is dependent on the seasonality and the residence time in the soil and Epikarst Zone (a thick portion of bedrock that extends from the base of the soil zone, characterized by fractures which allows the water percolates toward the cave) as well as, the cave saturation. Generally, after the percolation process, the cave drip water is ^{18}O enriched than the precipitation and most of the paleoclimatic

studies are realized in saturated caves to avoid kinetic fractionation due to evaporation (Lachniet et al., 2006; Fairchild et al., 2012).

1.4 – Objectives

Most of the last millennium paleoclimate works, presents the climate in very limited geographic region, just assessing the climate variability at the place where the record was collected (Kanner et al., 2013; Thompson et al., 2013; Novello et al., 2016; Wortham et al., 2017). These works show that the paleo-precipitation variability across the South America was not uniform, with the western portion of the continent variating in opposite manner to its eastern counterpart during the LIA period and variating similarly during the MCA period (Novello et al., 2012; Novello et al., 2018).

So, recently the number and the quality of paleoclimatic records across the South America rose substantially, enabling the analysis of the last millennium paleo-precipitation not just in terms of temporal variability, but also in terms of spatio-temporal variability.

One approach to study the temporal and spatial variability together is the use of eigen techniques. Here the first objective is to retrieve spatiotemporal patterns with physical meaning through the compilation of 12 available last millennium paleo-precipitation records by means of the Monte-Carlo Principal Component Analysis.

The Monte-Carlo Principal Component Analysis allows us to decompose the last millennium SAMS into its components such as the SACZ, SESA precipitation and the NEB precipitation. The second and main objective of this thesis is to retrieve the spatiotemporal variability of these SAMS components in the last millennium context.

Previous works (Apaéstegui et al., 2014; Novello et al., 2016; Bernal et al., 2016) attributes the precipitation at some sites in the South America to the influence of some climate variability patterns such as the Atlantic Multidecadal Oscillatio (AMO), Southern Annular Mode (SAM) and El Niño Southern Oscillation (ENSO). So, the third objective of this thesis is to assess the main drivers of the last millennium South American climate

through the comparison between the Principal Component modes to the last millennium climate variability time series and assess changes in theirs South America footprints along the last millennium.

The thesis is organized as the following, in the chapter 2 the methodology and an overview of the proxy time series is showed, chapter 3 shows the multi-proxy compilation using the Monte-Carlo method as well as for the PCA. In the chapter 4 the interpretation of the patterns obtained through the compilation and the coherence of the climate proxies along the South America is presented, as well as, comparisons to other South America last millennium time series, and proxies other than precipitation. In the chapter 5 the proxies' compilation is compared to the climate index time series and chapter 6 presents some discussion and conclusions.

Chapter II

Methods and Data Sets

2.1 – Principal Component Analysis

Introduced by Pearson (1901) to find the line or plane which best fits a given set of multidimensional data, and mathematically formalized by Hotelling (1933), Principal Component Analysis becomes a standard exploratory data analysis technique in multivariate statistics to reduce sets of data into fewer components.

In earth sciences, particularly in meteorology and climatology, generally, a given spatial field exhibit large correlation between the variables or locations, forming a spatial pattern of common spatiotemporal variability which has a "physical" meaning (Lorenz et al 1956). So, the Principal Component Analysis (PCA) has a potential to reduce a numerous set of M variables data into a fewer set of N << M variables, with each N data representing a given piece of the data variability associated with a spatial field. The Loadings Coefficients, often called by Empirical Orthogonal Function (EOF) and the Principal Component or amplitude of the Loading Coefficients, the standing oscillation of the spatial pattern, sometimes reveals non-trivial or hidden characteristics of the data.

Let **X** be a given field or set of variables disposed in a m x n matrix, with the rows of the matrix representing the time evolution of the variables and each column representing a different variable or grid point position, and let us take the anomaly of **X**, **x,** and compute the sample covariance matrix S

$$\boldsymbol{x} = \boldsymbol{X} - \overline{\boldsymbol{X}} \qquad (eq.2.1)$$

$$\mathbf{S} = \frac{1}{n-1}(\boldsymbol{x} \cdot \boldsymbol{x}') \qquad (eq.2.2)$$

Where n is the number of observations and the (') subscript represent the transpose matrix of x.

The goal of the PCA is to reduce the data into a set of meaningful patterns which maximize the data representation or the variance of the data, so let **u** the basis vector in which the principal component **z** can be written as a linear combination,

$$\boldsymbol{z} = \boldsymbol{u}' \cdot \boldsymbol{x} = \sum_{\boldsymbol{i=1}}^{\boldsymbol{n}} \boldsymbol{u_i}' \cdot \boldsymbol{x} \qquad (eq.2.3)$$

in other words, our goal is to find the argument which maximizes the variance of z, given by,

$$\begin{aligned} VAR(\boldsymbol{u}' \cdot \boldsymbol{x}) &= E\left(\boldsymbol{u}'^2 \cdot \boldsymbol{x}^2\right) - \left(E(\boldsymbol{u}' \cdot \boldsymbol{x})\right)^2 \\ &= VAR(\boldsymbol{u}')VAR(\boldsymbol{x}) + VAR(\boldsymbol{u}')\left(E(\boldsymbol{x})\right)^2 + VAR(x)\left(E(\boldsymbol{u}')\right)^2 \\ &= u'\boldsymbol{S}u \qquad (eq.2.4) \end{aligned}$$

Assuming the normalization $u_i' \cdot u_i = 1$ is a unit length vector, we want:

$$Arg\max[u'\boldsymbol{S}u - \lambda\,(u'u - 1)] = \frac{d}{du}[u'\boldsymbol{S}u - (\lambda\,u'u - 1)] = 0$$

$$= \boldsymbol{S}u - \lambda u = 0 \qquad (eq.2.5)$$

where λ is the $VAR(\boldsymbol{u}_i' \cdot \boldsymbol{x})$ or the explained variance of each basis vector **u**. Thus the eq.2.5 is a classical linear algebra problem to find eigenvectors **u** and eigenvalues or latent values λ. In our context, the loading coefficients (spatial pattern) and the contribution of each component (explained variance) given by:

$$e_i = \frac{\lambda_i}{\sum_{j=1}^{n} \lambda_j} \qquad (eq.2.6)$$

and the Principal Component, called also of scores or amplitude, given by the eq.2.3, the variable z.

As the first components represent the higher data variability, degenerating to the higher components or modes, following North et al. (1982), ideally the eigenvalues spectrum must present an exponential decay, however in some case this does not occurs, when the eigenvalues are nearer each other, so North et al. (1982) derived a formula to estimate the error or variability of the eigenvalues, given by:

$$error_\lambda = \lambda_i \sqrt{\frac{2}{n}} \qquad (eq.2.7)$$

This formula permits us to build error bars, if the error bars of one eigenvalue overlaps the other, we can tell that these patterns are “contaminated” or subjecting to intersample variability. To overcome this constraint generally, variamax rotation or other kind of orthogonal rotation is performed over the loading coefficients. Here we will use a modified version of eq.2.7 to quantify the error in estimating the eigenvalues, presented in the next chapter, in our case the loadings rotation was not needed.

The variables used in the present work, due to their characteristics, have different amplitudes (scales), what can skew the loading coefficients or spatial pattern

towards the greater amplitude variables, so to avoid this problem, the correlation matrix (covariance of the normalized data or z-scores) instead of the covariance matrix is used to perform the PCA.

Further details about mathematical formulation can be found in Preisendorfer (1988), and Wilks (2011). In the section 3.2, PCA is performed over the proxy dataset and further methodological details is given.

2.2 – Spectral Analysis

2.2.1 – Multi-Taper Method Power Density Estimate

To study a time series in the frequency domain, a common technique is the use of periodogram based on Fourier series. The periodogram permits us to assess and isolate dominant frequencies through the computation of the variance of a given cycle and infer about causal relationship between known cycles to dominant cycles found in the time series' periodogram, commonly applied in paleoclimatology and climatology (Torrence and Webster, 1995; Torrence and Compo, 1998).

Some periodograms or Power Density Estimate (PSD) perform better than other for some specific problems. The PSD based only on Fourier Analysis, is the magnitude of its response that resembles a rectangular window, where, as the length of signal increases, the bandwidth of each bandpass decreases, making it fair selective estimate. However, the computation of the power at each bandpass filter depend on a single sample of the filtered signal, which produces an imprecise approximation and the rectangular window leading to a poor bandpass filter.

Thomson (1982) improves the PSD by the aggregation of a set of optimal bandpass filters to compute the PSD derived from a set of sequences, the Slepian Sequences, where these sequences seeks the maximal energy concentration at a given band or window, called of tappers, which are orthogonal to each other. So, the Multitaper PSD is an average of periodograms based on this family of orthogonal windows, which have a most accurate PSD than the conventional Fourier periodogram

(see Thomson 1982 for details about the derivation and Prieto et al. 2009 for computational implementation and some examples in earth sciences).

The data sequence is multiplied by several tappers (weights), the Slepian Sequence, each tapper is selected in a way that minimizes the tendency of strong peaks to spread into neighbouring frequencies, so each tapered copies of the data is Fourier transformed and weighted averaged. Chosen a bandwidth W over which the spectrum is smoothed, for a N long sequence, fixing the time-bandwidth product NW and the number of tappers k. For the kth Slepian tapper v_k, we have:

$$Y_k(f) = \sum_{n=0}^{N-1} y(n) v_k(n) e^{-2\pi i f n} \qquad (eq. 2.8)$$

The kth eigen component, which is the Fourier transform of the N-long data sequence y(n) after multiplied by v_k or in other words the tapered sequence. The PSD estimate of a single frequency can be computed as,

$$S_f = |Y_k(f)|^2 \qquad (eq. 2.9)$$

Thomson (1982) and Prieto et al. (2009) suggest the computation of the weights d_k, as:

$$d_k(f) = \frac{S(f)\sqrt{\lambda_k}}{S(f)\sqrt{\lambda_k} - (1-\lambda_k)\sigma^2} \qquad (eq. 2.10)$$

where λ_k is the kth eigenvalue and σ^2 is the square of standard deviation or the variance. The estimated PSD can be computed through the weighted average:

$$\hat{S}(f) = \frac{\sum_{k=0}^{k-1} {d_k}^2 S_f}{\sum_{k=0}^{k-1} {d_k}^2} \qquad (eq. 2.11)$$

A limitation of the Multitatper method is that the time interval or sampling rate must be constant, what rarely occurs in climate proxy time series, however most of the climate proxy time series used in this work is resampled into a uniform time interval, using a cubic spline. An alternative PSD method that is not constrained by a uniform sampling rate can be found in Schulz and Mudelse (2001) the REDFIT algorithm.

2.2.2 – Wavelets and Wavelet Coherence Analysis

The PSD estimate described previously, just give us the power spectrum, telling nothing about its variability through the time series extent, a widely used technique to access together space (time) and frequency, called Wavelet (Daubechies 1990), which decompose the time series into scales, through the convolution between a basis function to the Fourier time series.

The idea behind the WTC is to study frequency features of the signal locally and not globally as the done by the periodogram. The convolution between the time series and the kernel function permits us to study features of the signal matched to their scale, in other words, finer features on small scales and broader features on large scales (Foufoula-Georgiou, 1995).

In geophysics, the most common kernel or base function used is the Morlet wavelet. The Morlet Wavelet provides a good balance between time and frequency localization (Grinsted et al. 2004, Torrence and Compo, 1998). The Morlet wavelet is given by:

$$\psi_0(\eta) = \pi^{-1/4} e^{i\omega_0 \eta} e^{-1/2\eta^2} \qquad (eq. 2.12)$$

where ω_0 is the dimensionless frequency and $\eta = st$ is the dimensionless time, or the scale s multiplied by the time.

The Continuous Wavelet Transform (CWT) of a time series $(x_n,\ n \in \mathbb{N} / 1 < n < N)$ with a uniform sampling rate δt, is defined as the convolution between $x_n$with ψ_0 the wavelet,

$$W_n^x(s) = \sqrt{\frac{\delta t}{s}} \sum_{n'=1}^{N} x_{n'} \psi_0 \left([n' - n] \frac{\delta t}{s} \right) \qquad (eq. 2.13)$$

and the Wavelet power is given by,

$$CWT = |W_n^x(s)|^2 \qquad (eq. 2.14)$$

However, it is desirable to compare two time series in the space-time, so let $(y_n,\ n \in \mathbb{N} / 1 < n < N)$ be another time series with the same length as x, we can define the cross spectrum or cross-wavelet that reveals periods of high common power, as,

$$XWT = \left|W_n^{xy}(s)\right|^2 = \left|W_n^x(s) \cdot W_n^y(s)\right|^2 \qquad (eq. 2.15)$$

and the complex argument *Im(XWT)* can be interpreted as the relative phase between x and y.

A correlation measure between $W_n^x(s)$ and $W_n^y(s)$ is desirable, so following Torrence and Webster (1999), we can define the wavelet coherence between both time series as,

$$R_n^2 = \frac{\left|s^{-1}W_n^{xy}(s)\right|^2}{\langle s^{-1}|W_n^x(s)|^2\rangle \cdot \langle s^{-1}\left|W_n^y(s)\right|^2\rangle} \qquad (eq.2.16)$$

A nonlinear and non-parametric measure, with the same objective of wavelet is also used in this work, the Empirical Mode Decomposition, presented in the next section.

2.3 – Empirical Mode Decomposition

Wavelet and Coherency analysis is suitable to analyse stationary signals and linear signals (Torrence and Compo, 1995; Grinsted et al. 2004), however paleoclimate time series do not necessarily must match this stationarity and linear condition, a non-linear and non-parametric technique to overcome these constraints is the Empirical Mode Decomposition ([EMD], Huang et al. 1998).

As the Wavelet analysis, the EMD consists on decompose a time series into scales, but these scales are not constrained to a periodicity or temporal parameter. In practical terms the decomposition consists in found the upper and lower envelope of a time series and subtract the time series from the average between the upper and lower envelope, the resulting new time series, called of Intrinsic Mode Function (IMF). This process is done iteratively up to some conditions are satisfied, so the last IMF is called of the trend mode.

The EMD decomposition can be resumed through the following algorithm (Manjula & Sarma, 2012),

(i) The upper and lower envelopes are constructed by connecting all the maxima and all the minima with cubic splines, respectively;

(ii) Take the mean of the two envelopes and let it define as m(t), then subtract the mean m(t) from the original signal to get the h(t),

$$h(t) = x(t) - m(t) \qquad (eq.2.17)$$

(iii) If the eq.2.17 satisfies the following conditions:

a. For a given time series h(t), the number of extreme and the number of zero crossings is either equal or differ almost by one;

b. At any point, the mean value of the envelope defined by the local maxima and minima is zero

Then h(t) can be considered an IMF;

(iv) The h(t) or IMF are separated from the original signal, giving rise a residual time series,

$$r(t) = x(t) - h(t) \qquad (eq.2.18)$$

Now taking the residual time series, the steps (i) to (iv) are repeated up to the conditions showed in (iii) are no more satisfied, this process is called of “sifting process’. So, one can construct a non-linear filter through the sum of the IMFs, a procedure used in the chapter V to compare the time series.

2.4 – Regime Shift Test

Most of the last millennium paleoclimate works explore two anomalous periods, a cold called of LIA and a warm called of MCA, and over the South America, the changing property between the two periods is the precipitation (Vuille et al. 2012; Bird et al. 2011). Both the cold and warm (or wet and dry) period, stands out visually in the time series, however a quantitative or statistical measure of the beginning and ending of these anomalous periods is desirable, thus a regime shift test or change point detection is used in this work.

The regime shift test chosen in this work can be found in Lavielle (2005) and Killick et al. (2012). It consists of dividing the signal into a given number of sections and to find abrupt changes in a given statistical property that can be the mean, variance, trend, or even its probability density function.

We are interested in the mean case, so, we can define a change point as a sample or time instant in which the mean of the signal changes abruptly, thus, for two change points,

(i) Choose a point that divides the signal in two sections

(ii) Compute an empirical estimate of the desired statistical property, the mean for each section

(iii) At each point within a section measures how much the mean deviates from the empirical estimate and adds the deviations to all points.

(iv) Adds the deviations to the total residual error

(v) Varies the location of the division point until the total error becomes minimum.

In mathematical terms, let $\{x_i, i \in \mathbb{N} \,/\, 1 < i < n\}$ the time series or the signal and J the contrast function, for K changing points, we want to find the argument that minimize (or the maximum likelihood estimate of):

$$J(K) = \sum_{r=0}^{K-1} \sum_{i=k_r}^{k_{r-1}-1} \left(x_i - \frac{1}{n - k_r - 1} \sum_{m=i}^{k_{r-1}-1} x_m \right)^2 + \beta K \qquad (eq. 2.19)$$

were k_0 and k_r are the first and last sample of the signal and β is a penalization function, for details and generalization to other statistics see Lavielle (2005). Another alternative often used in climatology and meteorology is the Rodionov test (Rodionov, 2004).

2.5 – Climate Proxies and Reanalysis Datasets Overview

2.5.1 – Proxy Data

Due to the greater quantity of proxy data used in this work, a detailed description of each time series will be given in the next chapters. Here just a very brief description of the dataset used is provided.

Table. 2.1 presents the South America Paleoclimate proxies across the continent used in this work. Only records spanning at least the period between AD 500 to AD 1970 or nearer this date were used in this work, however, due to uncertainty constraints and the Monte-Carlo simulation discussed in the next chapter, the analysis period is constrained to AD 600 to AD 1970. Two of our time series do not span up to AD 1970, so in the compilation the alternate least square algorithm is used. The figure 3.1 displayed in chapter III shows the geographical distribution of the records.

Most of our records are oxygen isotope $\delta^{18}O$ derived from speleothems, ice cores and lake sediments, just one record is based on the Sr/Ca ratio which is a better precipitation proxy than the $\delta^{18}O$, due to the source effect, concerning to different humidity sources, also discussed in detail in the next chapter.

Last millennium climate reconstructions of the South America ITCZ activity, Atlantic Multidecadal Oscillation, Southern Annular Mode, La Plata Basin precipitation and others are presented in the table.2.2. and are described in detail in the chapters IV and V.

Table 2.1 – South America proxy climate reconstruction.

Site Name	Records	ID	Time Span	Isotope	Lat	Lon	Mean Sampling	References
Palestina Cave	PAL03+PAL04	**1**	CE 413- CE 1928	$\delta^{18}O_{cal}$	5.92°S	282.65°E	5.0 years	Apaestegui et al.2014
Huagapo Ice cap	HUA	**2**	CE -5196- CE 2000	$\delta^{18}O_{ice}$	11.27°S	*284.21°E*	5.0 years	Kanner et al.2013
Quelcaya Ice cap	QUELC	**3**	CE 226 - CE 2009	$\delta^{18}O_{ice}$	13.93°S	*289.17°E*	1.0 year	Thompson et al. 2013
Pau d'Alho cave & Curupira cave	ALH+CUR4	**4**	CE 481 – CE 1961	$\delta^{18}O_{cal}$	15.20°S	303.20°E	0.6 years	Novello et al.2016
Jaraguá Cave	JAR1+JAR4	**5**	CE 442 – CE 2009	$\delta^{18}O_{cal}$	21.08°S	304.42°E	2.5 years	Novello et al. 2018
Botuverá Cave	BOT	**6**	CE -7107 – CE 2009	Sr/Ca	27.22°S	310.85°E	0.2 years	Bernal et al. 2016
Cristal Cave	CRT1	**7**	CE 2127 – CE 2003	$\delta^{18}O_{cal}$	24.58°S	311.42°E	2.7 years	Vuille et al. 2012
Tamboril Cave	TMO	**8**	CE 272 – CE 1982	$\delta^{18}O_{cal}$	16.00°S	313.00°E	3.6 years	Wortham et al. 2017
São Bernardo Cave & São Matheus	SBE3+SMT5	**9**	CE -798 – CE 2010	$\delta^{18}O_{cal}$	13.81°S	*313.65°E*	1.2 years	Novello et al. 2018
Iraquara Cave	DV2+TR5+LD12	**10**	CE -815 – CE 2010	$\delta^{18}O_{cal}$	12.36°S	318.43°E	4.0 years	Novello et al.2012
Paraiso Cave	PAR01+PAR03	**11**		$\delta^{18}O_{cal}$	4.00°S	*304.73°E*	7 years	Wang et al. 2017
Pumacocha Lake	PUM	**12**	CE -277 – CE 2007	$\delta^{18}O_{cal}$	10.07°S	*283.94°E*	1 year	Bird et al. 2011

Table 2.2 – Last Millennium climate proxy reconstruction.

Name	Reconstruction	Type	Time span	Reference
GeoB13813-4	La Plata Basin Precipitation	Fresh Water Diatomaceous account	CE 750 – CE 2000	Perez et al. (2016)
Cariaco Basin	ITCZ	Concentration of Titanium (%Ti)	CE -12000 – CE 1950	Haug et al. (2001)
SAM	Southern Annuar Mode	Multiproxy Compilations	CE 1000 – CE 2000	Abram et al. (2014)
AMO	Atlantic Multidecadal Oscillation	Multiproxy Compilation	CE 800 – CE 2000	Wang et al. (2017)
NHtemp	Northern Hemisphere Temperature	Multiproxy Compilation	CE 0 – CE 2000	Moberg et al. (2005)
El Niño	Southern California Precipitation PCA	Tree Rings dataset Compilation	CE 800 – CE 2000	Li et al. (2011)

2.5.2 – Coupled 20th Century Reanalysis (CERA20C)

The reanalysis project combines satellite, surface observations and general circulation models to retrieve atmospheric conditions. Reanalysis like the ECMWF ERA-Interim (European Centre for Medium Range Forecast, European Reanalysis; Dee et al., 2011), assimilates surface data such as Sea Surface Temperature (SST), surface pressure, surface temperature, as well as upper air data derived from radiosondes and satellites which goes into an Atmospheric General Circulation Model (AGCM) allowing the retrieval of the past atmospheric conditions, however these reanalysis span just about 40 years in the past, limiting the time scale of the analysis.

Recent efforts by these research centres like the ECMWF (European Centre of Medium-Range Weather Forecast) to integrate the GCMs to other earth system components such as cryosphere, lithosphere, vegetation and oceans, results in the Coupled Reanalysis. The Coupled 20th Century European Reanalysis (CERA20C; Lalloyaux et al., 2018) produced by the ECMWF, assimilates just surface data, like SST, sea level pressure, surface pressure, sea ice into an Earth System Model, forced with prescribed radiative forcing, spanning 110 years (CE 1901 -2010), allowing climate variability studies in decadal time scales.

Ten ensembles of the CERA20C reanalysis is available from hourly to monthly time resolution in 40 pressure levels. To avoid internal model variability, the ensemble mean is evaluated before the analysis. Due to the availability, the variable Total Column Rain Water (TCRW) was used instead the Total Precipitation (TP), which is available just for the forecast product.

Chapter III

Monte-Carlo Principal Component Analysis and South America Isotopic Time Series

Along the tropical South America, the number of last millennia paleoclimatic time series rose substantially allowing studies of the precipitation variability on different sites. However, most of the previous SAMS studies approaches the precipitation variability over a very localized region, only assessing the precipitation variability on the records' site.

To overcome these constraints, in works such as Novello et al. (2018) and Apastaegui et al. (2018), compares their isotopic time series to other records across the South America using composites analysis of well-known last millennia climate periods such as the Little Ice Age and the Medieval Climate Anomaly. However, this approach does not reduce the data complexity.

Other approach is the use of Principal Component Analysis (PCA), which reduces the data into a set of few variables based on the covariance/correlation matrix, where the first variables or Principal Components represent larger portions of the data variability, degenerating to the others, generally taken as noise or no significant components, which reduces the data complexity and manifold. Some previous studies like Deininger et al. (2016), Lechleitner et al. (2018), Tierney et al. (2013) used this

approach to study the temperature evolution over Europe, the Northern and Southern Hemisphere ITCZ variability and the Eastern African hydroclimate variability in the last millennium, respectively.

So, in this work this approach will be used to retrieve the last millennia paleo-precipitation variability through $\delta^{18}O$ and Sr/Ca records along the Tropical South America monsoon region. In the first part of this chapter a description of the isotopic datasets is presented. In the second part a Monte-Carlo or bootstrapping method to account the speleothems and other proxies dating uncertainty is presented and in the last part, some details of the data compilation technique or Principal Component Analysis, as well as principal components selections rules is given.

3.1 - $\delta^{18}O$ Isotopic Datasets and Trace Elements

The 12 proxy time series location are represented in fig.3.1 and table 3.1, together with the summer (Dec-Feb) precipitation climatology, extracted from 30 years (CE 1980 - 2010) of GPCP data. With the yellow dotted strips representing the main SAMS weather components, the SACZ and the ITCZ.. As one can see, all the present records are located inside the monsoon region, taking as the area where the summer (DJF) minus winter precipitation (JJA) is greater than 2 mm/day ($kg/m^2/day$). At least 70% of the precipitation amount falls during the summer on this domain (Wang and Ding, 2006), as indicated by the grey heavy line in the figure.

Most of our $\delta^{18}O$ records were derived from speleothems samples and some records like #3 Quelcaya (Thompson et al. 2013) and #2 Huagapo (Kanner et al. 2013) were based on ice cores extracted from ice caps over the Andes. The record #6 Botuvera (Bernal et al. 2016) were based on the Sr/Ca relationship.

Due to the Rayleigh distillation (see chapter 1) the $\delta^{18}O$ isotopes getting into the continent are depleted through the precipitation and enriched through evaporation and biota evapotranspiration. However, during the summer over tropical South America, the precipitation is greater than the evaporation/evapotranspiration and during the winter

season, the precipitation and evaporation/evapotranspiration rates are nearly equivalent, becoming $\delta^{18}O$ isotopes derived from speleothems and lakes suitable proxies for summer precipitation or monsoon precipitation due to the amount effect (Lachniet et al. 2006).

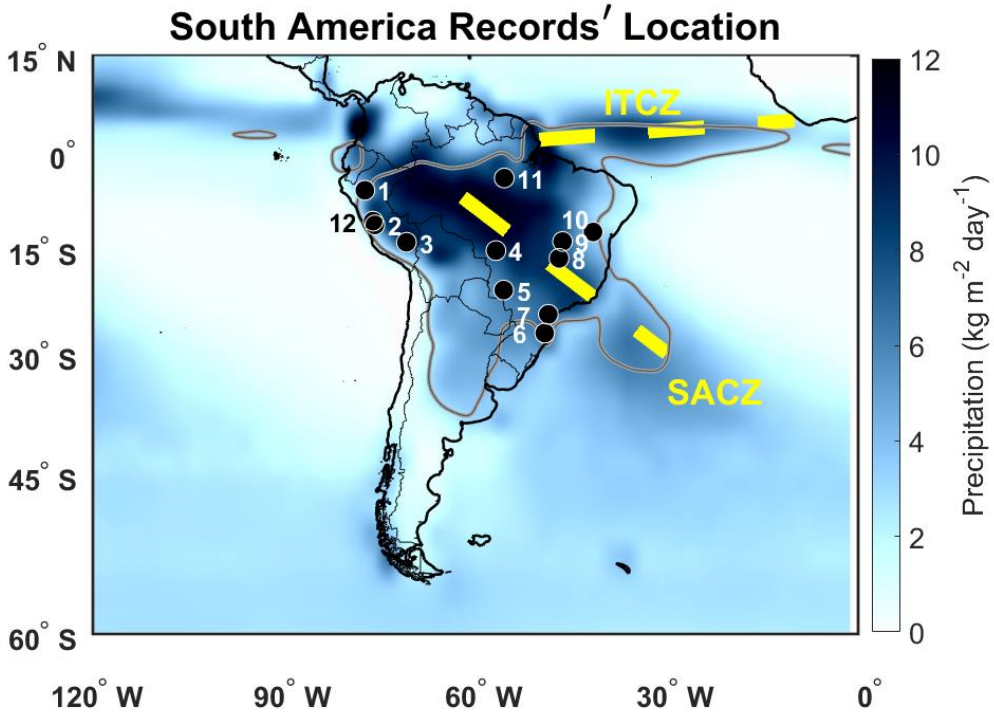

Figure 3.1 - South America Isotopic Records Location*. The shaded around represent the summer (DJF) precipitation climatology, extracted from 30 years of GPCP data. The yellow strips denote the SACZ and ITCZ position as indicated by the inscriptions and the grey coloured contour denotes the monsoon domain.*

The $\delta^{18}O$ value is affected also by the "source effect" (LeGrande and Schmidt, 2006; Lachniet, 2006), which arises due to differences in the air mass or moisture origin.. Due to the monsoon climate is present over almost all the 12 records sites, we can assume that the continental summer moisture comes from a common source, the tropical Atlantic Ocean. Following the table 3.1 works show that the amount effect is dominant over almost all the records, except over the #6 BOT speleothem's site.

***Table 3.1 - Speleothems $\delta^{18}O$ Isotopic time series**. The spatial distribution of the records is presented in the fig.3.1.*

Records	ID	Isotope	Lat	Lon	Mean Sampling	Reference
PAL03+PAL04	**1**	$\delta^{18}O_{cal}$	5.92°S	77.35°W	5.0 years	Apaestegui et al.2014
HUA	**2**	$\delta^{18}O_{ice}$	11.27°S	*284.21°E*	5.0 years	Kanner et al.2013
QUELC	**3**	$\delta^{18}O_{ice}$	13.93°S	*289.17°E*	1.0 year	Thompson et al. 2013
ALH+CUR4	**4**	$\delta^{18}O_{cal}$	15.20°S	303.20°E	0.6 year	Novello et al. 2016
JAR1+JAR4	**5**	$\delta^{18}O_{cal}$	21.08°S	304.42°E	2.5 years	Novello et al. 2018
BOT	**6**	Sr/Ca	27.22°S	310.85°E	0.2 years	Bernal et al. 2016
CRT	**7**	$\delta^{18}O_{cal}$	24.58°S	311.42°E	2.7 years	Vuille et al. 2010
TMO	**8**	$\delta^{18}O_{cal}$	16°S	47°W	3.6 years	Wortham et al. 2017
SBE3+SMT5	**9**	$\delta^{18}O_{cal}$	13.81°S	*313.65°E*	1.2 years	Novello et al. 2018
DV2+TR5+LD12	**10**	$\delta^{18}O_{cal}$	12.36°S	318.43°E	4.0 years	Novello et al. 2014
PAR01+PAR03	**11**	$\delta^{18}O_{cal}$	4°4'S	*55°27'W*	7 years	Wang et al. 2017
PUM	**12**	$\delta^{18}O_{cal}$	10.07°S	*76.06°W*	1 year	Bird et al. 2011

The #6 – BOT (Botuverá) is the only data where the amount effect is not dominant (Bernal et al., 2016). This speleothem is located at the edges of the SAMS, where two precipitation peaks are annually observed. One peak during the summer season (DJF) and another during the austral winter (JJA). Due to this double precipitation peaks and the fact that the summer and winter precipitation come from different sources, the $\delta^{18}O$ at this site does not represent the annual or the summer precipitation variability. Another data located near the edges of the monsoon and near the BOT data, is the CRT1 data (#7) (Vuille et al. 2010), located at the São Paulo state, where the dominant precipitation signal is during the summer months, presenting just only one precipitation peak in the summer.

An alternative to the $\delta^{18}O$ isotope is the use of the Sr/Ca trace element as precipitation proxy (Bernal et al., 2016; Fairchild et al., 2012). Several geochemical process like, calcite precipitation, calcite dissolution or mixing of two or more sources, can modulate trace elements variability (Bernal et al. 2016). However, the process linked to the atmosphere is the precipitation. Following Fairchild et al. (2012), the aquifer vadose zone above the cave favours calcite precipitation, allowing CO_2 degasification from the soil fissures, leading to the enrichment of trace elements, such Sr, Ca and Mg, during dry periods, which makes these trace elements suitable precipitation proxies, which do not depend on the source effect.

The raw 12 $\delta^{18}O$ isotopic time series is presented in fig.3.2. Some time series are compositions of two or more records, represented by the assorted colours. Just observing to the raw time series data we can see some common characteristics like $\delta^{18}O$ depletion during the LIA (AD 1450 – 1850) in the Andes records (fig.3.2a,b,c,l) as well as in the south-eastern and mid-eastern South America records (fig.3.2e,g) and the opposite in the Southern Tropical South America (fig.3.2f) where some lags and leads are seen in relation to rainy and dry periods, and the Brazilian Northeast and Eastern Amazonia speleothems (fig.3.2i,j,k), revealing an implicit spatiotemporal pattern.

Also, in fig.3.2 the dating uncertainty of some records is showed by the error-bars plotted on the left side of the isotopic time series. As one can see most of the speleothems are very well dated, presenting small dating errors. However, some speleothems like the Palestina, Pau d'alho and Jaraguá caves records (fig.3.2a, d, e) have perceptible uncertainties, especially as the age increases (as back to the past).

To take into account the age uncertainty in the isotopic time series analysis, Anchukaitis and Tierney (2012) suggest the use of the Monte-Carlo simulation on the age-depth model, through the use of a gaussian random number generator accounting ±1σ age uncertainty in each individual record across the simulations . A recent study by Deininger et al. (2017) applied the same technique over 12 speleothems in the Europe, North of Africa and Mideastern, to retrieve past temperature variations over the European continent associated to the North Atlantic Oscillation (NAO) and other climate patterns. In the next section the Monte-Carlo method for the records' age-depth model is presented.

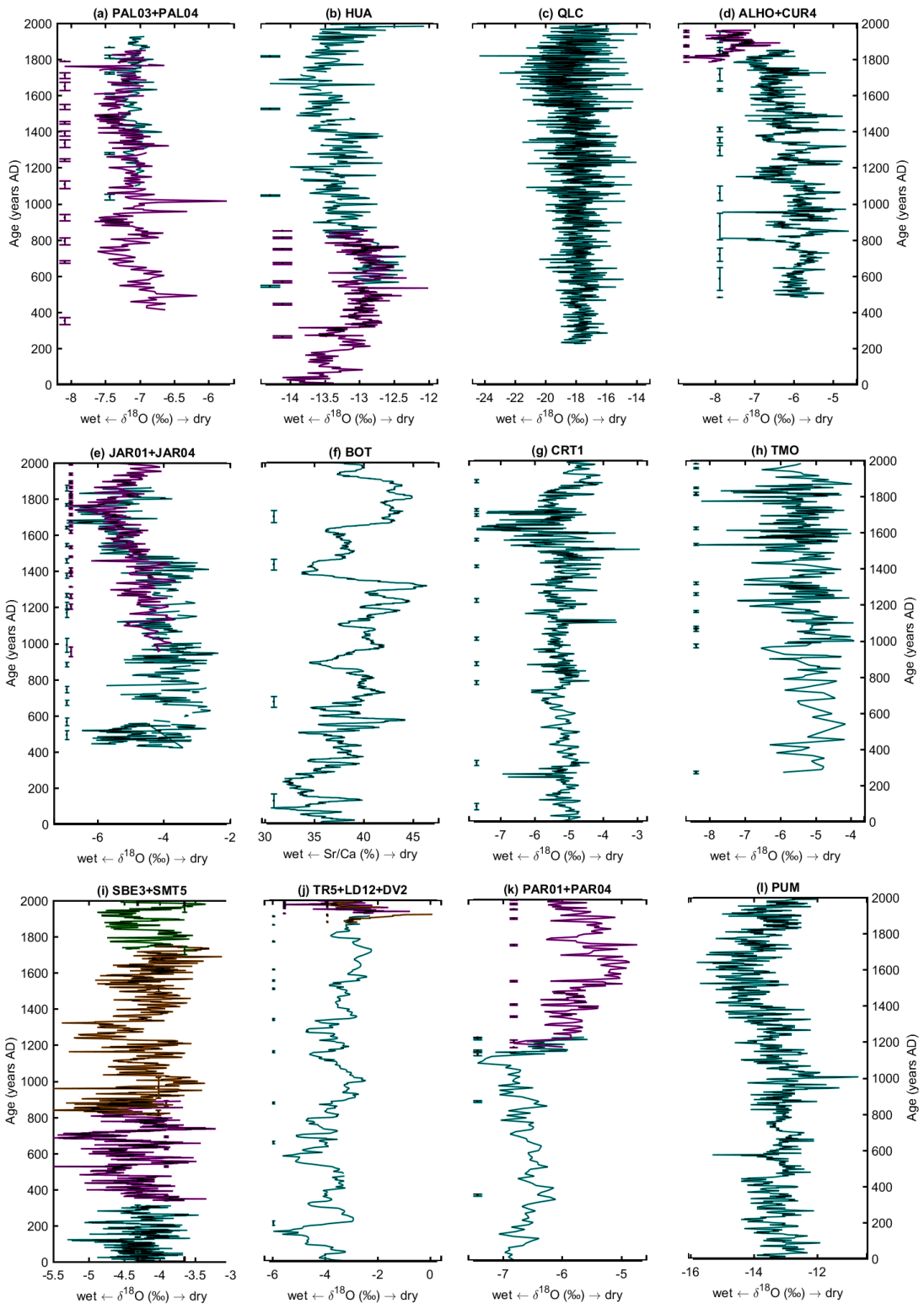

Figure 3.2 – $\delta^{18}O$ isotopic timeseries raw data. *Some time series are composed by two or more records sampled on the same or nearest place. The vertical error bars denote points where U/Th isotopes are sampled in order to date the sample.*

3.2 - Monte-Carlo Method Age-Depth Model

Most of our records are dated using U/Th relationship, sampled along the speleothems' growth axis. Uranium is transported through the groundwater incorporated into the speleothem decaying to Thorium (Fairchild et al. 2012). Assuming, that there is not transport of Uranium or Thorium after incorporated to the speleothem, the U/Th isotopic relationship becomes suitable to dating this type of sediment (Fairchild et al. 2018).

To take into account the records' age uncertainty, a random gaussian number generator (assuming that the error has a gaussian distribution [Bayesian approach, see Anchuaitis and Tierney, 2012]) were used to generate age values within the range of ±1σ, thus the ages were interpolated using a linear model. This procedure is repeated 1000 times generating 1000 isotopic time series for each sample. The age model simulations results are shown in fig. 3.3, where the error-bars denotes the ±1σ age uncertainty and the shaded lines represent the Monte-Carlo age-depth model dispersion, an approach similar to the used by Anchuakaitis and Tierney (2012) and Deininger et al. (2016).

Some ages sampled over a given speleothem can present distortions as age inversions or larger uncertainty, like the TR5 speleothem (fig.3.3k). In this case our routines do not account this age, evaluating the linear regression to the next age.

The proxy time series were obtained through interpolation of the new ages obtained from the Monte-Carlo age model simulations to the original isotopic series sampled in each speleothem or stratigraphic depth. From this process, 1000 proxy time series is obtained for each sample.

In the 4th column of table 3.1, the mean sampling for each paleoclimatic record is presented. As one can observe, the records have different sampling rates or temporal resolution. To evaluate the Principal Component Analysis, it is necessary that all data have the same temporal resolution. To equalise the time resolution, the records were

upsampled to the annual time scale using a cubic spline, resulting in a new resampled set of climate proxies.

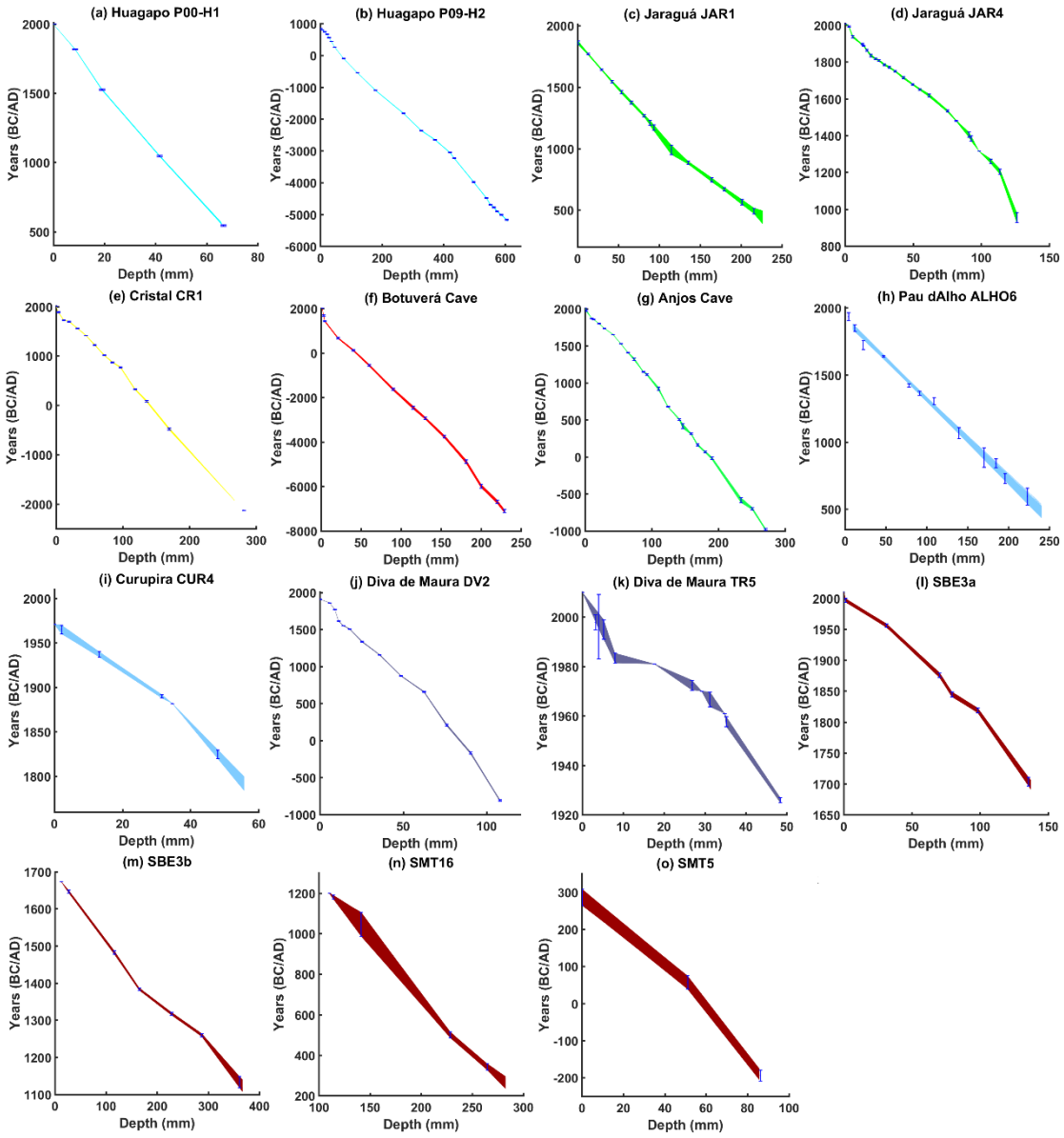

Figure 3.3 - Age-depth models for all speleothems *used in this work. Shaded lines represent the 1000 Monte-Carlo simulations linear models performed on the isotopic time series and error bars represent the dated age for each depth with ±1σ (standard deviation) representing the dating uncertainty.*

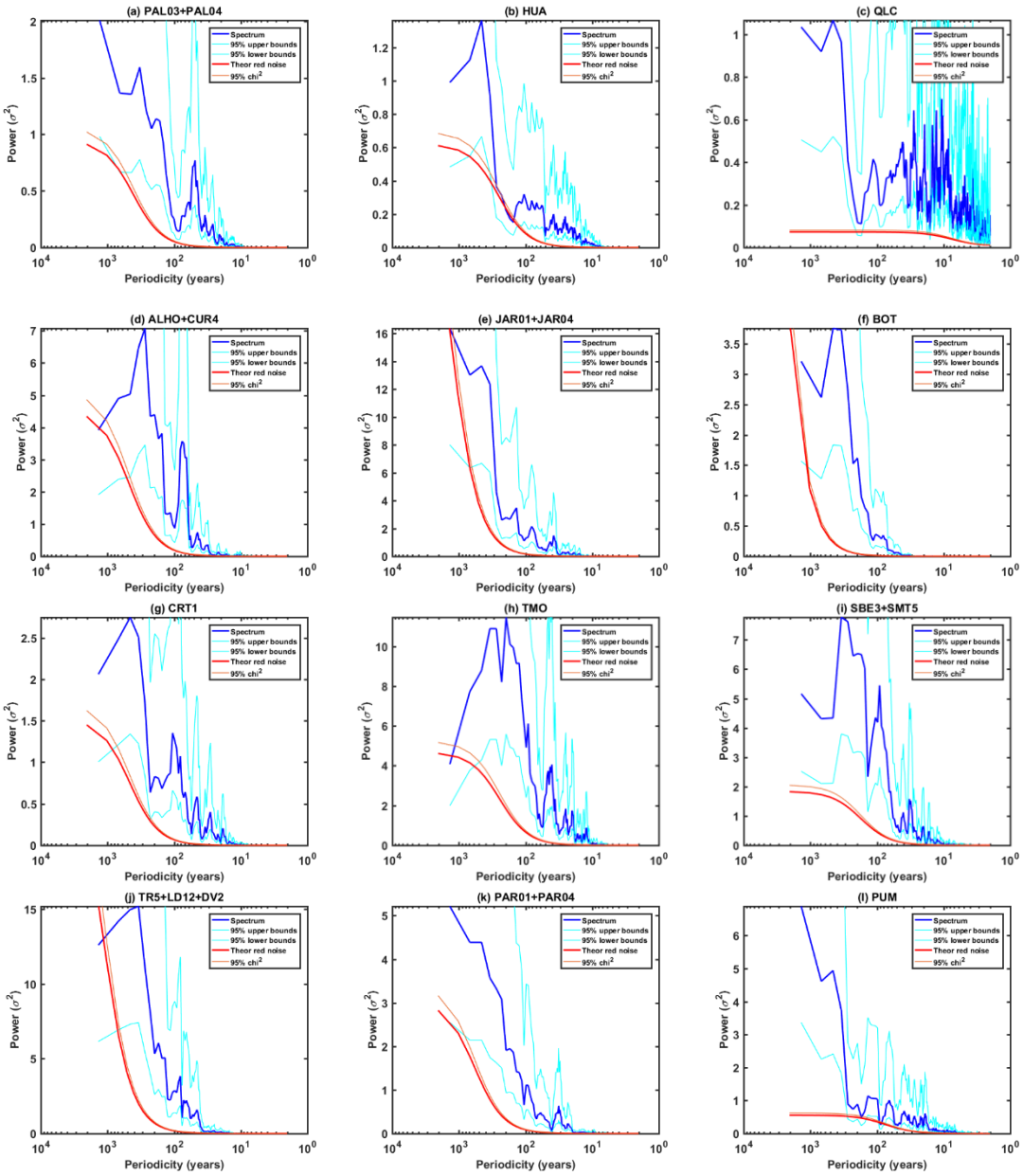

Figure 3.4 – Multi-taper Power Density Estimate for the South America Climate Proxies*. The blue curve represents the time series power density estimate, the heavy red line represents the theoretical red noise estimate, the cyan and the lighter red curves represent the 95% bounds of the time series and red noise estimates respectively. Only values above the red curve can be considered statistically significant at the level of 95% or different from the red noise.*

Records which are composed by two or more samples, were joined through the following procedure: the overlapping period among the samples are found and taken, forming subsamples, these subsamples are detrended and normalized into a unitary variance, so the sample mean among the time series is evaluated, forming a new "averaged time series". Thus, this "averaged time series" is reconstructed by multiplying

the standard deviation and by the addition of the sample mean and the trend of the longer time series and it is placed back to the record data, forming the complete proxy time series.

Inspecting fig.3.2, it is possible to see that each climate proxy represent the monsoon in different time scales, as in the Huagapo or Quelcaya ice cores (fig.3.2.b,c) which represent the climate with very high temporal resolution, or in others like the Iraquara and Paraiso speleothems (fig.3.2j,k) which represent lower frequency climate signals.

Spectral analysis using the multi-taper power density estimate method were performed on the median of the resulting Monte-Carlo time series, as shown in fig.3.4. As expected, all the records present a strong red noise and significant variances after decadal time scales (or lower frequencies than decadal time scales), revealing that the South America proxy records are suitable to study decadal to multidecadal and centennial climate variability. However, some records represent the climate variability lower than multidecadal climate variabilities, such as the speleothem JAR, ALH, PAR, BOT (fig.3.4d,e,j,k), on the other hand, others do not show higher variance in multidecadal time scales like the speleothems PAL, ALH, TMO and SBE (fig.3.4a,d,h,i).

Before the PCA evaluation, it is desirable that allrecords represent the same variabilities or climate signals. In order to overcome this constraint, all the climate records were low pass filtered using Fourier series at the band with frequency at 1/30 $years^{-1}$. This value was chosen because the low frequency data started to show significant Power Density Estimate signals after this band. To overcome this problem, Deininger et al. (2017) just resample their speleothems to 30 years, using a Gaussian kernel, a type of time series filter. However, the European speleothems have lower time resolution than the South American speleothems, and their dating uncertainties are larger.

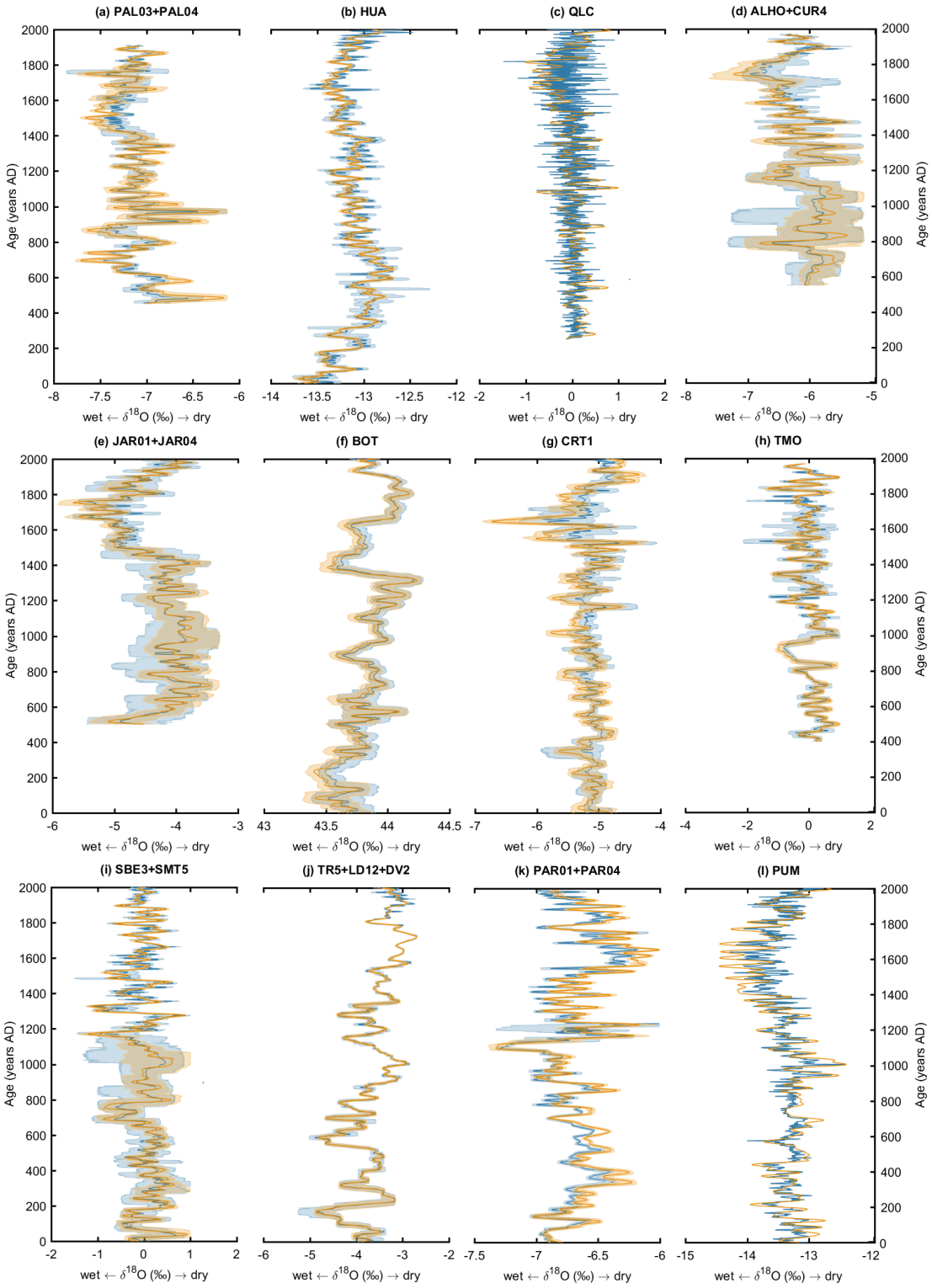

Figure 3.5 – Speleothems $\delta^{18}O$ isotopic time series after the Monte-Carlo simulations. *The blue and orange represent the time series before and after 30 years low pass filtering. The shaded around delimits the upper and low quartile.*

In fig.3.5, the $\delta^{18}O$ time series is presented after the Monte-Carlo simulations. The blue curve represents the median of the 1000 Mont-Carlo simulations and the around shaded represents the dispersion of the simulations, delimited by the 25^{th} and 75^{th} quantiles. Speleothems that has the dating sampling rate lower or with overlapping points of two or more samples, presents the higher uncertainties. Also, in fig.3.5, the orange line represents the speleothems data after low pass Fourier filtering. The normalized and detrended data were filtered and then reconstructed, by inverting the normalization and the detrending process. As one can see, the filter does not distort the time series substantially in order to cause issues in the interpretation or in the data compilation. So, these filtered time series are used in the principal component evaluation.

As one can see in table.3.1 the isotopic data have different time spans, so in this analysis, just the period of AD 600 to AD 1970 is used. This period was chosen due to it cover the main last millennium climate events, such as the LIA and the MCA, and to it is the common overlapping period among the records after the Monte-Carlo Simulations.

3.3 – Monte-Carlo Principal Component Analysis

The $\delta^{18}O$ and trace elements time series have not a uniform value across the South America, due to the Rayleigh distillation process (Table 3,1 references). So the correlation instead of the covariance data matrix is used to evaluate the Principal Component Analysis (see Willks, 2018).

Random time series for each speleothem record is chosen among the Monte-Carlo simulations and then Principal Component is performed, resulting in loadings coefficients, or the spatial pattern, Principal Components or amplitudes of the coefficients and the eigenvalue spectrum. This procedure is evaluated up to all 12000 Monte-Carlo time series is used.

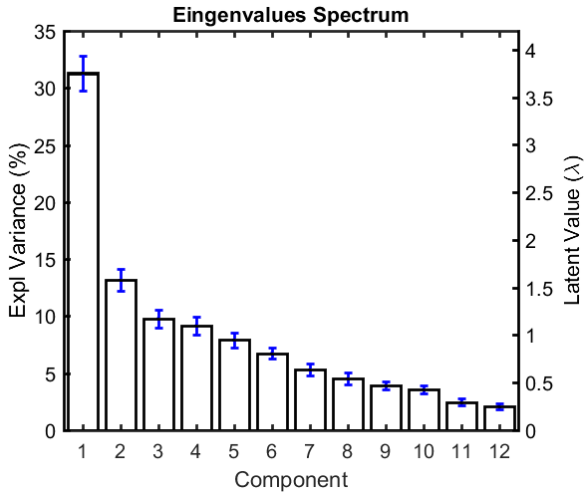

Figure 3.6 - Monte-Carlo Principal Component Eigenvalues Spectrum or Explained Variance*. The vertical bars represent the explained variance, or the latent values and the error bars represent the inter-sample variability and the Monte-Carlo simulation dispersion as a measure of uncertainty.*

Each component represents certain amount of data variability, with the first components representing the greater amount of variability, degenerating to the others. Infig.3.6 the eigenvalues spectrum or the explained variances is represented by the vertical black bars and the blue error bars representing the uncertainty in the eigenvalue or in the explained variance computed through "*the North's et al. rule of thumb*" (North et al., 1982).

To account the eigenvalue uncertainty and the Monte-Carlo simulations dispersion, the following formula is used to compute the error-bars:

$$e_\lambda = \lambda \sqrt{\frac{2}{n}} + \lambda_{IQR} \qquad (eq.3.1)$$

where the e_λ represent the error, λ represent the eigenvalue or latent value, n represent the number of observations and λ_{IQR} represent the Interquartile range of the eigenvalues Monte-Carlo simulations.

Our approach to define the number of simulations differs from the Deininger et al. (2017) and Deininger (2013) that used the number of Monte-Carlo simulations based on the eigenvalues' convergence. They found convergence after 2000 simulations. However, the period span of Deininger et al. (2016) work is greater than ours backing to

the Last Glacial Maximum and their speleothems dating uncertainty is greater than the South America ones.

The corresponding loadings or coefficients (eigenvectors) obtained from the Monte-Carlo Principal Components are represented by the boxplots in the fig.3.7. and in the Table.3.2. As one can see after the 3rd component, the loading coefficients dispersion becomes larger as the explained variability degenerates. This occurs because the lower frequency signal are retained in the firsts components due the strong red noise present in the time series, and the higher frequency signal(records) are retained in the lasts components where the uncertainties are larger.

***Table 3.2 – Monte-Carlo Principal Component Loading coefficients or factors**. Due to the simulation results do not follow a gaussian distribution, the median of the values was used instead the sample mean. For the explained variance and latent values (2nd and 3rd columns from left to right), the value between brackets represent the eigenvalue uncertainty estimated with the north's et al. rule of thumb (North et al, 19…) plus the Inter-quartile range of the Monte-Carlo simulations, for the speleothems loadings, the value between brackets represent the Inter-Quartile Range of the Monte-Carlo simulations.*

	λ	HUA	JAR	CRT	BOT	TMO	ALH	DV2	SBE	QLC	PAL	PAR	PUM
1stPC	3.7(2)	0.37(1)	0.45(1)	0.21(1)	-0.11(2)	0.12(1)	0.36(1)	-0.31(1)	-0.03(3)	0.13(1)	0.34(1)	-0.31(1)	0.36(1)
2ndPC	1.6(1)	-0.09(3)	0.03(3)	-0.28(5)	0.49(5)	0.08(1)	0.04(4)	0.17(4)	0.35(8)	0.56(3)	-0.22(3)	-0.20(3)	0.32(2)
3rdPC	1.2(1)	-0.0(2)	0.06(5)	-0.1(1)	-0.5(2)	0.2(7)	0.1(1)	0.3(2)	0.6(3)	-0.1(4)	-0.0(3)	-0.1(2)	0.0(1)
4thPC	1.1(1)	0.1(1)	-0.03(9)	-0.1(1)	0.2(6)	0.6(3)	0.1(2)	-0.2(4)	0.1(6)	-0.3(1)	-0.2(1)	0.2(2)	0.1(1)
5thPC	0.95(9)	0.46(5)	-0.09(6)	-0.4(2)	-0.0(1)	-0.4(1)	-0.3(1)	-0.28(9)	0.3(1)	-0.04(9)	0.10(9)	0.3(1)	0.24(7)
6thPC	0.81(7)	0.1(1)	-0.13(5)	0.7(1)	0.21(1)	-0.1(1)	0.0(1)	0.15(9)	0.3(1)	0.00(9)	-0.0(1)	0.4(1)	0.23(6)
7thPC	0.64(7)	0.02(1)	-0.05(7)	-0.1(2)	-0.10(8)	0.45(9)	-0.3(3)	0.2(1)	-0.1(1)	0.36(7)	0.55(9)	0.3(2)	0.0(1)
8thPC	0.54(7)	0.1(2)	-0.0(1)	-0.2(1)	-0.1(1)	-0.1(2)	0.6(2)	0.3(3)	-0.3(2)	0.0(3)	-0.1(3)	0.4(2)	0.1(2)
9thPC	0.47(5)	-0.4(3)	-0.0(2)	-0.1(1)	0.1(2)	-0.0(1)	0.2(5)	-0.4(7)	0.2(4)	-0.1(5)	0.3(3)	0.1(5)	-0.1(6)
10thPC	0.43(4)	0.1(6)	-0.1(3)	-0.1(2)	0.2(5)	-0.0(1)	-0.1(4)	0.2(3)	-0.2(3)	-0.4(7)	0.3(10)	-0.1(2)	0.3(4)
11thPC	0.30(4)	-0.4(1)	-0.3(4)	0.02(8)	-0.43(9)	0.06(7)	-0.1(1)	-0.3(1)	-0.12(7)	0.1(2)	-0.2(1)	0.1(2)	0.6(1)
12thPC	0.25(4)	-0.3(2)	0.8(1)	-0.06(6)	0.0(3)	-0.08(6)	-0.2(1)	0.1(1)	-0.0(1)	-0.2(1)	-0.1(2)	0.29(7)	0.2(3)

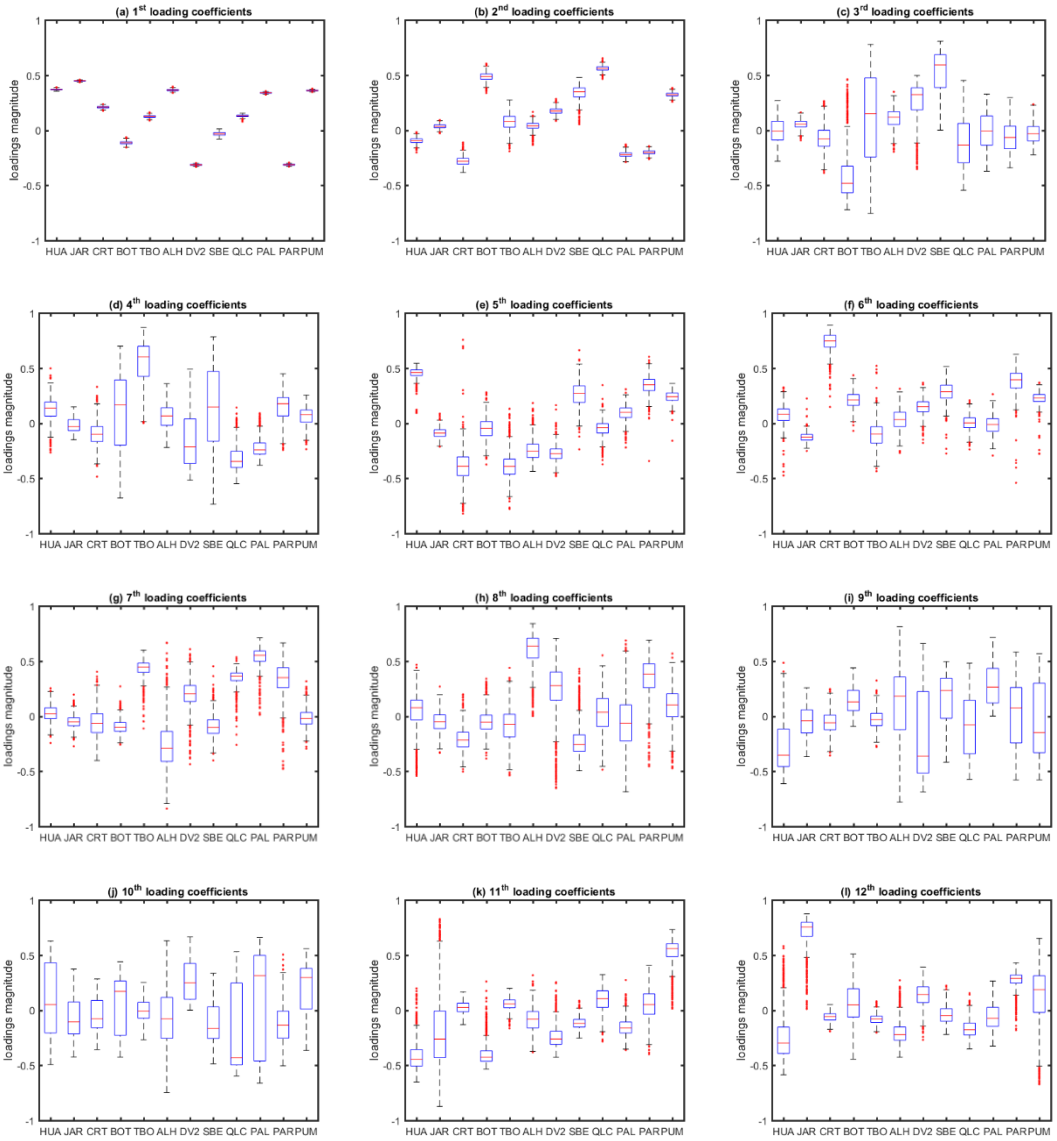

Figure 3.7 - Monte-Carlo Principal Component Analysis - Loading coefficients boxplots*. The box and whiskers represent the dispersion of the 1000 simulations. The greater is the box and the whiskers, the greater is the uncertainty of the loading.*

Fig.3.8 shows the loading coefficient spatial patterns. The dots represent the records location, the size of the dots represent the magnitude of the loading coefficients, shown in table 3.2 and by the horizontal red mark of the boxplots in the fig.3.7. The dot colours red and blue represent positive and negative loading signals, respectively. For example, the 1st Principal Component pattern, hereafter referred as 1st $PC_{\delta}{}^{18}{}_{O}$, presents a dipole structure northeast-southwestward oriented.

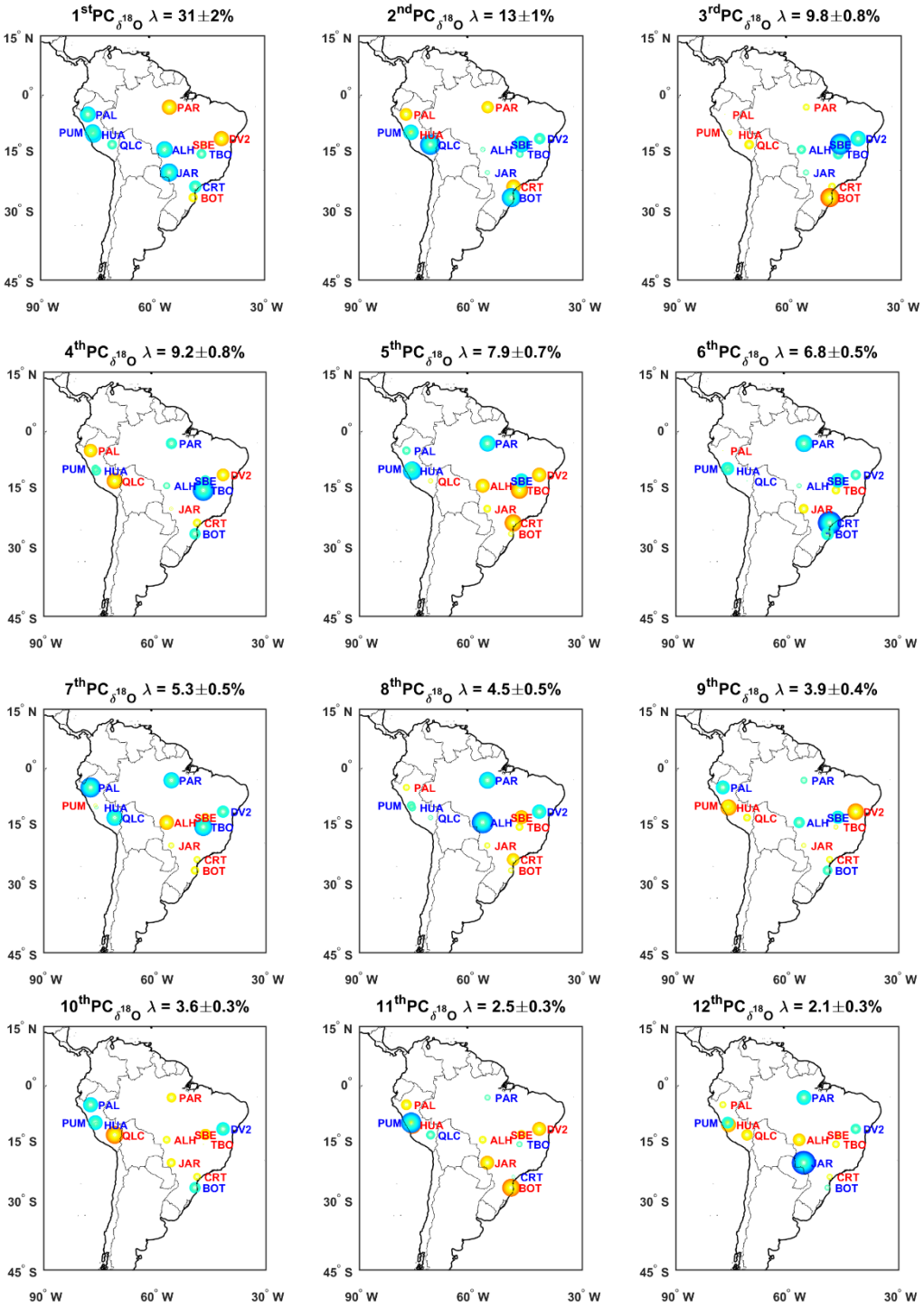

Figure 3.8 - Monte-Carlo Principal Component Analysis Loading Coefficients Spatial Distribution*. The size of the dots corresponds to the loading's magnitude, warm colours means positive loadings and colder, negative ones or $\delta^{18}O$ enrichment and impoverishment respectively. The magnitude of the loadings was computed through the extraction of the median of the 1000 Monte-Carlo simulations.*

It can be observed that some components form a cluster or a spatial pattern like the dipole pattern seen in the 1st $PC_{\delta}{}^{18}O$, the 2nd $PC_{\delta}{}^{18}O$ and the 5th $PC_{\delta}{}^{18}O$, while others

form a more diffuse spatial pattern. In some works like Kaiser (1960) suggested to retain only modes with eigenvalue greater than the unity, but Cattel (1966) suggested to look the slope of the eigenvalues. Other approaches like Monte-Carlo methods (Preisendorfer and Mobley, 1988) are more rigorous in assess the statistical significance of the patterns. However, the orthogonality constraints of the PCA can limit the analysis of the physical processes. So, in this work we will consider a Principal Component significant considering the likelihood to well-known physical observed patterns, which is the subject of the next chapter.

The respective Principal Components scores or amplitudes representing the temporal evolution of the spatial patterns is represented in fig.3.9, where the heavy lines represent the median of the 1000 Monte-Carlo simulations and the around shaded represents the upper and lower quartile, indicating the dispersion of the components.

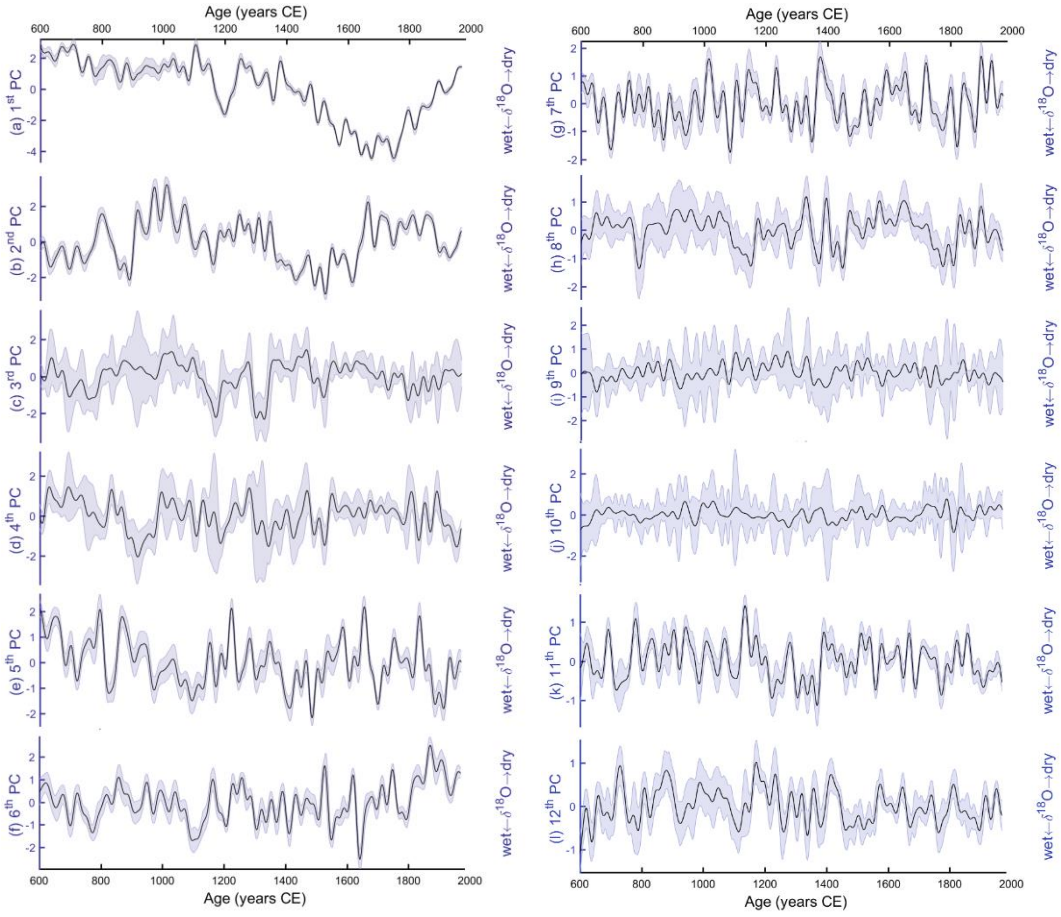

Figure 3.9 - Monte-Carlo Principal Component Scores or Time Series. *The shaded around represents the upper and lower quartile of the Monte-Carlo Simulations and the heavy curves represent the median of the simulations.*

Most of the Principal Components present a clear red noise or low frequency structure, as expected in any longer proxy climate time series. As one can see in the loading coefficients, as the representativeness of the mode degenerates the uncertainties becomes higher, as shown by the shaded curves around the median of the Monte-Carlo Principal Component. Thus, this result suggests that possibly the 1st and 2nd Principal Components may have "physical significance" associated to an observed precipitation pattern.

3.4 – Conclusions

The compilation of 12 well dated $\delta^{18}O$ and Sr/Ca records precipitation proxies is presented, resulting in a set of 12 spatial patterns. Following Cattel (1966), just 4 components can be considered statistically significant and following the box plot analysis, just the first two Principal Component modes present lower dispersions in the loadings coefficients, suggesting that possibly these components can be representing some observed precipitation or circulation pattern. The same is observed to the associated time series or scores, where just the first three leading modes presents lower dispersion along their extent as compared to the other components.

Chapter IV

South America Paleoclimate Records Spatial Coherence and Last Millennia Monsoon Variability

Principal Component Analysis provides a set of spatial modes that sometimes do not have physical interpretability or "significance", in the palaeoclimatological context due to the extent or time resolution of the proxies' time series. It is not always possible to compare proxy to observed data. In our analysis some of the time series span before 1980 and have multidecadal time resolution, just allowing comparisons of linear trends.

One way to compare proxies to observations is by verifying whether their spatial pattern is coherent or not. In this chapter we present the coherence between the $PC_{\delta^{18}O}$ spatial pattern to the Empirical Orthogonal Function of the precipitation derived from the reanalysis data, where the physical (e.g. climatological) interpretation of the $PC_{\delta^{18}O}$ modes is provided.

The coherency between last millennium precipitation proxy to the industrial period precipitation is shown in the first part, afterwards a comparison among various South America precipitation proxies is provided.

4.1 – $\delta^{18}O$ and Trace Elements South American Records Spatial Coherency

4.1.1 – Low Frequency Patterns in the Current Warm Period

In order to become the reanalysis data "frequency" coherent to the paleoclimate records data, extended summer means were computed (October – March) from the monthly means, resulting in 110 summer annual means. As for the proxy data, a 30 years Fourier low pass filtered was evaluated in each grid point, resulting in our low frequency reanalysis data.

Studies comparing model output or gridded data to weather/climate stations data, generally compares the observational data to the corresponding gridded time series. However, models and reanalysis data can misrepresent or displace spatially some climate modes and sometimes they are not able to represent small scales weather events due to the coarser spatial resolution or parametrizations, which can lead to values far from observations (Benestad et al. 2018). A better approach to overcome this problem is the comparison of observed climate modes to climate modes based on reanalysis or earth system models (Benestad et al. 2018). Thus, this approached is used in this section.

Due to data availability the variable Total Column Rainwater (TCRW) is used in place of total precipitation, that is only available for forecast products. Thus, Principal Component Analysis were evaluated over the correlation matrix of the low frequency TCRW data on the spatial domain of -30°S, 0° and -60°W, -30°W, a similar region to that used by Silva et al. (2007) in the evaluation of their monsoon index.

The resulting TCRW patterns or EOFs are shown in the fig.4.1, where the shaded represent the correlation between the principal component to the low frequency TCRW data, and the circulation field was obtained through the correlation between the principal component to the 850hPa zonal and meridional wind.

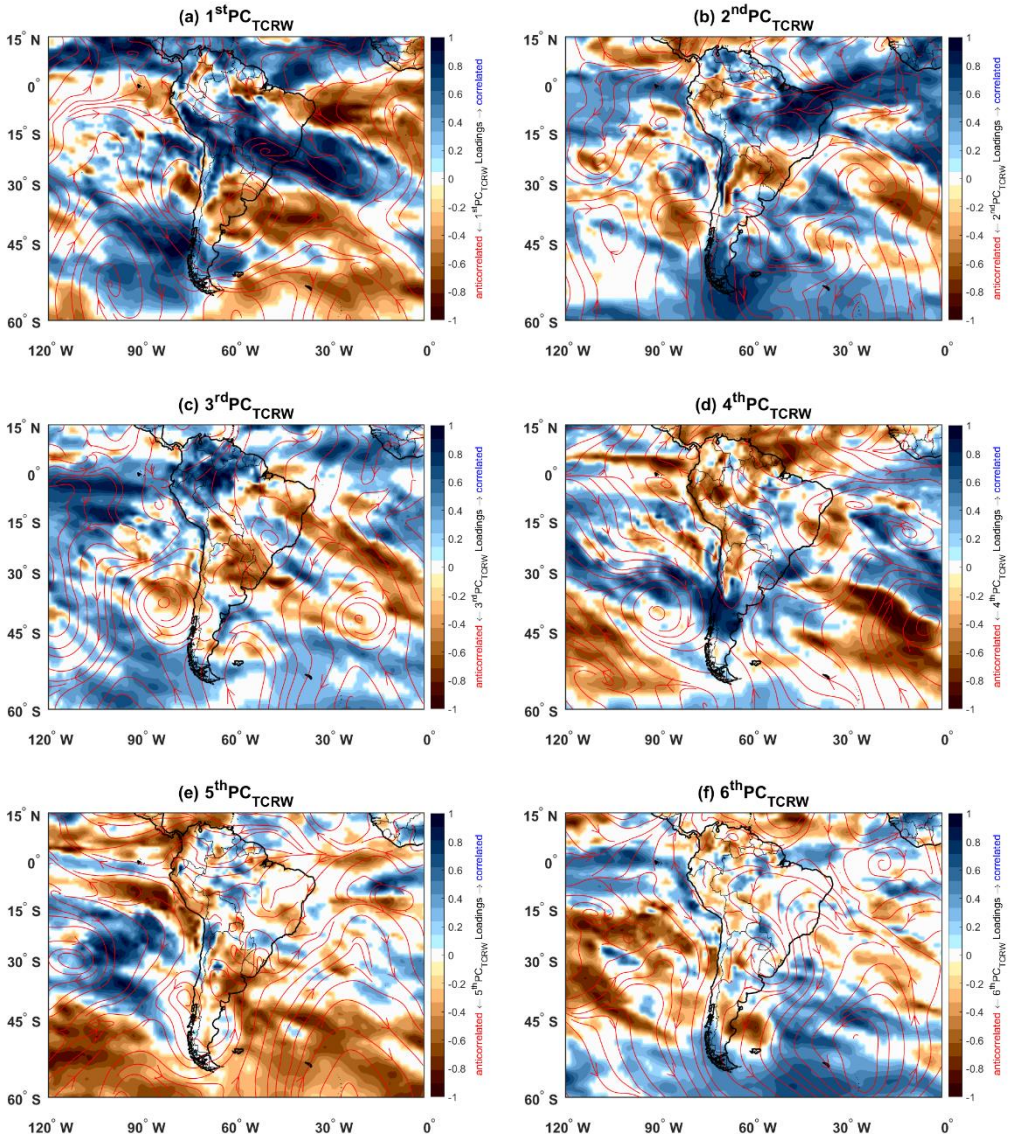

Figure 4.1 - Low Frequency South America Leading Variability Modes*. The shaded represent the correlation of the Principal Component to the TCRW variable. The streamlines represent the correlation of the PC to the 850hPa circulation.*

The first pattern (fig.4.1a) in its positive phase, presents a tri-pole structure between the monsoon domain to the Southeast South America (SESA) region and to the Brazilian Northeast region. Observing the circulation pattern, it is observed over the monsoon domain a cyclonic circulation denoting low level air convergence, contrasting to the SESA region and to the Northeast of Brazil (NEB). So, this mode will be taken as the monsoon mode.

The positive phase of the second pattern (fig.4.1b) presents a dipole pattern between the north and south portion of Brazil. On the north portion of Brazil, the

positive TCRW anomaly is associated to a cyclonic circulation over the continent and low-level wind convergence over the Northeast region.

The third pattern (fig.4.1c) in the TCRW field also shows a tri-pole pattern but southward displaced in relation to the 1st PC_{TCRW} pattern, presenting contrasts between the SACZ domain to the Northeast of Brazil and to the Southeast South America (SESA) region. This pattern also shows cyclonic/anticyclonic circulation between the SACZ and SESA domains, resembling episodes of southward displacements of the South American Low-Level Jets (SALLJ), called here Low- Level Jets episodes. The negative phase of this mode carries humidity flux from Amazonia to the SESA region, as noticed from the streamlines, favouring convection over this region (Salio et al. 2002; Jones and Carvalho et al. 2018; Marengo et al. 2004).

The other modes do not show clear spatial patterns. Therefore, we will limit our analysis to the three leading modes, where just two of them are coherent to the isotopic based principal components, as it will be discussed afterwards. A figure showing the contribution of the modes is provided in the appendix section (fig.A.2.1).

4.1.2 – South America Last Millennium Records' Coherency

From chapter 3, following the statistical significance criterion accounting the uncertainties in the latent values or in the eigenvalue's spectrum ($\lambda > 1$, Cattel. 1960), just four components can be considered statistically significant. Yet, through the Monte-Carlo simulations, based on the loading coefficients, just the first two leading modes present low uncertainty on the loading coefficients. Therefore, just the first two $PC_{\delta^{18}O}$ is considered here to analysis.

In order to find "physical significance" of the $PC_{\delta^{18}O}$. The $PC_{\delta^{18}O}$ spatial loading patterns are compared to the spatial patterns derived from the PC_{TCRW} and they are shown in fig.4.2. The 1st $PC_{\delta^{18}O}$ mode is found coherent to the 1st PC_{TCRW} mode. The paleoclimate records pattern forms a dipole between the monsoon region, represented by the speleothems CRT1, JAR, ALH, TMO to the speleothems DV2 and PAR, (see fig.3.9 and table 3.1), as it is emphasized by the different colours and by the size representing

the intensity of the coefficients or “weight of the loadings”. This pattern is coherent to previous studies like Novello et al. (2018) and Novello et al. (2012) showing the Northeast of Brazil speleothems in antiphase to the Andes speleothems. Wang et al. (2017) points toward a see-saw between $\delta^{18}O$ eastern Amazonia speleothem PAR01 to the western Amazonia speleothems in time scales greater than the multidecadal and spanning to periods greater than the studied in this work, but it is also observed in the last millennium as shown in Fig.4.2. In this work we interpret this pattern as the monsoon mode.

The 2nd $PC_{\delta^{18}O}$ spatial pattern is found coherent to the 3rd PC_{TCRW} spatial pattern, shown in the fig.4.2b. The 2nd $PC_{\delta^{18}O}$ presents stronger negative loadings coefficients (blue coloured dots) for the Andes, Brazilian Northeast records and BOT records (South of Brazil), and stronger positive loading coefficient for the CRT1 record (Southeast of Brazil), contrasting to the BOT record, which presents a different precipitation regime (see section 3.1). This mode weights the precipitation or the climate proxies towards the edges of the monsoon, resembling the see-saw between the SACZ region to the Northeast of Brazil (NEB) and SESA regions, with stronger LLJ episodes (Jones & Carvalho et al., 2018; Marengo et al., 2004). Thus, in this work, this mode is interpreted as SESA/NEB mode or edges of the monsoon, representing the variability of the shape of the SAMS.

The corresponding Principal Components or amplitudes of the patterns are shown in fig.4.3, representing the standing oscillations of the $PC_{\delta^{18}O}$ spatial patterns. In order to find any regime shift periods, a change point detection algorithm based on the sample means (Lavielle, 2004) was applied to the $PC_{\delta^{18}O}$ time series and it is represented by the assorted colours and by the horizontal dotted lines.

For the 1st $PC_{\delta^{18}O}$, three distinct periods were found, the Medieval Climate Anomaly (AD 724 -1160), the Little Ice Age (AD 1489 -1878) and the transition between the MCA and LIA, called TRANS or Transitional Period (AD 1160 - 1489). The periods before the MCA, represented by the yellow colour, and the period after the LIA, the CWP, were not considered due they begin or end outside of the time series span, and we cannot define a start or ending date for them, respectively. For the 2nd $PC_{\delta^{18}O}$, four climate periods were found, as indicated in the Fig.4.3 the Little Ice Age was divided into

two periods for this time series, the LIA1 representing negative $PC_{\delta^{18}O}$ variability and the LIA2 the positive $PC_{\delta^{18}O}$ variability.

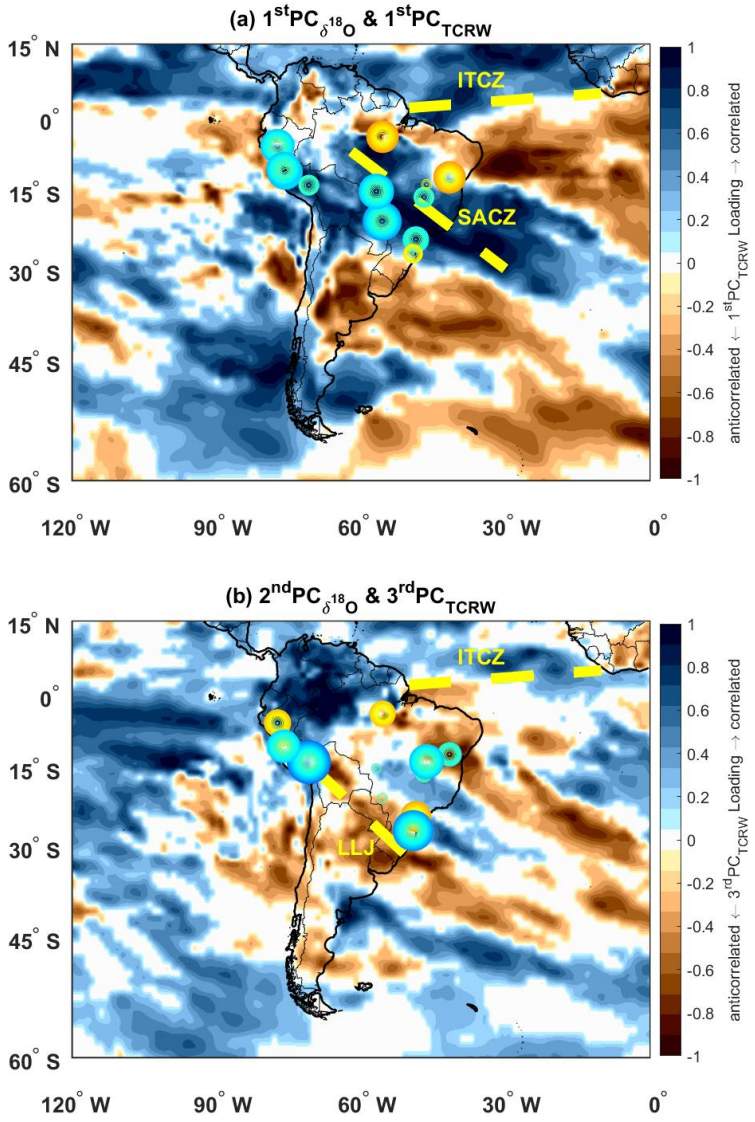

Figure 4.2 – Speleothems' Coherency, *(a) 1st $PC_{\delta^{18}O}$ and 1st PC_{TCRW}, and (b)2nd $PC_{\delta^{18}O}$ and 3rd PC_{TCRW}. The dots as in the fig. 4.4 represent the $PC_{\delta^{18}O}$ loading magnitude with red and blue dots representing $\delta^{18}O$ enrichment and depletion respectively, and the shaded represent the PC_{TCRW} loading patterns represented here as the correlation between the Principal Component to the original gridded data. The yellow strips represent the South Atlantic Convergence Zone (SACZ), the Intertropical Convergence Zone (ITCZ) and the Low-Level Jet (LLJ).*

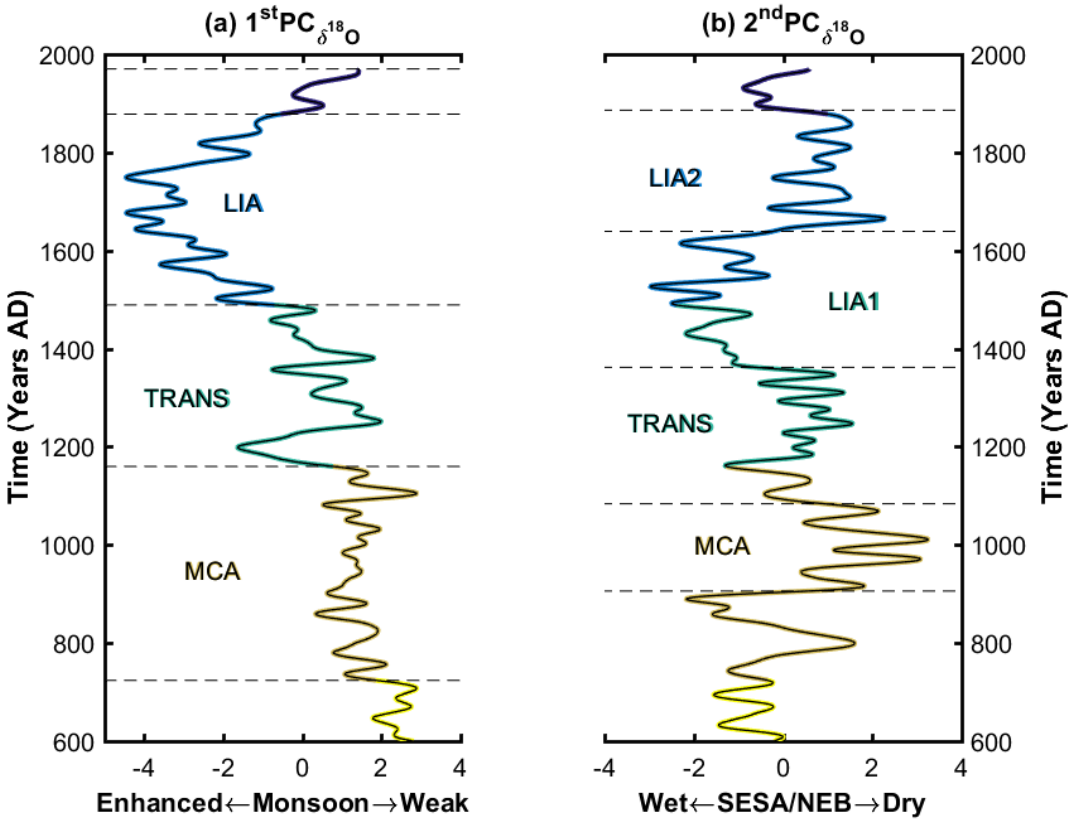

Figure 4.3 – Last Millennia South America temporal variability*. The coloured curves represent the isotopic Principal Components or amplitudes. The assorted colours represent changes in the sample mean or in the regimes evaluated through the automatic algorithm over the 1st $PC_{\delta^{18}O}$. The horizontal dotted lines also represent changes in the regimes, however evaluated over the respective time series.*

Table 4.7 – Climate Regime Shift dates*, in each cell it is represented the onset date of the climatic period. Cells which there is more than one value, represent regime shifts inside the given period*

	MCA	TRANS	LIA	CWP
1st $PC_{\delta^{18}O}$	AD 724	AD 1160	AD 1489	AD 1878
2nd $PC_{\delta^{18}O}$	AD 906	AD 1084	AD 1362,1639	AD 1886
NH (IPCC, 2013)	AD 950	AD 1250	AD 1450	AD 1850

In table.4.1 the regime shift dates are shown together to the IPCC Northern Hemisphere standard (IPCC, 2013), derived from various temperature proxies and Earth System Models output (IPCC. 2013; Jungclauss et al., 2017) over the Northern Hemisphere. Our results for the Southern Hemisphere agree to that found by Abram et al. (2016) who analysing various climate proxies on the Northern and Southern

Hemispheres shows that the Industrial period or CWP onset or LIA demise on the entire Southern Hemisphere lags the Northern Hemisphere counterpart.

The last millennium monsoon variability shown in the fig.4.3a, represents the climate variability during the LIA period as one can see through the substantial negative excursion of the 1st $PC_{\delta^{18}O}$ during this period, meaning wetter conditions in the blue dots (fig.4.2a) located along the monsoon axis or the SACZ region and drier conditions over the Brazilian Northeast, agreeing with previous studies, which pointed to a see-saw between the precipitation in the eastern and western portion of South America in multidecadal to centennial time scales (Novello et al. 2012, Novello et al. 2014)

The SESA/NEB variability mode shown in the fig.4.3b is representative of the records located over the monsoon borders, where positive excursion of the 2nd $PC_{\delta^{18}O}$ amplitude is found during the LIA2 and MCA period, meaning drying or a retraction of the monsoon shape during these periods over the NEB and SESA regions, and indicating a SALLJ less active or northwestward displaced, and drier conditions over the NEB. Positive 2nd $PC_{\delta^{18}O}$ values is found during the LIA1 period, which one can consider as the demise of the transition period and onset of the LIA period, representing a more active and southeastward SALLJ. This result agrees with the results found by Novello et al. (2018) and Novello et al. (2014), which found a drier period in the NEB speleothems during LIA, but neutral ones in the MCA and TRANS periods.

To improve the interpretability of the hidden structures revealed through the $PC_{\delta^{18}O}$'s, the compilation time series are compared to two others South American proxy time series. One representing the precipitation over the La Plata Basin, the sediment GeoB 13813-4 (Perez et al. 2016) and the other, a proxy of the past South America ITCZ variability, the Cariaco Basin sediment (Haug et a. 2001). Discussed in the next sections.

4.2 – South America Climate Proxies

4.2.1 – Sediment GeoB 13813-4 (Perez et al. 2016)

This record consists of a mud depocenter sediment collected over the La Plata river estuary, along the coast of Uruguay, located at 33°S and 53°W. Due to oceanic currents, this location is submitted to terrigenous sediment deposits from the La Plata river basin, like Ti/Ca, Fe/Ca and Al/Ca, showing signals of the LIA and MCA periods. The La Plata river fresh water plume also extends to this location, leading to variabilities in the contiguous seawater salinity as the La Plata river discharges. As the La Plata river integrates all the basin runoff because it is the exudate downstream of the basin. The count of fresh waters diatomaceous (biological activity) is used in this work as a proxy of the La Plata Basin precipitation.

Following Perez et al. (2016), about 70% of the Rio de La Plata discharge comes from the Paraná river which has most of its drainage basin on the SACZ domain, and because of this, Perez et al. (2016) interpret this proxy as a South America Summer Monsoon proxy (SASM).

However, the precipitation of the La Plata Basin is not only from the SAMS, but also from middle latitude transient weather systems (e.g. fronts and cyclones) propagating from higher to low latitudes, from SALLJ episodes and Mesoscale Convective System in higher frequencies time scales (e.g. daily to intraseasonal time scales).

In fig.4.4a, b the summer and winter precipitation are presenting together to the La Plata Basin (LPB) region. As one can see most of the precipitation over the LPB falls during the summer, except on its eastern side which falls during the winter. The raw time series of the sediment GeoB13813-4 is shown in the fig4.4c. It is interesting to notice this record shares a common signal with the 1^{st} $PC_{\delta^{18}O}$ during the LIA period.

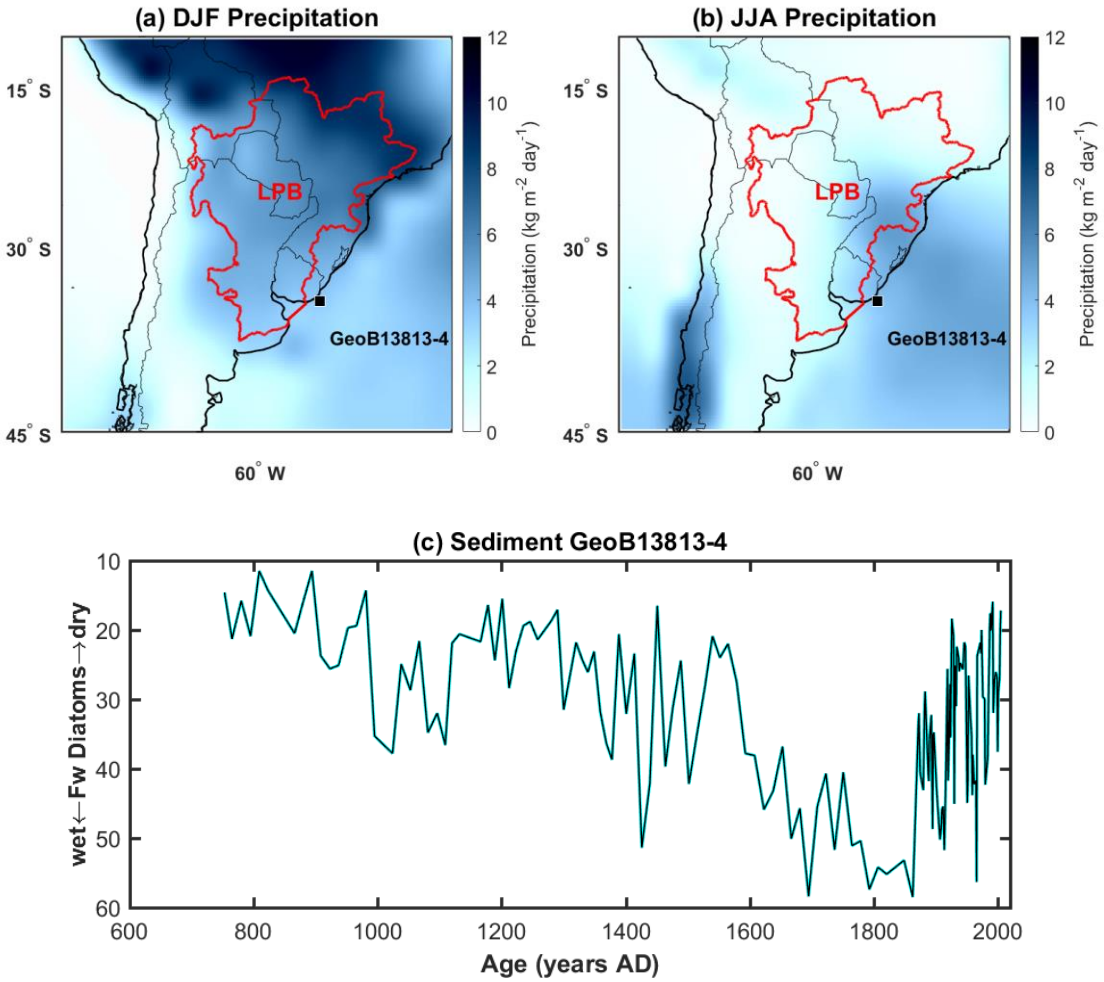

Figure 4.4 - La Plata River Basin precipitation and Sediment GeoB13813-4. *(a) Summer precipitation, (b) winter precipitation, extracted from 30 years (AD 1980-2010) of GPCP data, the red line delimits the La Plata Basin. (c) sediment GeoB13813-4 raw data, the cyan curve represents the freshwater diatoms account in (%). The location of the climate proxy is marked by the square in the map.*

4.2.2 – Cariaco Basin %Ti sediment (Haug et al. 2001)

The Cariaco basin data consists of an oceanic sediment collected on the maritime basin of Cariaco offshore of the Venezuelan coast located around 10°N, 65°W. Terrigenous trace elements like Fe (Iron) and Ti (Titanium) are sampled along the sediment core spanning about 14ka, in higher temporal resolution about 5 years.

The Fe as well as the Ti, reflect the continental freshwater input into the Cariaco basin. However, the Fe element suffers redox reaction through time and the Ti element is not sensible to the environment, thus in this work, the percentage of Titanium (%Ti) time series is used as precipitation proxy or terrigenous contribution on the Cariaco oceanic basin.

The main climate feature acting upon the Cariaco basin is the austral winter (boreal summer) ITCZ. Following Haug et al. (2001), as much as the ITCZ is displaced northward, the higher is the metal contribution into the Cariaco basin. In fig.4.5a, b it is shown the Cariaco basin location and the austral summer and winter precipitation climatology, respectively. As one can see most of the precipitation over the Cariaco basin that runoff into the basin, falls during the austral winter months (JJA) with a considerable contribution during the austral summer months (DJF). Comparisons to Andean lake sediments supports the hypothesis that the Cariaco basin metal concentration reflects the annual Atlantic ITCZ migration (Vuille et al., 2012; Novello et al., 2016). So, in this work we will take the Cariaco basin as an annual ITCZ migration proxy.

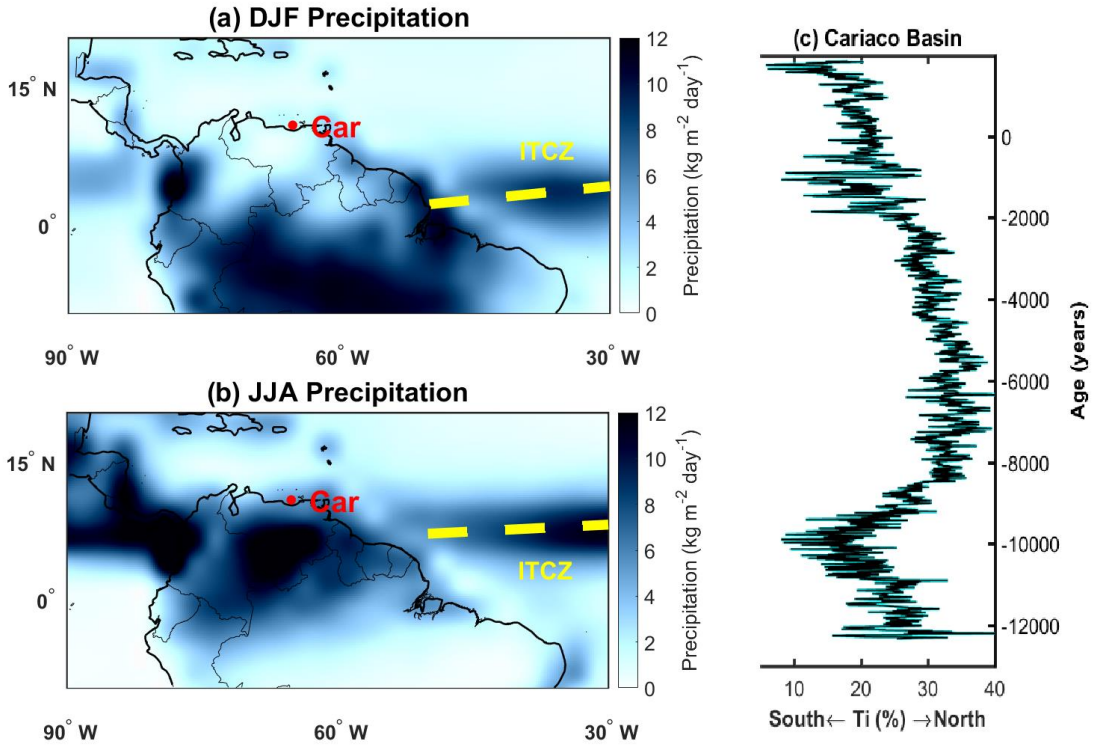

Figure 4.5 - Cariaco Basin Precipitation and %Ti sediment. *(a) Austral summer precipitation, (b) austral winter precipitation, extracted from 30 years (AD 1980 – 2010) of GPCP data. (c) Cariaco*

Basin sediment (%Ti). The location of the climate proxy is represented by the red dot indicated by the inscription Car and the summer and winter ITCZ position is indicated by the yellow strip in the maps.

An alternative to the Cariaco basin sediment is the compilation of Lechleitiner et al. (2018), which consists in a multiproxy climate reconstruction of the winter and summer global ITCZ.

4.3 – Principal Components and South America Time Series

To compare the La Plata and Cariaco basin time series to the $PC_{\delta^{18}O}$, the same procedures applied to the isotopic time series were applied to these two time series. Fig. 4.6 shows the South America time series together with the $PC_{\delta^{18}O}$ time series. The regime shift test was also evaluated for both time series, and the regime shift dates are shown in the Table 4.2. As it can be observed the regime shift dates among the time series are closer except for the onset of LIA period in the 1st $PC_{\delta^{18}O}$.

***Table 4.2 – South America Time Series Regime Shift dates**, in each cell it is represented the onset date of the climatic period. Cells which there is more than one value, represent regime shifts inside the given period.*

	MCA	TRANS	LIA	CWP
1st $PC_{\delta^{18}O}$	AD 724	AD 1160	AD 1489	AD 1878
2nd $PC_{\delta^{18}O}$	AD 906	AD 1084	AD 1362, 1639	AD 1886
NH (IPCC, 2013)	AD 950	AD 1250	AD 1450	AD 1850
GeoB138134-1	AD 989	AD 1120,	AD 1357, 1586	AD 1868
Cariaco Ti%	AD 895	AD 1053, 1276	AD 1389, 1533	AD 1798

The monsoon mode (Fig.4.6a) presents wet excursion during the LIA period, or event E1, indicated by the cyan vertical dashed line. Similar signals can be seen in the La Plata Basin (fig.4.6c) time series, with a delayed onset (LIA2 period) and synchronous demise and in the Cariaco basin sediment (fig4.6d), presenting a delayed onset and early demise (LIA2 period). Therefore, as the monsoon is the dominant variability mode, we

can take this period as the wettest period. In the fig. 4.7a and in the table 4.3, the spatial distribution of the $\delta^{18}O$ and Sr/Ca composites in unities of standard deviation is shown, with the blue colour indicating wet anomalies (^{18}O depletion) and red ones indicating dry anomalies (^{18}O enrichment). So as one can see over all the Monsoon axis or SACZ region, the long-term mean or composite analysis reveals negative $\delta^{18}O$ (blue dots) values, meaning positive precipitation anomalies over all this area. But the NEB (speleothems DV2 and PAR) presents positive anomalies meaning drier anomalies over the NEB and eastern Amazonia region. The record BOT located at the edge of the monsoon domain is the only outlier, presenting slightly drier anomalies. But, the record GeoB13813-4 presents strong positive freshwater input anomalies, consistent with its function as a proxy of La Plata basin precipitation runoff, integrating the precipitation of the southern monsoon region, especially the SACZ precipitation. Overall, our results suggest that during the LIA, the SAMS was enhanced, agreeing with previous studies (Bird et al., 2011; Vuille et al., 2012; Kanner et al., 2013 and Apaestegui et al., 2014).

In the 2nd $PC_{\delta^{18}O}$ (fig.4.7b), the wet period is the event E2, the LIA1 event, indicated by the green dashed line. The wettest period occurs when the event E1 and E2 overlaps, between CE 1439 – 1639, shown in fig.4.7b, which indicates wetter anomalies over almost all locations, except for the north and northeastern Brazil and for the La Plata basin, where the anomalies are minimal. When compared to the event E1, the high elevation Andean records, the QLC and PUM records present wetter conditions, indicating an enhancement of the humidity transport from the Amazonia to the Andes at this time (Garreaud et al., 2003; Hurley et al., 2015). The records SBE and TMO located at the south of NEB region, present slightly wet anomalies, as well as the South and Southeast of Brazil proxies, CRT and BOT, indicating an expansion of the monsoon domain toward the Northeast (NEB) and the Southeast South America (SESA).

The MCA period is more pronounced in the 2nd $PC_{\delta^{18}O}$ than in the 1st $PC_{\delta^{18}O}$ being a drier event. It is represented by the event E3 in the fig.4.6b and in the GeoB13813-4 as event E4 (fig.4.6c). The composite analysis (fig.4.7c) reveals drier anomalies over almost all the records locations, except for the eastern Amazonia, PAR record, and for the CRT1 record, located in the southeast of Brazil. The event E3 is also pronounced on the Cariaco %Ti time series as a higher Ti input into the basin, consistent with the notion

of northward migration of the ITCZ during dry periods (Bird et al. 2011; Vuille et al. 2012; Kanner et al. 2013). The La Plata basin time series presents a 'wet' pulse during this period in the event E4, possibly indicating higher activity of extratropical weather transient systems during this period, but do not propagating more equatorward.

Some authors such as Bernal et al. (2016), Novello et al. (2018) and Apastaegui et al, (2018) analysed $\delta^{18}O$ composites means during the MCA and LIA periods, but they only considered the latitudinal position of the records, like a transect around the SACZ area, suggesting a possible southward displacement of the SACZ or the monsoon axis during the LIA. However, our spatial analysis suggests an intense SACZ associated to an enhancement of the monsoon and preserving its shape throughout all the LIA period, except during the event E2, the onset of the LIA.

The monsoon enhancement of the LIA is directly linked to the southward migration of ITCZ, as seen the fig.4.6d, that strengthens the westward flux and enhances the moisture convergence in the continent leading convection over the monsoon region (Vuille et al. 2012). Another driver of the monsoon is the subtropical and tropical South Atlantic Ocean Sea Surface Temperatures (SST's), which forms a north-south dipole, where in its positive phase has the SST subtropical colder and the tropical warmer, coupling to the Subtropical High (Bombardi et al. 2014; Chaves and Nobre 2004; Jorgetti et al. 2014), and therefore, enhancing the anticyclonic circulation and the moisture influx to the continent, favouring the formation of the SACZ. In its negative phase, the Subtropical High is weakened allowing the propagation of extratropical weather systems, such as cyclones and cold fronts, which force the characteristic northwest-southeastward orientation of the monsoon circulation over the Southeast South America. The lack of high-resolution last millennia marine records sediments along the South Atlantic Ocean does not permit further assessments (see Utida et al. 2019).

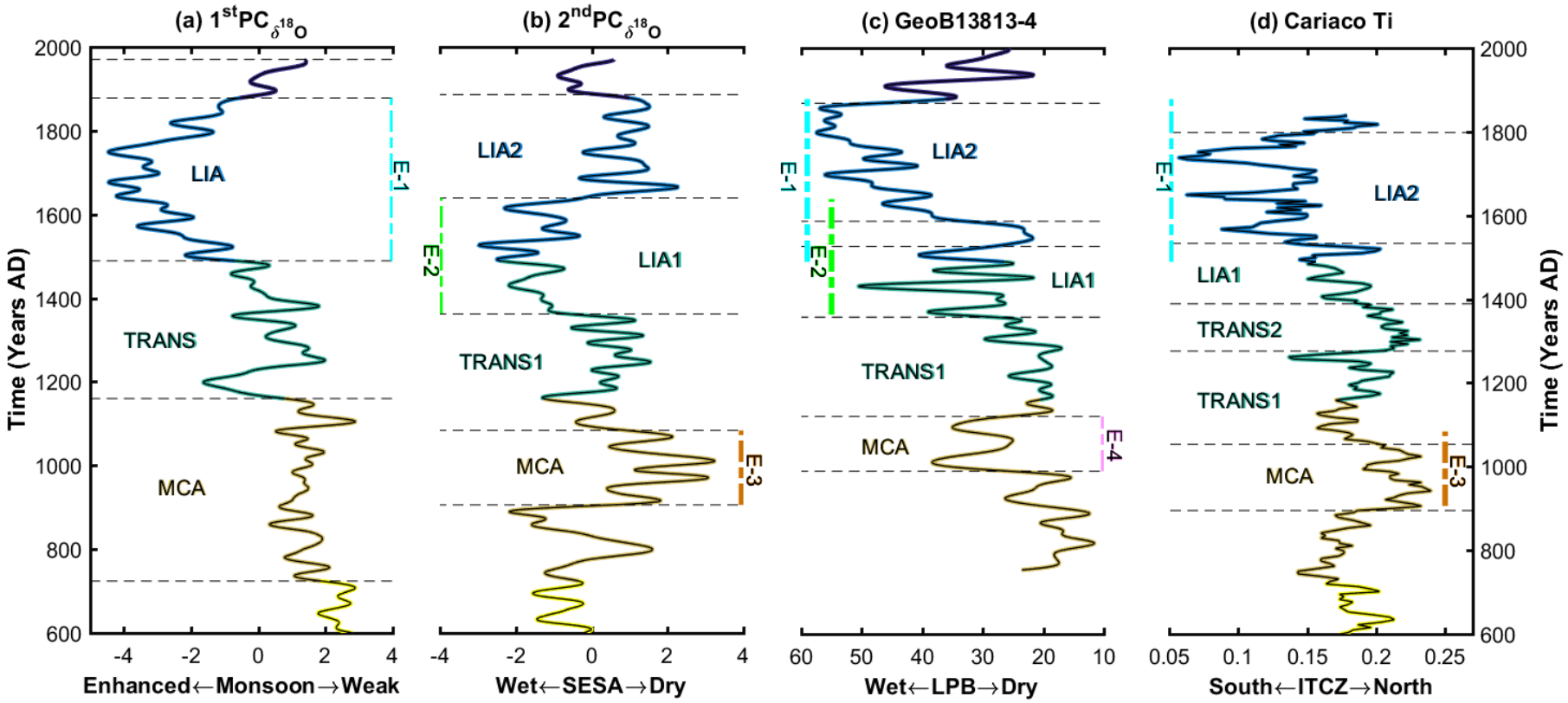

Figure 4.6 - South America Last Millennia time series. *(a) 1st $PC_{\delta^{18}O}$, (b) 2nd $PC_{\delta^{18}O}$, (c) Sediment GeoB 13813-4, (d) Cariaco %Ti sediment. The assorted colours represent different climate regimes, obtained through the regime shift test evaluated on the 1st $PC_{\delta^{18}O}$, the horizontal dotted lines represent the different climate regimes found for their respective time series. The coloured vertical dotted lines represent some important periods cited in the text.*

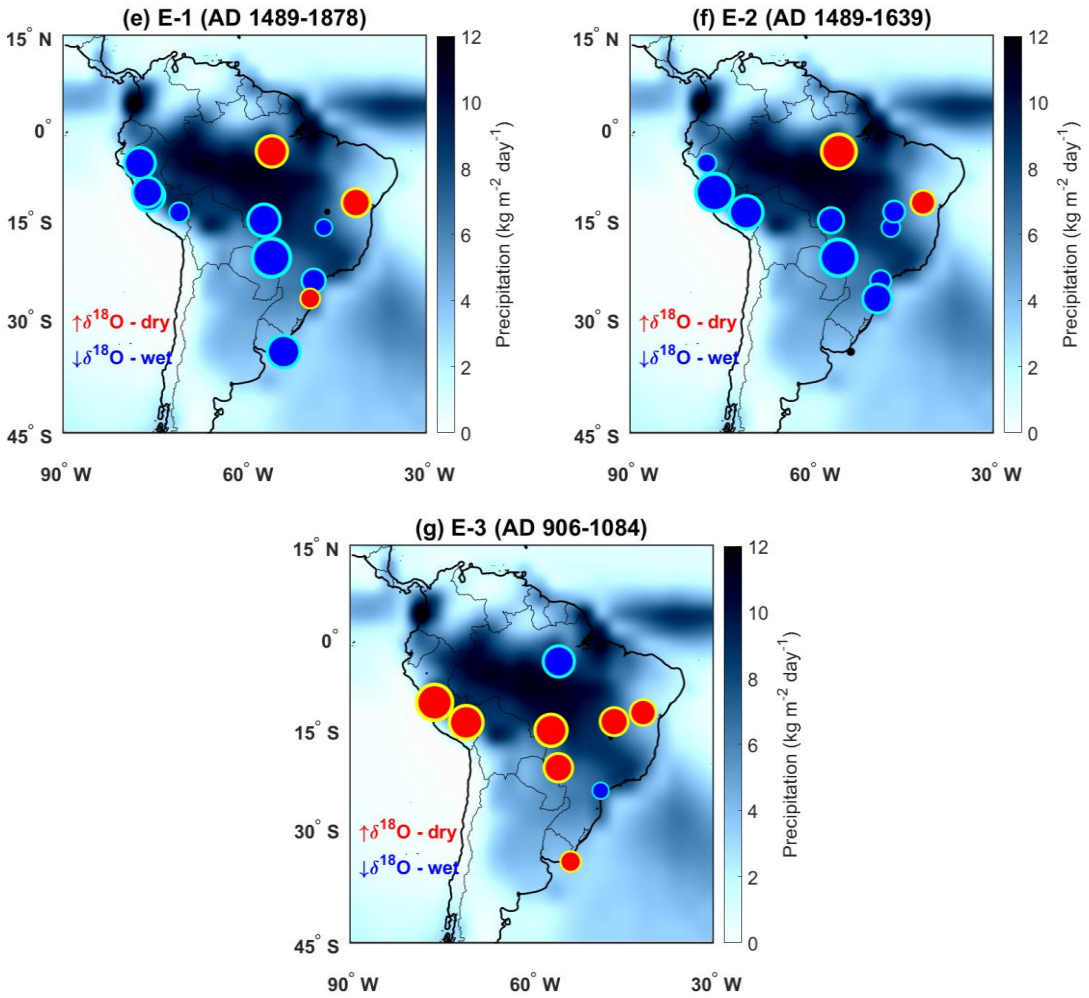

Figure 4.7 – Composite Analysis of the Last Millennia Climate Events*. (a) Event E1 or Little Ice Age, (b) Event E2 or LIA1 and (c) Event E3 or Mediaeval Climate Anomaly. Red colours indicate positive (dry) anomalies and blue colours indicate negative anomalies (blue), the size of the dots represents the intensity of the anomalies. The shaded field represent the precipitation climatology extracted from 30 years (AD 1981-2010) of GPCP analysis.*

In the current climatology, when the SACZ is active, positive precipitation anomalies dominate all the SACZ area and negative ones are found on the NEB and SESA areas (Silva and Berbery, 2006). When the SACZ is active, to compensate the upper troposphere divergence, subsidence over the SACZ adjacent area, the SESA and the NEB are observed, together with the propagation of mid-latitudes Rossby Wave trains from the Pacific Ocean (Caravlho et al., 2004; Muza et al., 2009; Ma et al.,2011). Such a pattern can be seen during the event E1, when the BOT located in the south of Brazil and DV2 located in the NEB are in anti-phase to the core monsoon records (fig.4.7a). However, during the events E2, LIA1 and MCA, this tripole pattern is not observed,

suggesting possible changes or displacements in the climatological Rossby-Wave guides at these times (Hoskins and Ambrizzi, 1993).

Spectral analysis is performed on the 1st and 2nd $PC_{\delta}{}^{18}O$, presented in the fig.4.8, shows frequencies with periodicity of 32^{-1}, 56^{-1}, 80^{-1} and 128^{-1} $years^{-1}$ with statistically significant spectral peaks. Some authors (Novello et al., 2002; Novello et al., 2016; Apastaegui et al., 2014; Bernal et al., 2016 and Perez et al. 2016) attribute centennial and multi-centennial variabilities to solar forcing, and decadal to multidecadal variabilities to some climate variability modes, like the Atlantic Multidecadal Oscillation (AMO) and the Pacific Decadal Oscillation (PDO).

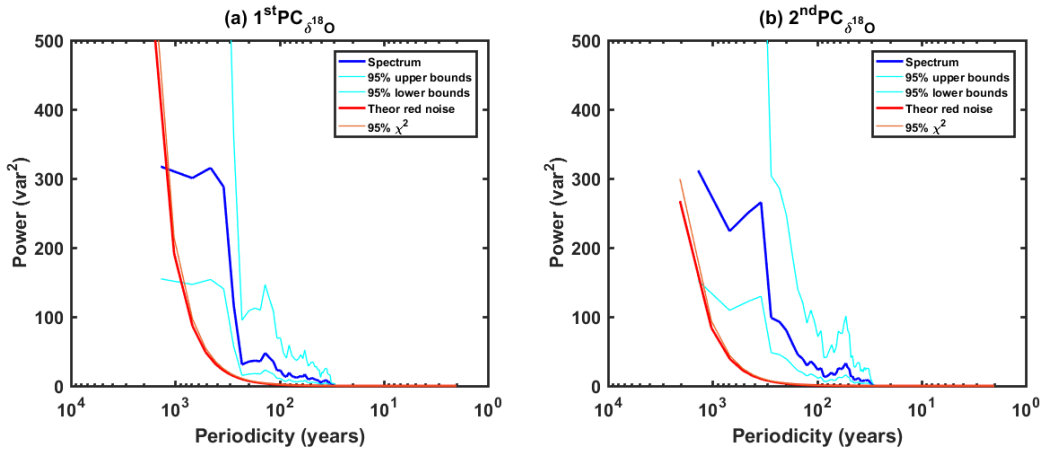

Figure 4.8 - Multitapper Power Density Estimate of $PC_{\delta}{}^{18}O$ modes, *for (a) 1st $PC_{\delta}{}^{18}O$, (b) 2nd $PC_{\delta}{}^{18}O$, only values above the red curve representing the red noise, can be considered statistically significant against the red noise at the level of 95%.*

Recent results presented by Jones and Carvalho (2018) who compared SALLJ over the SESA region to the North Atlantic SST variability, found that during negative AMO phase, there is positive precipitation anomalies over the SESA region and negative anomalies over the Amazonia and the SACZ region. This occurs due to the enhancement of the northwestern flow over the South America, combined with the outflow due to the subsidence over the core monsoon area, leading to a strengthening of the northerly winds along the east slope of the Andes and Amazon, intensifying the SALLJ, leading to positive precipitation anomalies over the SESA region. The pattern described in Jones

and Carvalho (2018) is coherent with the 2nd PC$\delta^{18}O$ spatial pattern showed in the fig.4.2b.

4.4 – Conclusion

Two isotopic based Monte-Carlo Principal Components or PC$\delta^{18}O$ is found coherent to low frequency Current Warm Period climate modes. The first represents a dipole between the monsoon domain to the Northeast of Brazil (NEB), the monsoon mode, and the second shows a tripole between the SACZ domain to the NEB and Southeastern South America (SESA), the SESA mode (fig.4.2).

Both PC$\delta^{18}O$ were compared to other two time series, a proxy of the ITCZ positioning and a proxy of the La Plata basin precipitation variability. During the LIA period, wetter conditions is found in all the monsoon domain. However, the southward SACZ displacement is not observed, contrasting to the results suggested by other publications (Novello et al., 2018; Apastaegui et al., 2016 and Bernal et al., 2016), that just presented a north-south transect along the monsoon axis, misleading to a SACZ displacement, but through our composites spatial distribution (fig.4.7), an expansion of the SACZ or monsoon axis towards the NEB and SESA is found, during the LIA1 period (CE 1489-1639).

Spectral analysis reveals significant centennial to multidecadal variabilities, and previous works attribute these variabilities to external forcings such as solar activity and to internal variability, as climate patterns forcing the atmospheric circulation, like the AMO, Solar Variability, El Niño Southern Oscillation or even the South Atlantic Oscillation (or Southern Annular Mode - SAM) to be presented in the next chapter.

Chapter V

Climate Index Proxy Time Series and South America Summer Monsoon

The climate is not only dependent on local effects, but may be affected by anomalies in remote regions, through the propagation of Rossby Waves (Hoskins and Ambrizzi, 1993; Ambrizzi and Hoskins, 1996; Van der Wiel et al. 2015) or through compensating movements (ascent/descent) due to large scale circulation, which can generate anomalies like dipoles and tripoles.

Outside the instrumental period, little is known about teleconnection patterns and just recently reliable proxy time series are available to analysis. In this chapter we compare time series of well-known climate modes of variability acting over the South America, the Southern Annular Mode (Abram et al., 2014), the ENSO variability mode (Li et al., 2011), the Atlantic Multidecadal Oscillation Mode (Wang et al., 2017) and a Northern Hemisphere temperature reconstruction (Moberg et al., 2005).

At first, a summary presenting the description of the climate modes time series will be presented. Then, a brief discussion presenting the Wavelet Coherence and Empirical Mode Decomposition analysis performed over the proxy time series and some partial conclusions of the analysis will close the chapter.

5.1 – Climate Index Proxy

5.1.1 – Southern Annular Mode Reconstruction

The Southern Annular Mode (SAM) is the main mode of climate variability of the Southern Hemisphere, acting in displacing the storm tracks north to south, leading to temperature and precipitation anomalies over the South America, especially in the Southern South America (Silvestri & Vera, 2003; Gillet et al., 2006; Villalba et al., 2012). The SAM can be defined as the difference of the mean atmospheric pressure between middle latitudes and the Antarctica or the 1st leading principal component of the 850hPa mean atmospheric pressure or the 500hPa geopotential height along the Southern Hemisphere (Rogers and Van Loon, 1982).

In its positive phase the SAM is associated to low pressure anomalies over the Antarctic continent and high-pressure anomalies over middle-high latitudes (40°S) and in its negative phase, the opposite. During their negative phase it is expected a northward displacement of the storm tracks and an increase in the cyclonic and frontogenetical activity over the La Plata basin and Southern of Brazil region (Carvalho et al., 2005; Vera et al., 2006; Reboita et al., 2009).

In a palaeoclimatological context, Abram et al. (2014) provided an annual time series of the SAM index, which was the result of a multi-proxy compilation of records along the Antarctic continent. Comparisons between CMIP5/PMIP4 ensembles and observations shows the reliability of this reconstruction. In their work, Abram et al. (2014) presented the raw time series and the 80 years low passed filtered time series. Here we use the raw annual time series obtained from their compilation.

5.1.2 – Atlantic Multidecadal Oscillation

In the past 150 years the North Atlantic Ocean SST exhibits multidecadal variability (60 – 80 years) affecting the climate on the adjacent continents and this SST

behaviour is commonly called of Atlantic Multidecadal Oscillation (AMO) (Enfield et al., 2001; Wang et al., 2017).

The impacts of the AMO extends from the North Atlantic to the Sahel region, Indian Ocean (Zhang & Delmont., 2006), the Northeast Brazil (Knigtht et al., 2006; Novello et al., 2014; Kayano et al., 2016) and the SESA region (Jones & Carvalho, 2018). The AMO in its cold phase impacts the Northern of Amazonia and ITCZ region with negative precipitation anomalies and it may also be associated with strong episodes of SALLJ, leading to positive precipitation anomalies over the SESA region (see chapter IV for further discussions).

The AMO reconstruction time series is the result of a compilation of 46 annually terrestrial climate proxies along the North Atlantic coast (e.g. North America, Europe and North Africa), most of the proxies based on tree rings extending 1200 years before present. Wang et al. (2017), obtained the Atlantic Multidecadal Variability/Oscillation, through multivariate principal component regression.

5.1.3 – Northern Hemisphere Temperature Reconstruction

Moberg et al. (2005) reconstructed the Northern Hemisphere temperature through the combination of various terrestrial and SST oceanic temperature climate proxy around the Northern Hemisphere, combining low resolution proxies, like boreholes, to high resolution proxies, like tree ring thickness and ice cores, using wavelet transform and variance scaling to retrieve a high frequency Northern Hemisphere time series.

Alternatively, there is the NH temperature reconstruction of Mann and Jones (2003), that besides using most of the proxies used by Moberg et al. (2005), due to the greater geographical sparseness of the proxy data and the lack of the variance scaling, they do not show results as robust as Moberg et al. (2005). So, for the next analysis, just the Moberg et al. (2005) NH reconstruction time series is considered in this work.

5.1.4 – El Niño Southern Oscillation

The North America west coast, particularly, is a region prone to the influence of El Niño, which in its warm phase induces positive temperature and precipitation anomalies along a dry area. Considering a set of 4 thousand tree rings over the U.S. west coast, precipitation proxy data spanning to the last millennium were used to construct the North America Drought Atlas (NADA, Cook et al., 2004).

Li et al. (2011) evaluating the Principal Component Analysis over the NADA dataset found the 1st leading Empirical Orthogonal Function coherent to the El Niño imprinting over the west of U.S, representing 23.5% of the total variance of the data. However, the 1st NADA principal component presents a strong white noise and larger Niño/Niña amplitudes than observed in the instrumental period. So, in order to 'filter' and reduce the bias due to outliers, Li et al. (2011) computed the 21 years variance measuring changes in the ENSO amplitude. Thus, the ENSO variance time series is used in this work.

5.2 – Time Series Analysis

In Fig. 5.1 the climate proxy time series, as well as the South America time series are shown, and comparisons between the $PC_{\delta^{18}O}$ to the South America time series (Fig.5.1a-d) was provided in the previous chapter. The same regime shift test (Lavielle, 2005) applied in previous analysis were evaluated here for the climate index time series (Fig.5.1e-h) and they are shown by the dashed horizontal lines in the figure.

Northern Hemisphere Temperature

Comparing the NH temperature (Moberg et al., 2005; fig.5h) to the 1st $PC_{\delta^{18}O}$, the same "secular trend" is observed between the time series, showing similar variabilities during both the LIA and TRANS periods, suggesting that the 1st $PC_{\delta^{18}O}$ or monsoon

variability mode are linked to the Northern Hemisphere (NH) temperature variability. Previous studies like Novello et al. (2016), that compared the NH temperature to mid-western Brazil speleothems, found similar results for the LIA and MCA periods.

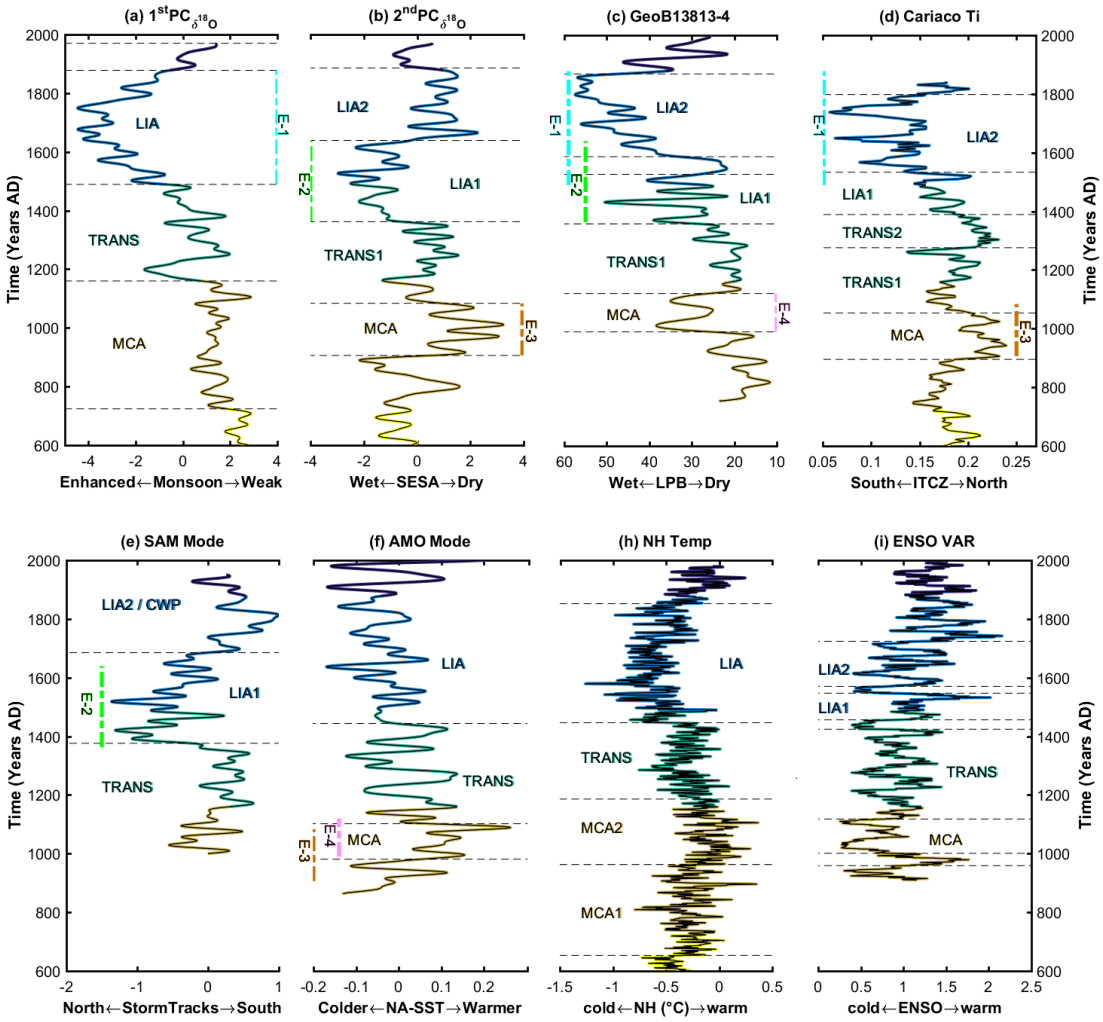

Figure 5.1 - South America and Climate Index time series. *(a) 1st PC$_{\delta^{18}O}$, (b) 2nd PC$_{\delta^{18}O}$, (c) GeoB13813-4, (d) Cariaco %Ti, (e) Southern Annular Mode reconstruction, (f) Atlantic Multidecadal Oscillation Mode reconstruction, (g) Northern Hemisphere Temperature reconstruction and (h) El Niño Southern Oscillation variance reconstruction. The assorted colours represent periods found through the regime shift test and the dashed lines represent shift periods of their respective time series.*

It is well known that changes in the incoming solar irradiance and volcanic eruptions leads to changes in the Northern Hemisphere (NH) temperature as those which led to the LIA onset (Miller et al., 2012). The NH temperatures indirectly

influenced the SASM due to its function in the inter-hemispheric energy exchange (Schneider et al., 2014) leading to the ITCZ displacement, which in seasonal to longer time scales migrates towards the warm hemisphere (Schneider et al., 2014), impacting the moisture supply over the SAMS.

As discussed previously and comparing the %Ti Cariaco time series (fig.5.1d) to the 1st $PC_{\delta^{18}O}$ and NH temperature (figs.5.1a, h respectively), the same secular trend can be seen, and more pronounced for the %Ti Cariaco time series, during the MCA period.

Southern Annular Mode

In longer time scales, similar features can be observed between the 2nd $PC_{\delta^{18}O}$ (Fig.5.1b) and the Southern Annular Mode (Abram et al., 2014) time series (Fig.5.1e). Considering just the overlapping period between the time series, one can see a shift in the SAM signal during the LIA1 period (AD 1400 - 1650) toward negative values or phase, meaning a northward shift of the storm tracks, accompanying a shift towards wetter conditions or widening of the SACZ (see Fig.4.7b) during its onset in the LIA (event E2 in the 2nd $PC_{\delta^{18}O}$) period. The 2nd $PC_{\delta^{18}O}$ as shown in the Fig.4.2b, weights (higher loading coefficient values) towards the edges of the SAMS, especially the BOT (Botuverá) speleothem located over the Santa Catarina state in the Southern of Brazil.

In the current climatology (AD 1981-2010), during negative SAM phases (Silvestri & Vera 2003; Carvalho et al., 2005 and Vera et al., 2006) many studies observed positive precipitation anomalies over the SESA, Southern of La Plata Basin and Uruguay, in particular, Silvestri and Vera (2003) associated these precipitation anomalies to an intensification of an upper level cyclonic anomaly over the ocean, enhancing the humidity convergence over the SESA region, during the spring and the winter. Reboita et al. (2009), shows that during negative SAM phases there is a northward shift of the cyclones tracks and an increase in the cold-fronts frequency over the SESA, associated to the northward shift of the storm tracks, however during the summer season these anomalies are weak.

The spatial pattern found for the 2nd $PC_{\delta}{}^{18}O$ (Fig.4.2b) is coherent to the SAM activity over the southern edge of the SASM. Nevertheless, some studies like Datwyler et al. (2017), who studied the SAM variability in the last millennium, suggest that the SAM teleconnections are not stationary and no time-coherent along the Southern Hemisphere in the Last Millennium, highlighting the importance of local climate dynamics and thermodynamics in generating the precipitation and temperature anomalies over the continent and other teleconnection patterns, like the Pacific South America pattern (PSA, Mo & Higgins, 1997) and the dipole SACZ-SALLJ (Liebmann et al., 2004), as well as the South Atlantic Ocean SST variability (Bombardi et al., 2014; Jorgetti et al., 2014) in driving precipitation and temperature anomalies across the South America.

Wavelet Coherence (Torrence & Compo., 1998; Grinsted et al., 2004) and Empirical Mode Decomposition (Huang et al., 1998) were performed over both the 2nd $PC_{\delta}{}^{18}O$ and SAM reconstruction time series. Wavelet Coherence does not show any coupled signal between the time series. However, the Empirical Mode Decomposition, reveals couplings between the SAM and the 2nd $PC_{\delta}{}^{18}O$. The full Empirical Mode Decomposition and Wavelet Coherence is presented in the appendix section.

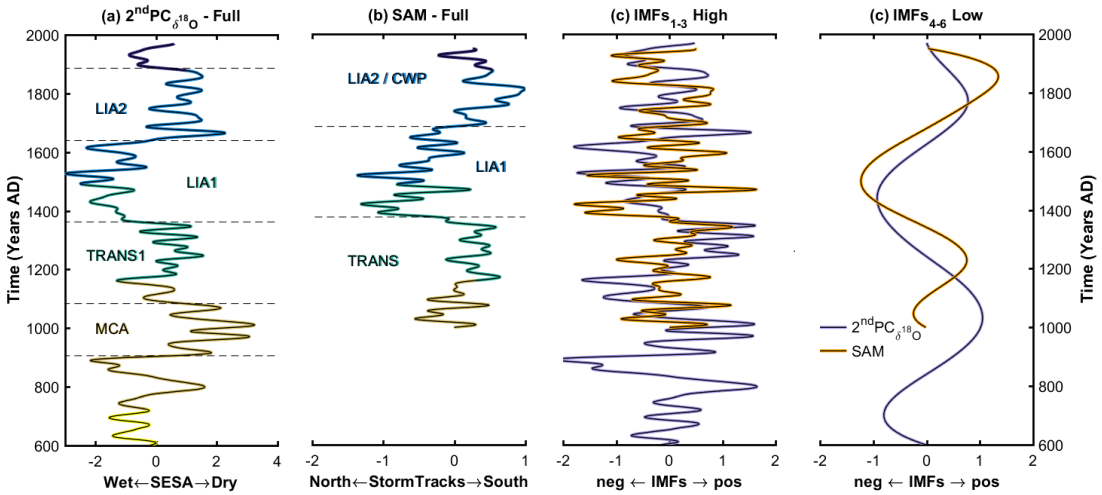

Figure 5.2 - Empirical Mode Decomposition Analysis between the 2nd $PC_{\delta}{}^{18}O$ and the SAM mode. *(a) 2nd $PC_{\delta}{}^{18}O$, (b) SAM mode as in the Fig.5.1. (c) 2nd $PC_{\delta}{}^{18}O$ and SAM modes reconstructed with the first 3 IMFs and (d) reconstructed with the last 3 IMFs. The blue curve represents the 2nd*

$PC_{\delta^{18}O}$ and the orange one, the SAM mode. A figure showing all the IMFs separately is provided in the appendix section.

Excluding the trend component, both the 2nd $PC_{\delta^{18}O}$ and SAM signals were decomposed into 6 Intrinsic Mode Functions (IMFs), where the first 3 IMFs are called high frequency component and the last 3 called of low frequency component. In fig.5.2 the low frequency and the high frequency component of the 2nd $PC_{\delta^{18}O}$ and SAM mode time series are presented.

The high frequency IMFs reconstruction representing multidecadal to centennial variabilities (frequency band from 32^{-1} years^{-1} to 128^{-1} years^{-1}) are shown in Fig.5.2c. As one can see, most of the time series peaks are in phase from the LIA1 period to the transitional period (AD 1200 - 1600), except during a short time slice in the onset of the LIA1 period. This result suggests that the SAM may have influenced the SESA precipitation behaviour during the LIA and Transitional periods.

The low frequency IMFs, representing centennial variabilities (frequencies < 128^{-1} years^{-1}) are shown in Fig.5.2d. It is observed that both time series present pronounced secular trends with around 100 years lag, with the 2nd $PC_{\delta^{18}O}$ leading the SAM at these frequencies band. Previous studies over South America (Novello et al., 2012) attributed these variabilities to external forcings (Saltzman, 2001), as solar activity, probably influencing both time series and the climate over the whole Southern Hemisphere.

Atlantic Multidecadal Oscillation/Variability

As done for the SAM time series, wavelet coherence was performed over the 1st$PC_{\delta^{18}O}$ and the AMO index, shown in Fig.5.3a, The coherence analysis reveals statistically significant coupling from AD 900 to AD 1300, a period spanning the from the MCA to the early TRANS period, at the band centred about 200^{-1} years^{-1}. Empirical Mode Decomposition was also evaluated as done in the previous section and it is presented in the Fig.5.3. b-e. As one can see, only the low frequency component of the signal presents some coupling between the time series, agreeing well to the wavelet coherence analysis.

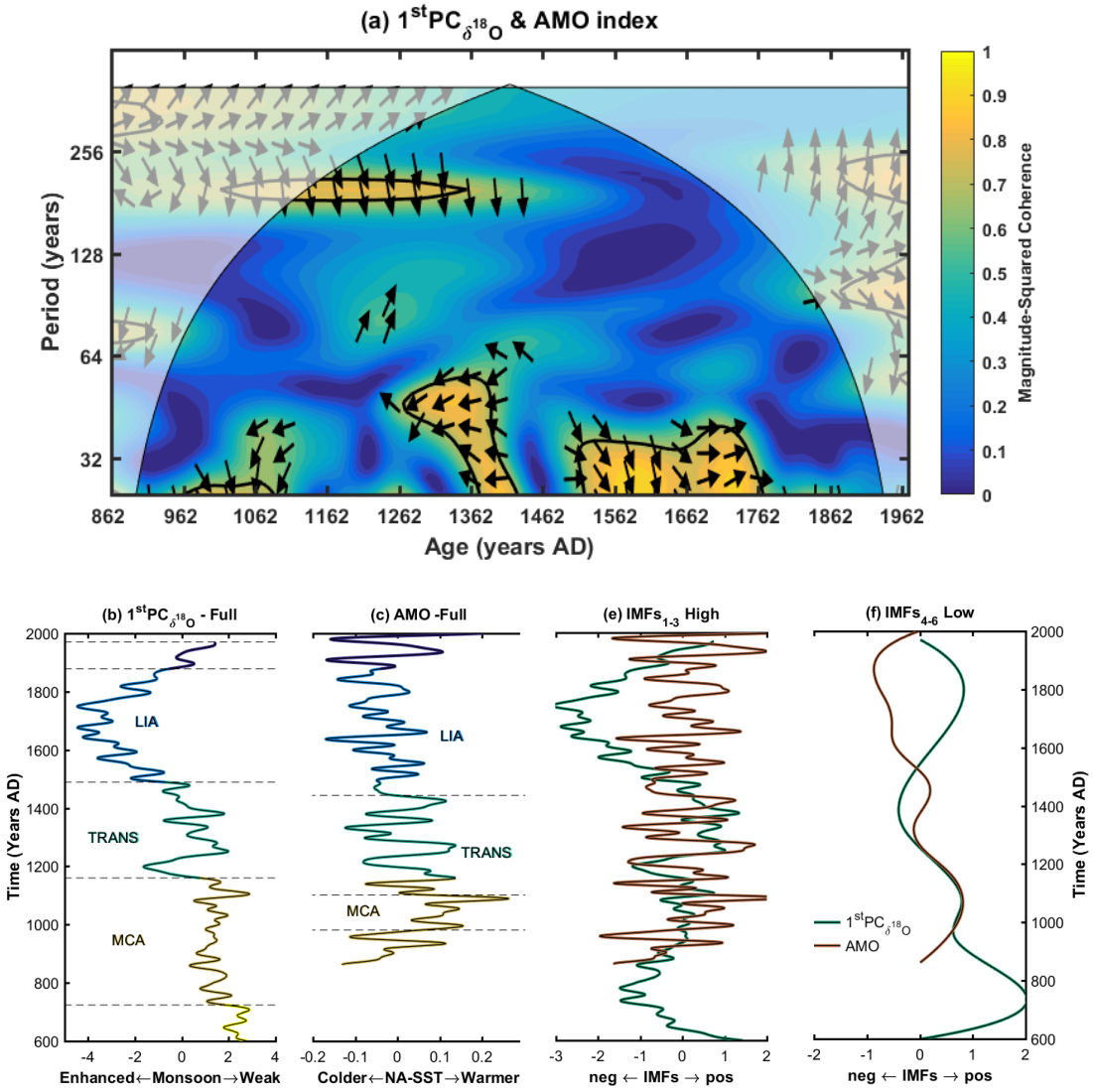

Figure 5.3 – Spectral analysis and Empirical Mode Decomposition between the 1st $PC_{\delta}{}^{18}{}_{O}$ and the AMO time series*. (a) Wavelet Coherence Analysis, between the 1st $PC_{\delta}{}^{18}{}_{O}$ and AMO index, statistically significant values at the level of 95% are presented inside the contours, and the arrows indicate the phase angle between the signals. (b) 1st $PC_{\delta}{}^{18}{}_{O}$, (c) AMO time series, (d) High frequency IMFs reconstruction and (e) Low frequency IMFs reconstruction. The green curves represent the 1st $PC_{\delta}{}^{18}{}_{O}$ reconstruction and the brown curve is referent to the AMO reconstruction.*

Most of the South American studies attribute the influence of the AMO to multidecadal climate variabilities around 64^{-1} $years^{-1}$ (Chiessi et al., 2009; Apastaegui et al., 2014; Novello et al., 2014). However, Apastaegui et al. (2014) compare their proxy time series (#1 – PAL see table3.1) to the AMO reconstruction of Mann et al. (2005),

which substantially differs from the modern AMO reconstruction (Wang et al., 2017) used in this work. So, our results suggest a possible influence of the AMO in the SASM behaviour in multicentennial time scales during the last millennium.

In the Chapter IV, it was discussed possible links between the AMO and the 2nd $PC_{\delta^{18}O}$, based in the likelihood between the results obtained by Jones and Carvalho (2018) to our spatial pattern (Fig.4.2b). The events E3 and E4 found for the 2nd $PC_{\delta^{18}O}$ and for the sediment GeoB13813-4, representing the La Plata Basin precipitation, show a clear signature for the MCA period, one presenting drier anomaly over the SESA and other presenting wetter anomalies (when comparing the periods before and after) respectively. As indicated in the fig.5.1g, the events E-3 and E-4 are associated to a positive AMO/AMV index.

Jones and Carvalho (2018) found that negative AMO phases are associated to positive precipitation anomalies over the SESA domain, agreeing with our analysis, which present drier anomalies during the event E-3. However, the GeoB13813-4 La Plata basin precipitation presents a wetter excursion, as the SESA and SACZ domains are located over the mid-to-northern portion of the La Plata basin. This result suggest that this "wetter" excursion or event E-4 can be due to a southward displacement of the storm tracks or extremely southward displacement of the SALLJ, leading to precipitation anomalies over the southern portion of the basin, possibly not associated to the SAM mode in centennial to multicentennial time scales that at this time presents in its neutral phase.

El Niño Southern Oscillation

Wavelet Coherence and Empirical Mode Decomposition were evaluated over the ENSO variance time series to the 1st $PC_{\delta^{18}O}$ and 2nd $PC_{\delta^{18}O}$. It was not found any coherence or coupled variability periods between the time series. However, during the events E-3 and E-4 the ENSO time series presents low variance than to the other periods, suggesting a possible signature of the ENSO negative phase (e.g. La Niña) on the 2nd $PC_{\delta^{18}O}$ which presents drier conditions at this time, coherent to La Niña episodes

signature over this area. On the other hand, the GeoB13813-4 presents wetter conditions at this time, not coherent to the La Niña signature over the LPB region, but coherent to the AMO signature as discussed previously, suggesting a predominance of the AMO signal over the ENSO in multidecadal time scales. High-resolution proxies along the Pacific Ocean and over the South America ENSO teleconnections areas are needed to further discussion.

5.3 – Conclusions

Wavelet Coherence and Empirical Mode Decomposition were applied to compare the two $PC_{\delta^{18}O}$, La Plata and Cariaco basin time series, described in the Chapter IV and III, to the AMO, SAM, NH temperature and ENSO variance time series.

The NH temperature shares a common behaviour to the monsoon proxies, the 1st $PC_{\delta^{18}O}$ and the GeoB13813-4, presenting colder condition during the LIA (enhanced monsoon) and warm conditions during the MCA period. This common behaviour is probably associated to the ITCZ southward/northward shifts that occurred during the LIA/MCA, as it is observed by comparing these time series to the %Ti Cariaco basin sediment time series, which also shares a common behaviour, presenting southward/northward displacement during the LIA/MCA, evidencing the dependency of the ITCZ shift in the SASM variability.

The 2nd $PC_{\delta^{18}O}$ seems to be influenced by the SAM mode during the LIA1 period (CE 1362 - 1669), presenting wetter conditions over the SESA region associated to a possible northward displacement of the storm tracks, which is coherent to a negative SAM phase. In higher frequencies the IMFs suggest possible coupled behaviour between the proxy time series during the LIA1 and the TRANS period.

Regime shift test applied to the 2nd $PC_{\delta^{18}O}$, GeoB13813-8 data and to the AMO reconstruction, reveals possible influences of the AMO over the SESA and over the southern La Plata basin precipitation anomaly, where both time series present opposite signals, indicating a possible southward displacement of the SALLJ or the storm tracks,

but it was found some association with the SAM mode in multidecadal frequencies and during the LIA and TRANS period.

Interferences between atmospheric variability modes and teleconnections, even in the CWP or industrial period are subject of research and the decadal to multidecadal variability of this mode are still not well known. Earth system modelling efforts are necessary to clarify the role of these teleconnection patterns on the South America during the last millennium.

Chapter VI

Conclusions

A set of 12 paleo-precipitation proxies covering the last 1000 years are compiled by mean of Monte Carlo Principal Component Analysis accounting the records' dating uncertainty, generating a set of 12 latent variables. From the compilation just 2 latent variables are found physically meaningful, and statistically significant based on the Principal Component loading coefficient dispersion and in their eigenvalues' magnitude.

The leading Principal Component, representing 31 ± 2 % of the data variability, is found coherent to the current monsoon variability pattern extracted from 100 years of CERA20C reanalysis precipitation data. The second leading Principal Component representing 13 ± 1 % of the data variability, is found coherent to the current Southeast South America – South Atlantic Convergence Zone – Northeast of Brazil pattern or simply SESA pattern. One representing the strength of the South American Monsoon precipitation and the other representing its format.

Regime shift test based on the mean was evaluated over the Principal Components, revealing four anomalous period, the Medieval Climate Anomaly (CE 724 1160), the Transitional Period (CE 116 – 1489), the Little Ice Age (CE 1489 - 1878) and the Current Warm Period (CE 1878 - today). In the Little Ice Age was found the wettest period presenting stronger monsoon and in the Medieval Climate Anomaly occurred the driest period, indicating a weaker monsoon. These results agree well to previous studies found in the literature (Novello et al. 2018; Novello et al. 2016; Apáestegui et al. 2016; Vuille et al. 2012 and table 3.1 references).

Composite analysis based on the regime shift test evaluated over the proxy based Principal Components and over others South America time series representing the La Plata Basin precipitation and the interannual Intertropical Convergence Zone activity, show generalized drought during the Medieval Climate Anomaly period, except for the eastern of Amazonia region. The onset of the LIA is marked by a widening of the Monsoon (Monsoon axis or SACZ), rather than a southward displacement in contrast to previous interpretations from Novello et al. (2018), Apaéstegui et al. (2018) and Bernal et al. (2016), and the middle to the demise of the Little Ice Age, presents a contraction of the Monsoon to its current (e.g. Industrial Period, after CE 1850) climatological position, but more intense as revealed by the La Plata basin sediment.

The fig.6.1 summarizes the results found for the paleo-precipitation records compilation and for the composite analysis through the scatter plot of the 1st to the 2nd Monte-Carlo Principal Component based on the proxy data (see appendix for details about the figure).

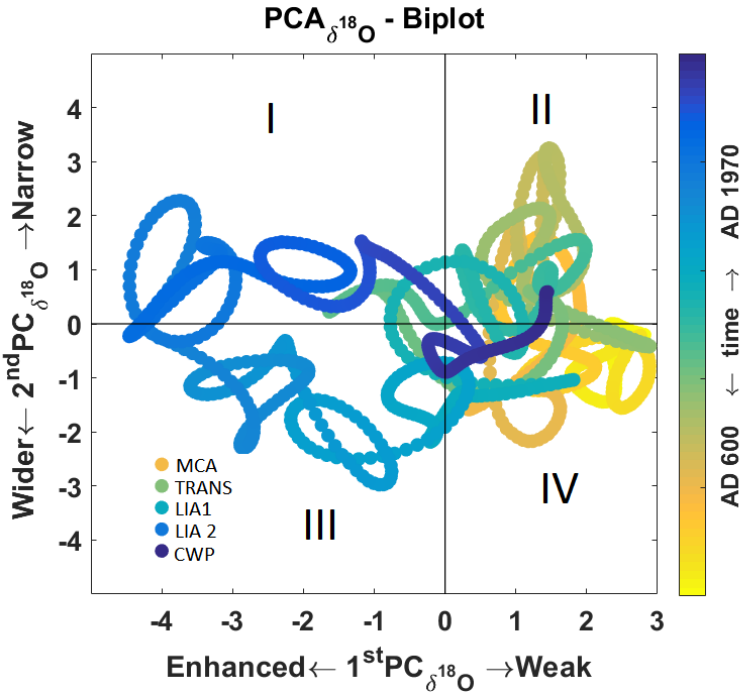

Figure. 6.1 – Biplot or scatter plot of the leading two Monte-Carlo Principal Component Analysis based on the proxy data. *The x axis represents the monsoon activity mode and the y axis represent the tripole SESA-SACZ-NEB mode or simply the SESA mode. The roman algorisms represent the quadrants of the biplot. The periods studied are represented by the assorted colours as showed in the legend on the left side inside the figure.*

Spectral and Morlet Wavelet analysis were applied over the time series, presenting multidecadal and multicentennial statically significant periodicities centred at the bands of 32, 80, 128 and 200 years. These variabilities are generally attributed to some climate variability modes, such as to the Atlantic Multidecadal Oscillation and to the Solar variability. Wavelet Coherence and Empirical Mode Decomposition was performed over the Atlantic Multidecadal Oscillation, Southern Annular Mode, Northern Hemisphere temperature and El Niño Southern Oscillation last millennium reconstructions.

The Northern Hemisphere and the Intertropical Convergence Zone reconstruction shares a common signal to the 1st $PC_{\delta^{18}O}$, throughout the analysis period (CE 650 - 1970), representing the monsoon strength, evidencing the dependency of the Intertropical Convergence Zone displacement in the moisture supply of the monsoon.

Through the decomposition of the 2nd $PC_{\delta^{18}O}$ and the Southern Annular Mode signals (EMD and Wavelets). Significant results is found for the lower and higher frequency components. For the lower frequencies (centennial), it is suggested that the Southern Annular mode possibly influenced the precipitation over the Southeast South America domain during the first half of the Little Ice Age period through the northward displacement of the storm tracks. In higher frequencies (decadal to multidecadal) coupled behaviour between the two modes are observed from the Transitional to the middle of Little Ice Age period (CE 1084 - 1639).

Wavelet Coherence and Empirical Mode Decomposition between the monsoon and the AMO modes reveals coupled low frequency (periodicity of 200 years) behaviour during CE 1000 – 1200 suggesting possible influences of the AMO on the Monsoon strength during the late Medieval Climate Anomaly to the early Transitional period. Regime shift test applied on the AMO time series suggests possible influences of this mode during the Medieval Climate Anomaly for the precipitation over the Brazilian Northeast and Southeast South America and southern of La Plata basin regions, which are coherent to previous studies found in the literature (see table 2.1 and table 3.1 references) and to recent publications related to the climate in the Industrial Period such

as Jones and Carvalho (2018), that found precipitation patterns similar to the 2nd proxy based Principal Component.

Paleoclimate studies exploring the climate low frequency variability dynamics is still very scarce over South America, efforts to sample paleoclimate records off the South America Monsoon region and at the edges of the system, is crucial to assess their spatial variability and strength during the last millennia and other periods.

Works such as Bombardi et al. (2014), Jorgetti et al. (2014), shows the role of the South Atlantic Ocean in modulating the precipitation over the continent, there is an urgent need of last millennium paleoclimate proxy over the South Atlantic Ocean in order to study the monsoon drivers.

The paleoclimate multiproxy compilation and the division of the South America precipitation into two modes of climate variability, the monsoon and the tripole Southeast South America – South Atlantic Convergence Zone – Northeastern of Brazil, represents a novel approach in the paleoclimate field of study. This novel approach allows robustly, one to compare earth system model outputs, like those of the PMIP/CMIP (Paleoclimate Model Intercomparison/Coupled Model Intercomparison) framework (Jungclauss et al. 2017) to paleoclimate proxies through the modes of climatic variability (Benestad et al., 2019) as a future work.

Appendix

A.1 – Large Scale South America Monsoon Index (LISAM, da Silva et al. 2007)

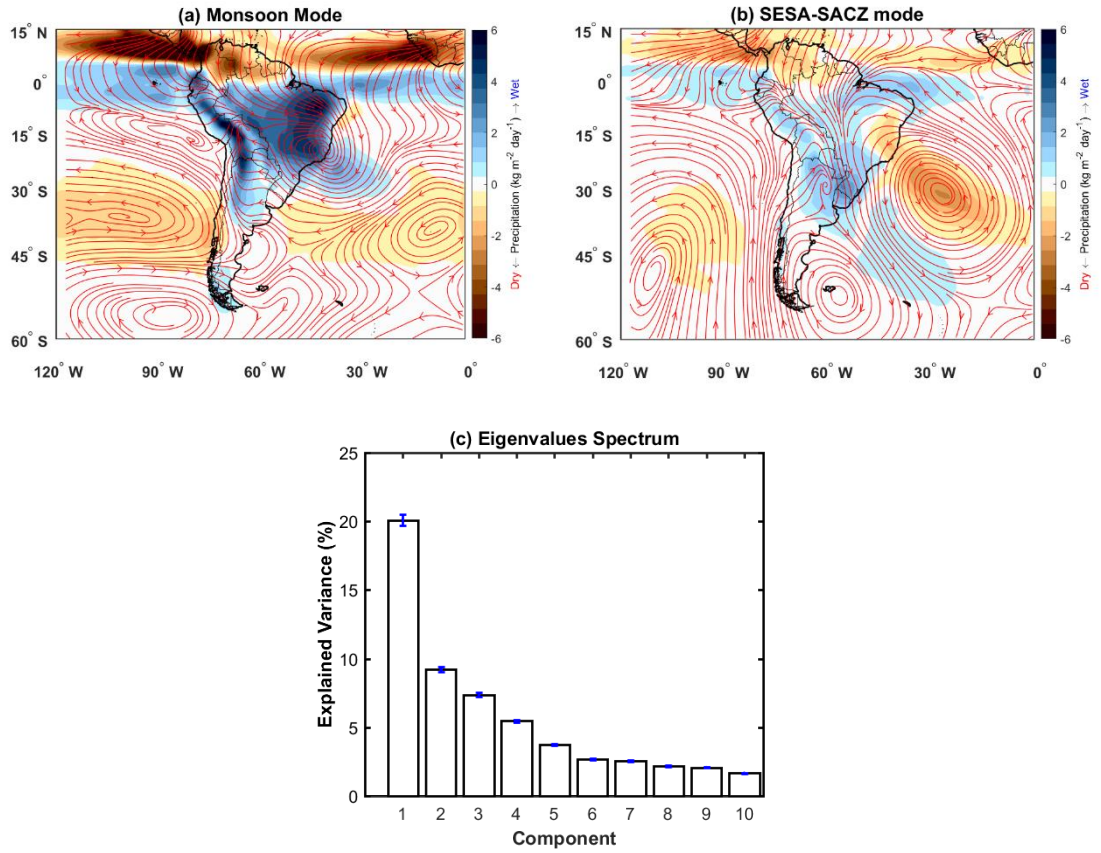

Figure A.23 – LISAM, Large Scale South America Monson Index. *(a) 1st LISAM mode, representing the monsoon precipitation, (b) 2nd LISAM mode, representing the SACZ-SESA precipitation pattern and (c) Explained Variance or Loadings latent values. The LISAM consists of the Principal Component of the low-level circulation, temperature, specific humidity and surface precipitation. Here the annual mean was taken through a 13-year running mean filter. da Silva et al. (2007) removed the annual component using just a linear trend.*

A.2 – Principal Component Analysis of the TCRW data

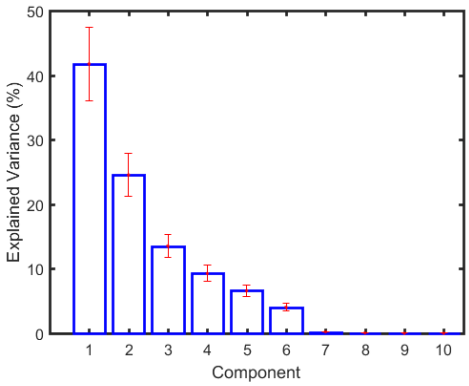

***Figure A.24 - Explained Variance for the TCRW principal component analysis**, the error bars were computed through the North et al. (1982) rule of thumb.*

A.3 – Wavelet Analysis and Coherency Analysis

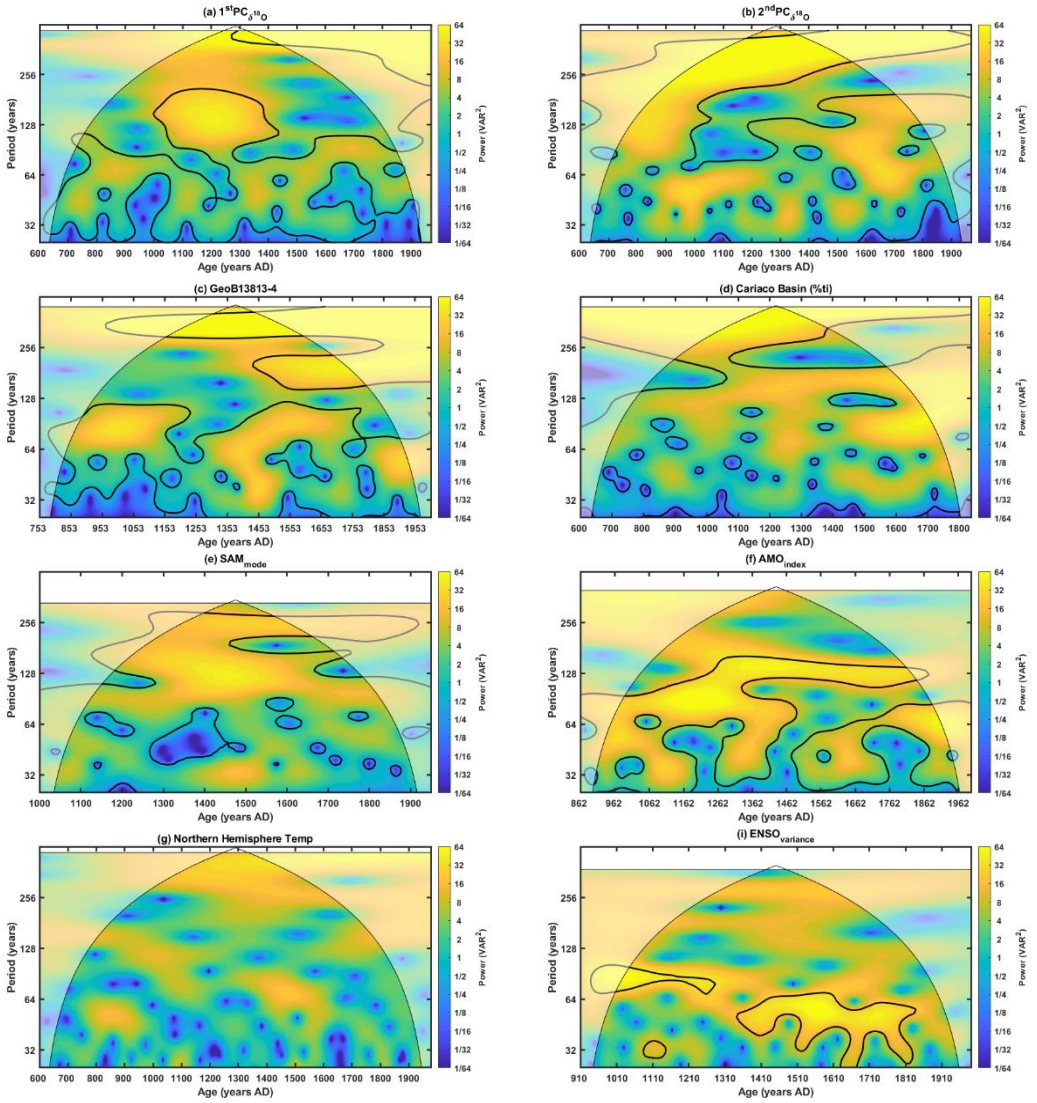

Figure. A.3 – Morlet Wavelet Analysis*, the shaded inside the contour represent statistically significant values at the level of 95%. The light shaded represent the Cone of Influence. (a) 1st PC, (b) 2nd PC, (c) GeoB13814 sediment, (d)Cariaco Basin, (e) SAM, (f) NH temperatures and (g) ENSO variance*

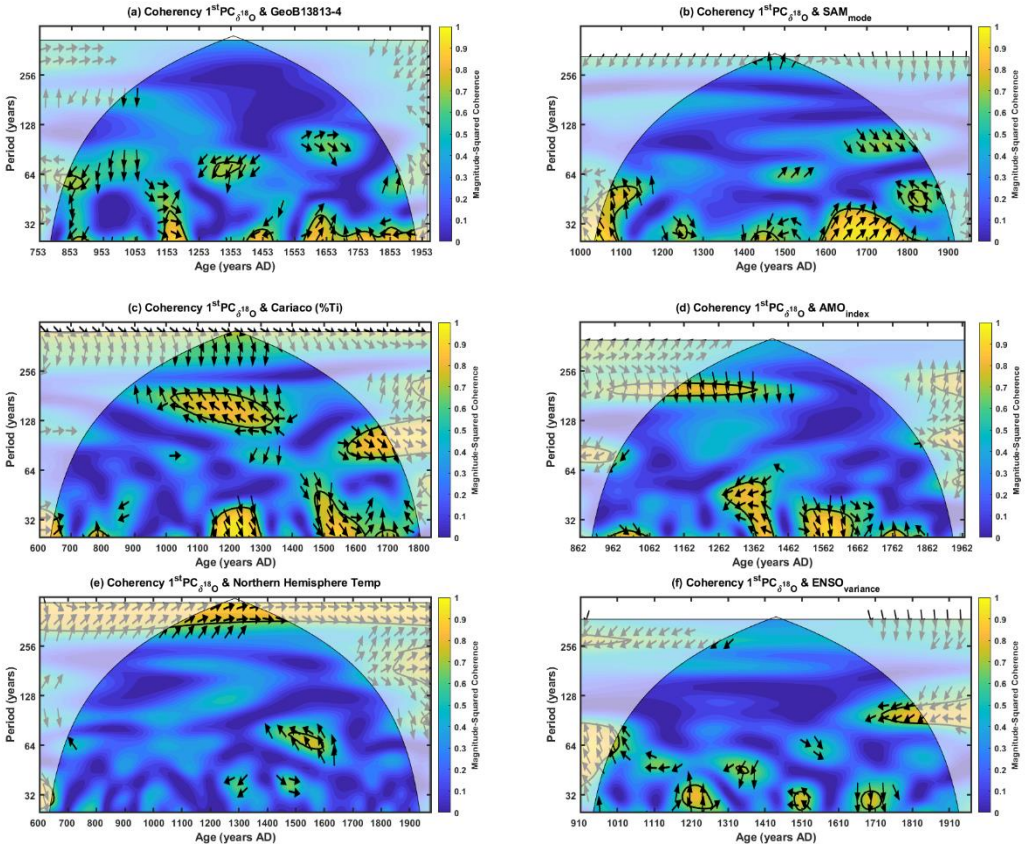

Figure A.4 -Wavelet Coherency Analysis*, values inside the black contours, represent statistically significant values at the level of 95%, the arrows represent the leads and lags between the time series. Coherency between the 1stPC and (a) GeoB13413, (b) SAM, (c) Cariaco Basin, (d) AMO index, (e) Northern Hemisphere Temperature and (f) ENSO variance.*

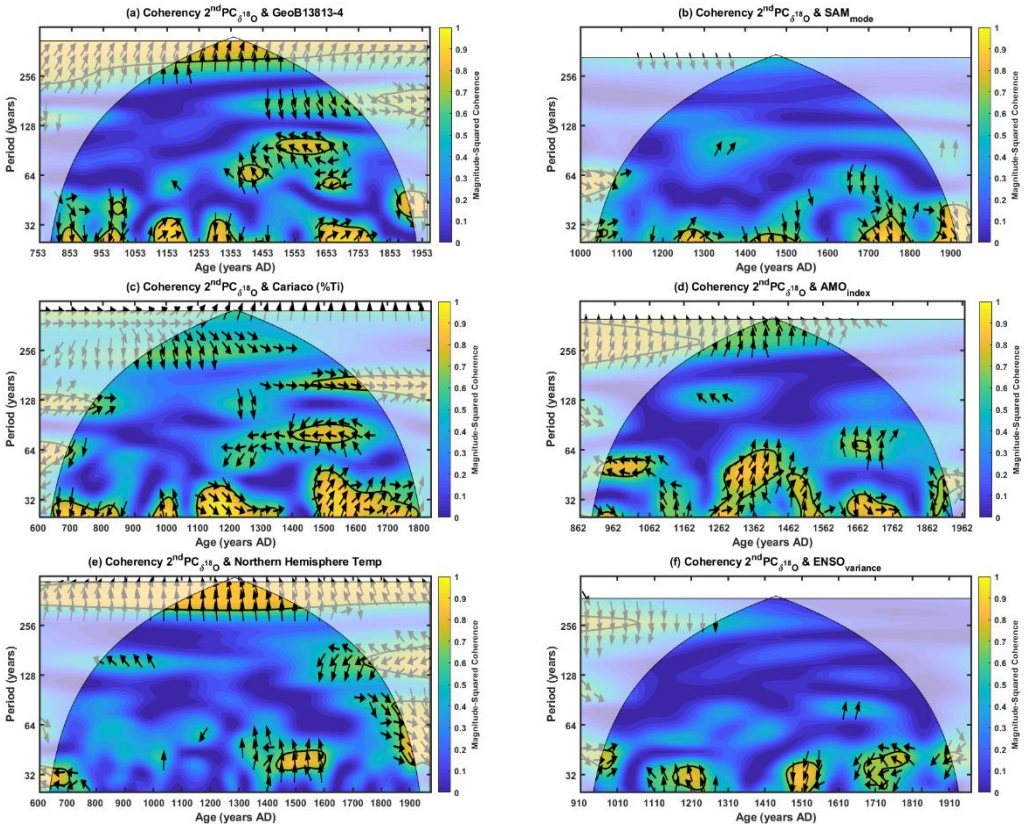

Figure A.5 *-The same as to the fig. A.3.2 but for the 2ndPC.*

A.4 – Empirical Mode Decomposition

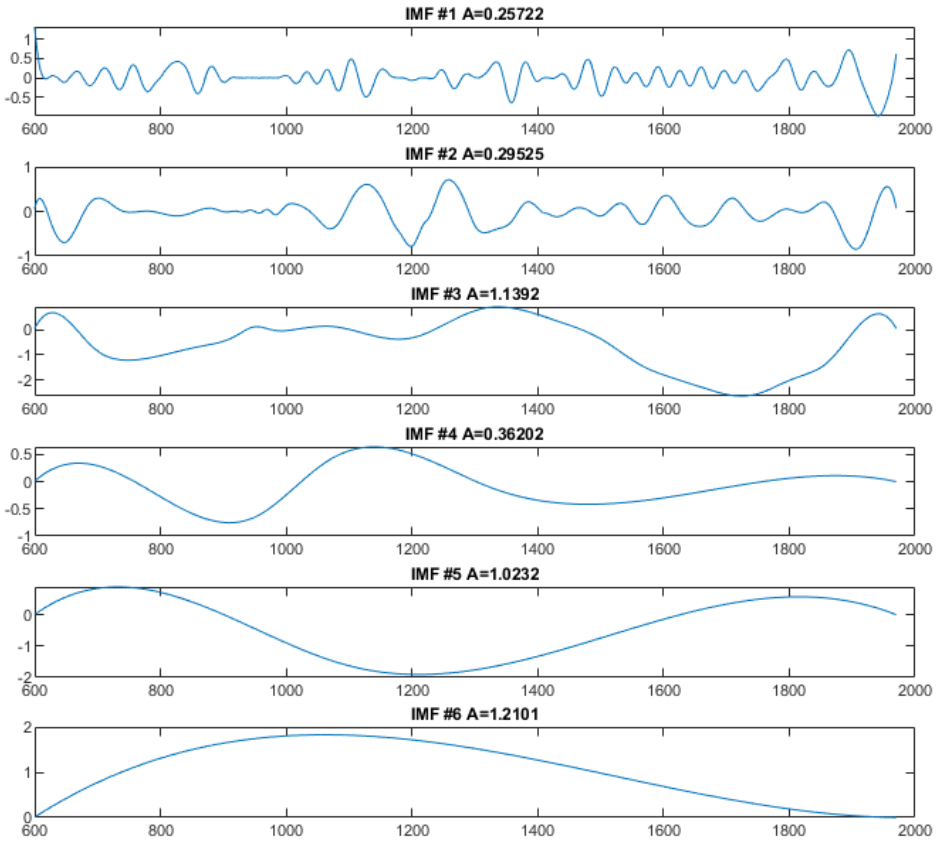

Figure. A.6 - Intrinsic Mode Functions for the 1st PC. The last component (bottom plot) represent the trend component and the others, the IMFs.

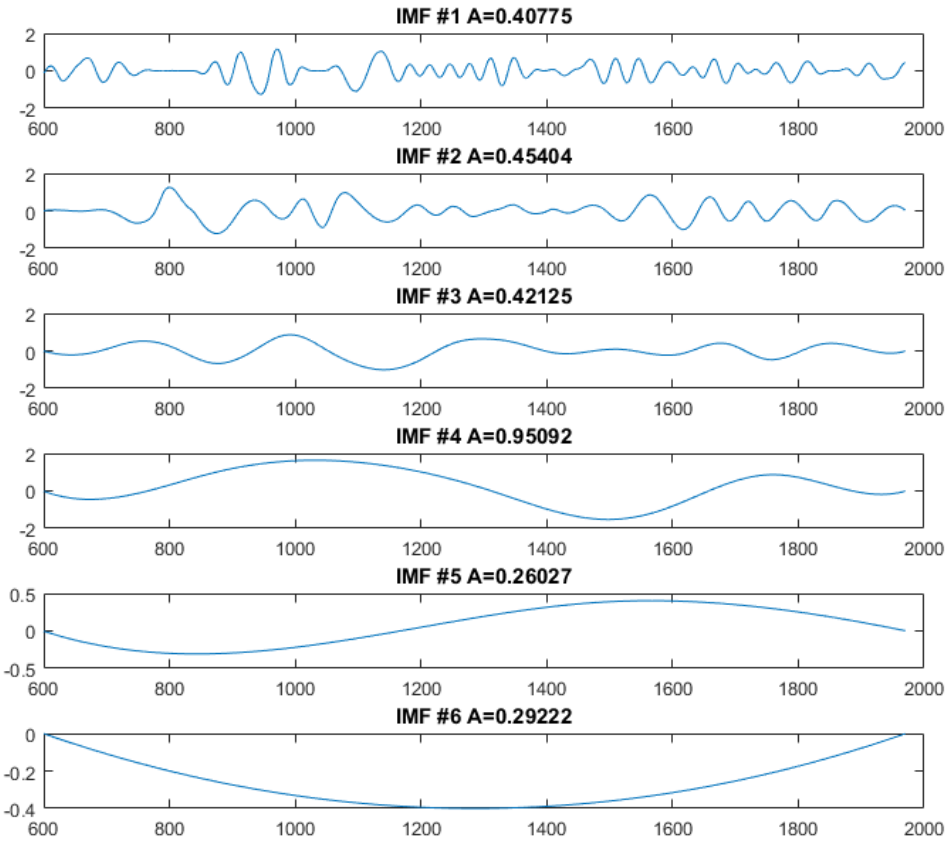

Figure A.7 - Intrinsic Mode Functions for the 2nd PC

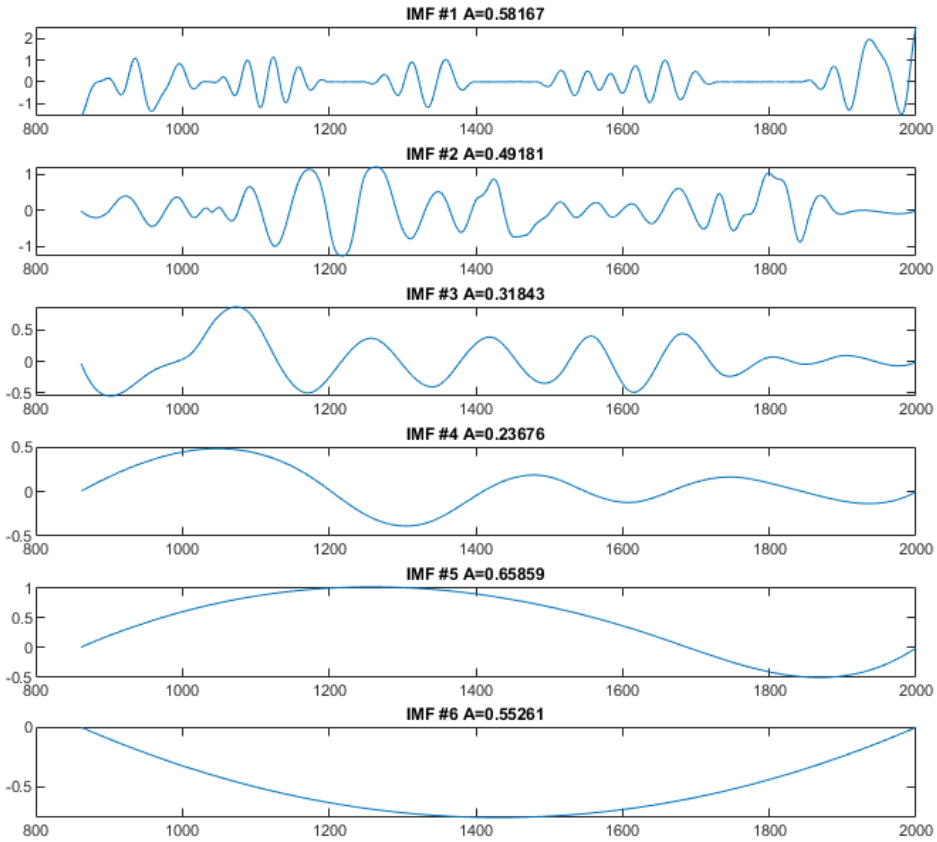

Figure A.8 - Intrinsic Mode Functions for the AMO index time series.

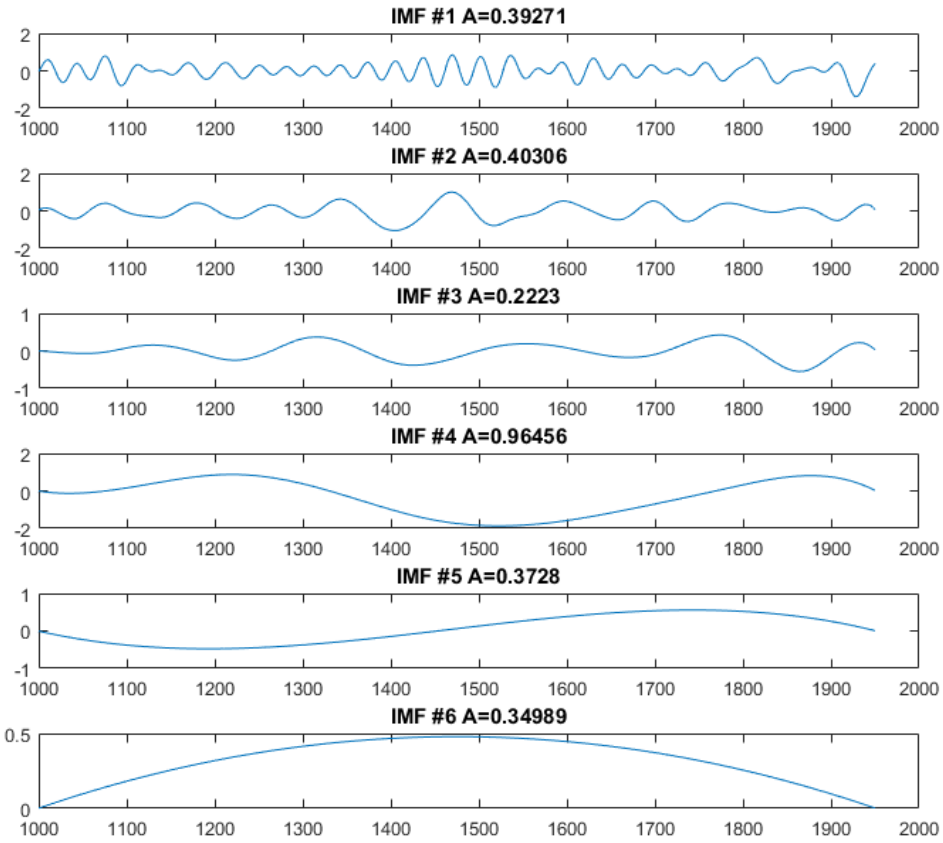

Figure A.9 - Intrinsic Mode Functions for the SAM time series.

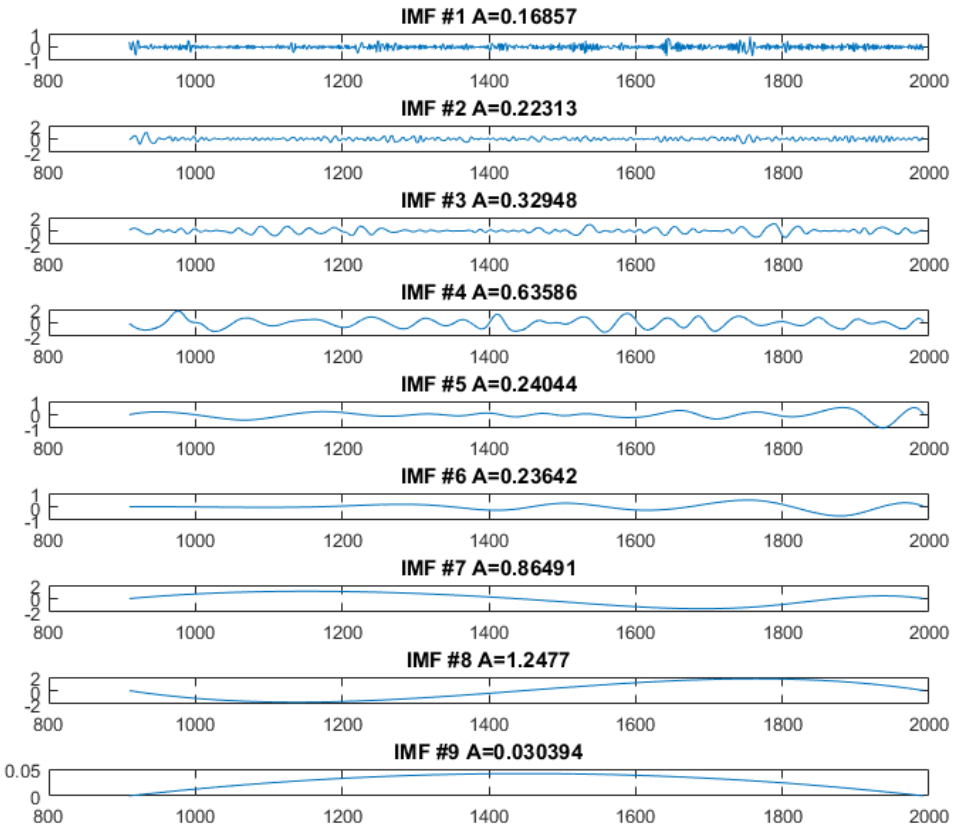

Figure. A.10 - intrinsic Mode Functions for the ENSO variance time series

A5. Biplot

The biplot graph consists of a scatter plot between the 1st and 2nd Principal Components. Classically in factor analysis, this type of plot is used to assess similarity between categorical variables often called of factors. The original biplot consists of a plot showing the factors or the eigenvectors (the explanatory variables), where the closer the angle between the eigenvectors, more correlated is the variables and the scores. For further details see Gabriel (1971).

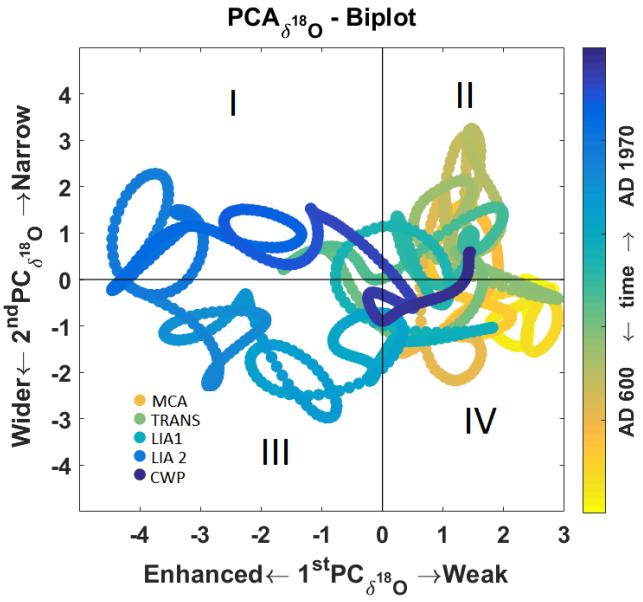

Figure A.11 – Biplot or scatter plot of the leading two Monte-Carlo Principal Component Analysis based on the proxy data. *The x axis represents the monsoon activity mode and the y axis represent the tripole SESA-SACZ-NEB mode or simply the SESA mode. The roman algorisms represent the quadrants of the biplot. The periods studied are represented by the assorted colours as showed in the legend on the left side inside the figure.*

A6. Paper Submitted to Geophysical Research Letters

Coherent South American Monsoon Variability during the Last Millennium Revealed through high-resolution proxy Records

J.L.P.S. Campos[1], F.W. Cruz[2], T. Ambrizi[1], M. Deininger[3]; M. Vuille[4]; V.F. Novello[2]; N.M. Strikis[5]

[1] Department of Atmospheric Sciences, Instituto de Astronomia Geofísica e Ciências Atmosféricas, Universidade de São Paulo

[2] Department of Sedimentary Geology,Instituto de Geociências, Universidade de São Paulo

[3] Institute of Geosciences, Johannes Gutenberg University Mainz, J.-J.-Becher-Weg 21, 55128 Mainz, Germany

[4]Department of Atmospheric and Environmental Sciences, University at Albany, State University of New York

[5]Department of Geochemistry, Universidade Federal Fluminense

Corresponding author: José Campos (jose.leandro.campos@usp.br) ; Francisco Cruz (cbill@usp.br); Tercio Ambrizzi (tercio.ambrizzi@iag.usp.br)

Key Points:

- The first compilation of 12 $\delta^{18}O$ and Sr/Ca time series based on multiproxy records across the Tropical South America is presented revealing two large-scale spatiotemporal variability modes of the South America Summer Monsoon during the last millennium

- The first leading Principal Component, representing the monsoon shows an enhanced monsoon during the LIA and weak during the MCA. The second mode representing the South Atlantic Low-Level Jet, reveals more activity during the early LIA period and seems related to the AMO.

- Composite analysis shows an enhancement and wider monsoon axis (SACZ) during the LIA rather than a southward displacement of the monsoon axis, contrasting to previous interpretations of the Last Millennium South America Summer Monsoon.

Abstract

The number of last millennia paleo-precipitation records from the South America Monsoon (SASM) domain have increased dramatically, allowing the identification of different precipitation regimes across the continent. However, most of these studies focus only on monsoon regional aspects, thereby neglecting its large spatio-temporal variability. Here, using Monte-Carlo Principal Component Analysis (MC-PCA). A compilation of 12 well-dated summer paleo-precipitation records across the tropical South America is presented. The 1stMC-PCA represents a see-saw pattern between the South Atlantic Convergence Zone (SACZ) on one side, and Northeastern Brazil (NEB) on the other. The 2ndMC-PCA forms a tri-pole between the descending branches of the SACZ over Southeastern South America (SESA) and NEB, respectively, and the core SACZ domain, consistent with rainfall anomalies during extreme South American Low-Level Jets (SALLJ) episodes. Composite analysis reveals an enhanced monsoon with a wider SACZ rather than a southward displaced SACZ during the Little Ice Age contrasting previous interpretations.

Plain Language Summary

The South America Summer Monsoon (SASM) and its subcomponents are responsible by more than 70% of the annual precipitation over the tropical South America domain. Due to data availability in Industrial Period (40 years), the variability on low frequency timescales of the SASM is a poorly known issue. In a changing climate the knowledge of the SASM variability in lower frequency time scales is crucial to a better understanding of the climate variability dominated just by natural forcings, to quantify anthropic climate change and validate Earth System Models such as PMIP/CMIP project. So here a compilation of 12 paleo-precipitation records that spans the last millennium, across the South America is presented revealing the multidecadal spatiotemporal variability of the monsoon and its subcomponents, such as the South Atlantic Convergence Zone (SACZ), South America Low Level Jets (SALJ) which impact the precipitation over the Southeast South America (SESA), Northeast of Brazil (NEB), eastern Amazonia and tropical Andes domains in two anomalous last millennia periods, the Little Ice Age (LIA) and the Medieval Climate Anomaly (MCA).

References

Anchukaitis, K. J., & Tierney, J. E. (2013). Identifying coherent spatiotemporal modes in time-uncertain proxy paleoclimate records. Climate dynamics, 41(5-6), 1291-1306, https://doi.org/10.1007/s00382-012-1483-0

Abram, N. J., McGregor, H. V., Tierney, J. E., Evans, M. N., McKay, N. P., Kaufman, D. S., ... & Steig, E. J. (2016). Early onset of industrial-era warming across the oceans and continents. *Nature*, *536*(7617), 411, https://doi.org/10.1038/nature19082

Abram, N. J., Mulvaney, R., Vimeux, F., Phipps, S. J., Turner, J., & England, M. H. (2014). Evolution of the Southern Annular Mode during the past millennium. *Nature Climate Change*, *4*(7), 564, https://doi.org/10.1038/nclimate2235

Ambrizzi, T., & Hoskins, B. J. (1997). Stationary Rossby-wave propagation in a baroclinic atmosphere. *Quarterly Journal of the Royal Meteorological Society*, *123*(540), 919-928, https://doi.org/10.1002/qj.49712354007

Apaéstegui, J., Cruz, F. W., Sifeddine, A., Vuille, M., Villar, J. C. E., Guyot, J. L., ... & Edwards, L. (2014). Hydroclimate variability of the northwestern Amazon Basin near the Andean foothills of Peru related to the South American Monsoon System during the last 1600 years. Climate of the Past, 10(6), 1967-1981, doi : 10.5194/cp-10-1967-2014

Benestad, R., Sillmann, J., Thorarinsdottir, T. L., Guttorp, P., Mesquita, M. D. S., Tye, M. R., ... & Parding, K. M. (2017). New vigour involving statisticians to overcome ensemble fatigue. Nature Climate Change, 7(10), 697, https://doi.org/10.1038/nclimate3393

Bernal, J. P., Cruz, F. W., Stríkis, N. M., Wang, X., Deininger, M., Catunda, M. C. A., ... & Auler, A. S. (2016). High-resolution Holocene South American monsoon history recorded by a speleothem from Botuverá Cave, Brazil. Earth and Planetary Science Letters, 450, 186-196, https://doi.org/10.1016/j.epsl.2016.06.008

Bird, B. W., Abbott, M. B., Vuille, M., Rodbell, D. T., Stansell, N. D., & Rosenmeier, M. F. (2011). A 2,300-year-long annually resolved record of the South American summer monsoon from the Peruvian Andes. Proceedings of the National Academy of Sciences, 108(21), 8583-8588, https://doi.org/10.1073/pnas.1003719108

Bombardi, R. J., Carvalho, L. M., Jones, C., & Reboita, M. S. (2014). Precipitation over eastern South America and the South Atlantic Sea surface temperature during neutral ENSO periods. Climate dynamics, 42(5-6), 1553-1568, https://doi.org/10.1007/s00382-013-1832-7

Bradley, R. S., Hughes, M. K., & Diaz, H. F. (2003). Climate in medieval time. *Science*, *302*(5644), 404-405.

Broecker, W. S. (2001). Was the medieval warm period global?. *Science*, *291*(5508), 1497-1499, https:// doi: 10.1126/science.291.5508.1497

Carvalho, L. M., Jones, C., & Liebmann, B. (2002). Extreme precipitation events in southeastern South America and large-scale convective patterns in the South Atlantic convergence zone. *Journal of Climate*, *15*(17), 2377-2394, *https://doi.org/10.1175/1520-0442(2002)015<2377:EPEISS>2.0.CO;2*

Carvalho, L. M., Jones, C., & Liebmann, B. (2004). The South Atlantic convergence zone: Intensity, form, persistence, and relationships with intraseasonal to interannual activity and extreme rainfall. Journal of Climate, 17(1), 88-108, https://doi.org/10.1175/1520-0442(2004)017<0088:TSACZI>2.0.CO;2

Carvalho, L. M., Jones, C., & Ambrizzi, T. (2005). Opposite phases of the Antarctic Oscillation and relationships with intraseasonal to interannual activity in the tropics during the austral summer. *Journal of climate*, *18*(5), 702-718, https://doi.org/10.1175/JCLI-3284.1

Cattell, R. B. (1966). The scree test for the number of factors. *Multivariate behavioral research*, *1*(2), 245-276, https://doi.org/10.1207/s15327906mbr0102_10

Chao, W. C. (2000). Multiple quasi equilibria of the ITCZ and the origin of monsoon onset. *Journal of the atmospheric sciences*, *57*(5), 641-652, *https://doi.org/10.1175/1520-0469(2000)057<0641:MQEOTI>2.0.CO;2*

Chaves, R. R., & Nobre, P. (2004). Interactions between sea surface temperature over the South Atlantic Ocean and the South Atlantic Convergence Zone. Geophysical Research Letters, 31(3), https://doi.org/10.1029/2003GL018647

Chen, T. C., Weng, S. P., & Schubert, S. (1999). Maintenance of austral summertime upper-tropospheric circulation over tropical South America: The Bolivian high–Nordeste low system. Journal of the atmospheric sciences, 56(13), 2081-2100, https://doi.org/10.1175/1520-0469(1999)056<2081:MOASUT>2.0.CO;2

Chiessi, C. M., Mulitza, S., Pätzold, J., Wefer, G., & Marengo, J. A. (2009). Possible impact of the Atlantic Multidecadal Oscillation on the South American summer monsoon. Geophysical Research Letters, 36(21), https://doi.org/10.1029/2009GL039914

Cook, E. R., Woodhouse, C. A., Eakin, C. M., Meko, D. M., & Stahle, D. W. (2004). Long-term aridity changes in the western United States. *Science*, *306*(5698), 1015-1018, DOI: 10.1126/science.1102586

Cruz, F. W., Vuille, M., Burns, S. J., Wang, X., Cheng, H., Werner, M., ... & Nguyen, H. (2009). Orbitally driven east–west antiphasing of South American precipitation. *Nature Geoscience*, *2*(3), 210, https://doi.org/10.1038/ngeo444

Daubechies, I. (1990). The wavelet transform, time-frequency localization and signal analysis. *IEEE transactions on information theory*, *36*(5), 961-1005, https://doi.org/10.1109/18.57199

Dätwyler, C., Neukom, R., Abram, N. J., Gallant, A. J., Grosjean, M., Jacques-Coper, M., ... & Villalba, R. (2018). Teleconnection stationarity, variability and trends of the Southern Annular Mode (SAM) during the last millennium. *Climate dynamics*, *51*(5-6), 2321-2339, https://doi.org/10.1007/s00382-017-4015-0

Dee, D. P., Uppala, S. M., Simmons, A. J., Berrisford, P., Poli, P., Kobayashi, S., ... & Bechtold, P. (2011). The ERA-Interim reanalysis: Configuration and performance of the data assimilation system. *Quarterly Journal of the royal meteorological society*, *137*(656), 553-597, https://doi.org/10.1002/qj.828

Deininger, M., McDermott, F., Mudelsee, M., Werner, M., Frank, N., & Mangini, A. (2017). Coherency of late Holocene European speleothem δ18O records linked to North Atlantic Ocean circulation. Climate Dynamics, 49(1-2), 595-618, https://doi.org/10.1007/s00382-016-3360-8

Deininger M (2013) The European holocene climate from the Speleothem's view, PhD thesis. Department of Physics and Astronomy, Faculty of Physics and Astronomy, University of Heidelberg. http://www.ub.uniheidelberg.de/archiv/16039, http://www.ub.uni-heidelberg.de/archiv/16039

Douglas, M. W., Maddox, R. A., Howard, K., & Reyes, S. (1993). The mexican monsoon. *Journal of Climate*, *6*(8), 1665-1677, *https://doi.org/10.1175/1520-0442(1993)006<1665:TMM>2.0.CO;2*

Eddy, J. (1976). The Maunder Minimum. *Science*, *192*(4245), 1189-1202. Retrieved from http://www.jstor.org/stable/1742583

Enfield, D. B., Mestas-Nuñez, A. M., & Trimble, P. J. (2001). The Atlantic multidecadal oscillation and its relation to rainfall and river flows in the continental US. *Geophysical Research Letters*, *28*(10), 2077-2080. https://doi.org/10.1029/2000GL012745

Fairchild, I. J., & Baker, A. (2012). *Speleothem science: from process to past environments* (Vol. 3). John Wiley & Sons.

Ferreira, N. J., Sanches, M., & SILVA, D. (2004). MAF Composição da Zona de Convergência do Atlântico Sul em períodos de El Niño e La Niña. *Revista Brasileira de Meteorologia*, *19*(1), 89-98.

Foufoula-Georgiou, E., Kumar, P., Mukerji, T., & Mavko, G. (1995). Wavelets in geophysics. *Pure and Applied Geophysics*, *145*(2), 374-375.

Gabriel, K. R. (1971). The biplot graphic display of matrices with application to principal component analysis. *Biometrika*, *58*(3), 453-467. https://doi.org/10.1093/biomet/58.3.453

Gan, M. A., Kousky, V. E., & Ropelewski, C. F. (2004). The South America monsoon circulation and its relationship to rainfall over west-central Brazil. *Journal of climate*, *17*(1), 47-66, *https://doi.org/10.1175/1520-0442(2004)017<0047:TSAMCA>2.0.CO;2*

Garreaud, R. D., Vuille, M., Compagnucci, R., & Marengo, J. (2009). Present-day south american climate. Palaeogeography, Palaeoclimatology, Palaeoecology, 281(3-4), 180-195, https://doi.org/10.1016/j.palaeo.2007.10.032

Garreaud, R., Vuille, M., & Clement, A. C. (2003). The climate of the Altiplano: observed current conditions and mechanisms of past changes. Palaeogeography, palaeoclimatology, palaeoecology, 194(1-3), 5-22, https://doi.org/10.1016/S0031-0182(03)00269-4

Gonfiantini, R. (1978). Standards for stable isotope measurements in natural compounds. *Nature*, *271*(5645), 534, https://doi.org/10.1038/271534a0DO

Gillett, N. P., Kell, T. D., & Jones, P. D. (2006). Regional climate impacts of the Southern Annular Mode. *Geophysical Research Letters*, *33*(23), https://doi.org/10.1029/2006GL027721

Goswami, B. N., & Xavier, P. K. (2003). Potential predictability and extended range prediction of Indian summer monsoon breaks. *Geophysical Research Letters*, *30*(18), **https://doi.org/10.1029/2003GL017810**

Grinsted, A., Moore, J. C., & Jevrejeva, S. (2004). Application of the cross wavelet transform and wavelet coherence to geophysical time series. *Nonlinear processes in geophysics*, *11*(5/6), 561-566,

Haug, G. H., Hughen, K. A., Sigman, D. M., Peterson, L. C., & Röhl, U. (2001). Southward migration of the intertropical convergence zone through the Holocene. Science, 293(5533), 1304-1308, doi: 10.1126/science.1059725

Hoskins, B. J., & Ambrizzi, T. (1993). Rossby wave propagation on a realistic longitudinally varying flow. Journal of the Atmospheric Sciences, 50(12), 1661-1671, https://doi.org/10.1175/1520-0469(1993)050<1661:RWPOAR>2.0.CO;2

Hotelling, H. (1933). Analysis of a complex of statistical variables into principal components. *Journal of educational psychology*, *24*(6), 417, https://psycnet.apa.org/doi/10.1037/h0071325

Hurley, J. V., Vuille, M., & Hardy, D. R. (2016). Forward modeling of δ18O in Andean ice cores. Geophysical Research Letters, 43(15), 8178-8188, https://doi.org/10.1002/2016GL070150

Hurley, J. V., Vuille, M., Hardy, D. R., Burns, S. J., & Thompson, L. G. (2015). Cold air incursions, δ18O variability, and monsoon dynamics associated with snow days at Quelccaya Ice Cap, Peru. Journal of Geophysical Research: Atmospheres, 120(15), 7467-7487, https://doi.org/10.1002/2015JD023323

Huang, N. E., Shen, Z., Long, S. R., Wu, M. C., Shih, H. H., Zheng, Q., ... & Liu, H. H. (1998). The empirical mode decomposition and the Hilbert spectrum for nonlinear and non-stationary time series analysis. *Proceedings of the Royal Society of London. Series A: Mathematical, Physical and Engineering Sciences*, *454*(1971), 903-995, https://doi.org/10.1098/rspa.1998.0193

Jones, C., & Carvalho, L. M. (2018). The influence of the Atlantic multidecadal oscillation on the eastern Andes low-level jet and precipitation in South America. npj Climate and Atmospheric Science, 1(1), 40, https://doi.org/10.1038/s41612-018-0050-8

Jorgetti, T., da Silva Dias, P. L., & de Freitas, E. D. (2014). The relationship between South Atlantic SST and SACZ intensity and positioning. Climate dynamics, 42(11-12), 3077-3086, https://doi.org/10.1007/s00382-013-1998-z

Jungclaus, J., Bard, E., Baroni, M., Braconnot, P., Cao, J., Chini, L., ... & Hurtt, G. (2017). The PMIP4 contribution to CMIP6–Part 3: The last millennium, scientific objective, and experimental design for the PMIP4 past1000 simulations. Geoscientific Model Development Discussions, 10(11), 4005-4033, doi : 10.5194/gmd-10-4005-2017

Kanner, L. C., Burns, S. J., Cheng, H., Edwards, R. L., & Vuille, M. (2013). High-resolution variability of the South American summer monsoon over the last seven millennia: insights from a speleothem record from the central Peruvian Andes. Quaternary Science Reviews, 75, 1-10, https://doi.org/10.1016/j.quascirev.2013.05.008

Kayano, M. T., Capistrano, V. B., Andreoli, R. V., & de Souza, R. A. (2016). A further analysis of the tropical Atlantic SST modes and their relations to north-eastern Brazil rainfall during different phases of Atlantic Multidecadal Oscillation. *International Journal of Climatology*, *36*(12), 4006-4018, https://doi.org/10.1002/joc.4610

Kaiser, H. F. (1960). The application of electronic computers to factor analysis. *Educational and psychological measurement*, *20*(1), 141-151, https://doi.org/10.1177%2F001316446002000116

Killick, R., Fearnhead, P., & Eckley, I. A. (2012). Optimal detection of changepoints with a linear computational cost. *Journal of the American Statistical Association*, *107*(500), 1590-1598, https://doi.org/10.1080/01621459.2012.737745

Knight, J. R., Folland, C. K., & Scaife, A. A. (2006). Climate impacts of the Atlantic multidecadal oscillation. *Geophysical Research Letters*, *33*(17), https://doi.org/10.1029/2006GL026242

Kodama, Y. (1992). Large-scale common features of subtropical precipitation zones (the Baiu frontal zone, the SPCZ, and the SACZ) Part I: Characteristics of subtropical frontal zones. Journal of the Meteorological Society of Japan. Ser. II, 70(4), 813-836, https://doi.org/10.2151/jmsj1965.70.4_813

Lachniet, M. S., & Patterson, W. P. (2006). Use of correlation and stepwise regression to evaluate physical controls on the stable isotope values of Panamanian rain and surface waters. *Journal of Hydrology*, *324*(1-4), 115-140, https://doi.org/10.1016/j.jhydrol.2005.09.018

Laloyaux, P., de Boisseson, E., Balmaseda, M., Bidlot, J. R., Broennimann, S., Buizza, R., ... & Kosaka, Y. (2018). CERA-20C: A coupled reanalysis of the Twentieth Century. Journal of Advances in Modeling Earth Systems, https://doi.org/10.1029/2018MS001273

Lavielle, M. (2005). Using penalized contrasts for the change-point problem. Signal processing, 85(8), 1501-1510, https://doi.org/10.1016/j.sigpro.2005.01.012

Lechleitner, F. A., Breitenbach, S. F., Rehfeld, K., Ridley, H. E., Asmerom, Y., Prufer, K. M., ... & Polyak, V. (2017). Tropical rainfall over the last two millennia: evidence for a low-latitude hydrologic seesaw. Scientific Reports, 7, 45809, https://doi.org/10.1038/srep45809

LeGrande, A. N., & Schmidt, G. A. (2006). Global gridded data set of the oxygen isotopic composition in seawater. *Geophysical research letters*, *33*(12), **https://doi.org/10.1029/2006GL026011**

Li, J., Xie, S. P., Cook, E. R., Huang, G., D'arrigo, R., Liu, F., ... & Zheng, X. T. (2011). Interdecadal modulation of El Niño amplitude during the past millennium. *Nature Climate Change*, *1*(2), 114, https://doi.org/10.1038/nclimate1086

Liebmann, B., Kiladis, G. N., Vera, C. S., Saulo, A. C., & Carvalho, L. M. (2004). Subseasonal variations of rainfall in South America in the vicinity of the low-level jet east of the Andes and comparison to those in the South Atlantic convergence zone. *Journal of climate*, *17*(19), 3829-3842, https://doi.org/10.1175/1520-0442(2004)017%3C3829:SVORIS%3E2.0.CO;2

Lenters, J. D., & Cook, K. H. (1999). Summertime precipitation variability over South America: Role of the large-scale circulation. Monthly Weather Review, 127(3), 409-431. https://doi.org/10.1175/1520-0493(1999)127<0409:SPVOSA>2.0.CO;2

Lorenz, E. N. (1956). Empirical orthogonal functions and statistical weather prediction,

Ma, H. Y., Ji, X., Neelin, J. D., & Mechoso, C. R. (2011). Mechanisms for precipitation variability of the eastern Brazil/SACZ convective margin. Journal of Climate, 24(13), 3445-3456, https://doi.org/10.1175/2011JCLI4070.1

Manjula, M., & Sarma, A. V. R. S. (2012). Comparison of empirical mode decomposition and wavelet based classification of power quality events. *Energy Procedia*, *14*, 1156-1162, https://doi.org/10.1016/j.egypro.2011.12.1069

Mann, M. E. (2001). Climate during the past millennium. *Weather*, *56*(3), 91-102, DOI: 10.1002/j.1477-8696.2001.tb06542.x

Mann, M. E., Cane, M. A., Zebiak, S. E., & Clement, A. (2005). Volcanic and solar forcing of the tropical Pacific over the past 1000 years. *Journal of Climate*, *18*(3), 447-456, *https://doi.org/10.1175/JCLI-3276.1*

Mann, M. E., & Jones, P. D. (2003). Global surface temperatures over the past two millennia. *Geophysical Research Letters*, *30*(15), https://doi.org/10.1029/2003GL017814

Marengo, J. A., Liebmann, B., Grimm, A. M., Misra, V., Silva Dias, P. L., Cavalcanti, I. F. A., ... & Saulo, A. C. (2012). Recent developments on the South American monsoon system. International Journal of Climatology, 32(1), 1-21, https://doi.org/10.1002/joc.2254

Marengo, J. A., Soares, W. R., Saulo, C., & Nicolini, M. (2004). Climatology of the low-level jet east of the Andes as derived from the NCEP–NCAR reanalyses: Characteristics and temporal variability, https://doi.org/10.1175/1520-0442(2004)017<2261:COTLJE>2.0.CO;2

Miller, G. H., and Coauthors, 2012: Abrupt onset of the Little Ice Age triggered by volcanism and sustained by sea-ice/ocean feedbacks. *Geophys. Res. Lett.*, **39**, L02708, https://doi.org/10.1029/2011GL050168

Mo, K. C., & Higgins, R. W. (1998). The Pacific–South American modes and tropical convection during the Southern Hemisphere winter. *Monthly Weather*

Review, *126*(6), 1581-1596, https://doi.org/10.1175/1520-0493(1998)126%3C1581:TPSAMA%3E2.0.CO;2

Moberg, A., Sonechkin, D. M., Holmgren, K., Datsenko, N. M., & Karlén, W. (2005). Highly variable Northern Hemisphere temperatures reconstructed from low-and high-resolution proxy data. *Nature*, *433*(7026), 613, https://doi.org/10.1038/nature03265

Muza, M. N., Carvalho, L. M., Jones, C., & Liebmann, B. (2009). Intraseasonal and interannual variability of extreme dry and wet events over southeastern South America and the subtropical Atlantic during austral summer. Journal of Climate, 22(7), 1682-1699, https://doi.org/10.1175/2008JCLI2257.1

Muscheler, R., Joos, F., Beer, J., Müller, S. A., Vonmoos, M., & Snowball, I. (2007). Solar activity during the last 1000 yr inferred from radionuclide records. *Quaternary Science Reviews*, *26*(1-2), 82-97, https://doi.org/10.1016/j.quascirev.2006.07.012

North, G. R., Bell, T. L., Cahalan, R. F., & Moeng, F. J. (1982). Sampling errors in the estimation of empirical orthogonal functions. Monthly Weather Review, 110(7), 699-706, https://doi.org/10.1175/1520-0493(1982)110<0699:SEITEO>2.0.CO;2

Novello, V. F., Cruz, F. W., Moquet, J. S., Vuille, M., de Paula, M. S., Nunes, D., ... & Stríkis, N. M. (2018). Two millennia of South Atlantic Convergence Zone variability reconstructed from isotopic proxies. Geophysical Research Letters, https://doi.org/10.1029/2017GL076838

Novello, V. F., Vuille, M., Cruz, F. W., Stríkis, N. M., De Paula, M. S., Edwards, R. L., ... & Hartmann, G. A. (2016). Centennial-scale solar forcing of the South American Monsoon System recorded in stalagmites. Scientific reports, 6, 24762, https://doi.org/10.1038/srep24762

Novello, V. F., Cruz, F. W., Karmann, I., Burns, S. J., Stríkis, N. M., Vuille, M., ... & Barreto, E. A. (2012). Multidecadal climate variability in Brazil's Nordeste during the last 3000 years based on speleothem isotope records. Geophysical Research Letters, 39(23), https://doi.org/10.1029/2012GL053936

Otterå, O. H., Bentsen, M., Drange, H., & Suo, L. (2010). External forcing as a metronome for Atlantic multidecadal variability. *Nature Geoscience*, *3*(10), 688, https://doi.org/10.1038/ngeo955

Parsons, L. A., Yin, J., Overpeck, J. T., Stouffer, R. J., & Malyshev, S. (2014). Influence of the Atlantic Meridional Overturning Circulation on the monsoon rainfall and carbon balance of the American tropics. Geophysical Research Letters, 41(1), 146-151, https://doi.org/10.1002/2013GL058454

Pearson, K. (1901). Principal components analysis. *The London, Edinburgh, and Dublin Philosophical Magazine and Journal of Science*, *6*(2), 559,

Perez, L., García-Rodríguez, F., & Hanebuth, T. J. (2016). Variability in terrigenous sediment supply offshore of the Río de la Plata (Uruguay) recording the continental climatic history over the past 1200 years. Climate of the Past, 12(3), 623-634, https://doi.org/10.5194/cp-12-623-2016

Preisendorfer, R. W., & Mobley, C. D. (1982). Data intercomparison theory. II. Trinity statistics for location, spread and pattern differences,

Preisendorfer, R. Ä. N. Ü. (1988). Principal component analysis in meteorology and oceanography. *Elsevier Sci. Publ.*, *17*, 425.

Prieto, G. A., Parker, R. L., & Vernon III, F. L. (2009). A Fortran 90 library for multitaper spectrum analysis. *Computers & Geosciences*, *35*(8), 1701-1710, https://doi.org/10.1016/j.cageo.2008.06.007

Rao, G. V., & Erdogan, S. (1989). The atmospheric heat source over the Bolivian plateau for a mean January. *Boundary-Layer Meteorology*, *46*(1-2), 13-33, https://doi.org/10.1007/BF00118444

Ramage, C. S. (1971). *Monsoon meteorology* (No. 551.518 R3).

Reboita, M. S., Da Rocha, R. P., Ambrizzi, T., & Caetano, E. (2010). An assessment of the latent and sensible heat flux on the simulated regional climate over Southwestern South Atlantic Ocean. *Climate dynamics*, *34*(6), 873-889, https://doi.org/10.1007/s00382-009-0681-x

Robock, A., & Mao, J. (1995). The volcanic signal in surface temperature observations. *Journal of Climate*, *8*(5), 1086-1103, *https://doi.org/10.1175/1520-0442(1995)008<1086:TVSIST>2.0.CO;2*

Rodionov, S. N. (2004). A sequential algorithm for testing climate regime shifts. *Geophysical Research Letters*, *31*(9), https://doi.org/10.1029/2004GL019448

Rogers, J. C., & Van Loon, H. (1982). Spatial variability of sea level pressure and 500 mb height anomalies over the Southern Hemisphere. *Monthly Weather Review*, *110*(10), 1375-1392, https://doi.org/10.1175/1520-0493(1982)110%3C1375:SVOSLP%3E2.0.CO;2

Salio, P., Nicolini, M., & Zipser, E. J. (2007). Mesoscale convective systems over southeastern South America and their relationship with the South American low-level jet. Monthly Weather Review, 135(4), 1290-1309, https://doi.org/10.1175/MWR3305.1

Saltzman, B. (2001). *Dynamical paleoclimatology: generalized theory of global climate change* (Vol. 80). Elsevier.

Sharp, Z. D., Barnes, J. D., Brearley, A. J., Chaussidon, M., Fischer, T. P., & Kamenetsky, V. S. (2007). Chlorine isotope homogeneity of the mantle, crust and carbonaceous chondrites. *Nature*, *446*(7139), 1062, https://doi.org/10.1038/nature05748

Schneider, T., Bischoff, T., & Haug, G. H. (2014). Migrations and dynamics of the intertropical convergence zone. *Nature*, *513*(7516), 45, https://doi.org/10.1038/nature13636

Silva, V. B., & Berbery, E. H. (2006). Intense rainfall events affecting the La Plata Basin. Journal of Hydrometeorology, 7(4), 769-787, Silva, V. B., & Berbery, E. H. (2006). Intense rainfall events affecting the La Plata Basin. Journal of Hydrometeorology, 7(4), 769-787, https://doi.org/10.1175/JHM520.1

da Silva, A. E., & de Carvalho, L. M. V. (2007). Large-scale index for South America Monsoon (LISAM). Atmospheric Science Letters, 8(2), 51-57, https://doi.org/10.1002/asl.150

Silvestri, G. E., & Vera, C. S. (2003). Antarctic Oscillation signal on precipitation anomalies over southeastern South America. *Geophysical Research Letters*, *30*(21), https://doi.org/10.1029/2003GL018277

Schleussner, C. F., & Feulner, G. (2013). A volcanically triggered regime shift in the subpolar North Atlantic Ocean as a possible origin of the Little Ice Age. *Climate of the Past*, *9*(3), https://doi.org/10.5194/cp-9-1321-2013

Shindell, D. T., Schmidt, G. A., Mann, M. E., Rind, D., & Waple, A. (2001). Solar forcing of regional climate change during the Maunder Minimum. *Science*, *294*(5549), 2149-2152, DOI: 10.1126/science.1064363

Schurer, A. P., Tett, S. F., & Hegerl, G. C. (2014). Small influence of solar variability on climate over the past millennium. *Nature Geoscience*, *7*(2), 104, https://doi.org/10.1038/ngeo2040

Schulz, M., & Mudelsee, M. (2002). REDFIT: estimating red-noise spectra directly from unevenly spaced paleoclimatic time series. *Computers & Geosciences*, *28*(3), 421-426, https://doi.org/10.1016/S0098-3004(01)00044-9

Slawinska, J., & Robock, A. (2018). Impact of volcanic eruptions on decadal to centennial fluctuations of Arctic sea ice extent during the last millennium and on initiation of the Little Ice Age. *Journal of Climate*, *31*(6), 2145-2167, *https://doi.org/10.1175/JCLI-D-16-0498.1*

Stevenson, S., Otto-Bliesner, B., Fasullo, J., & Brady, E. (2016). "El Niño like" hydroclimate responses to last millennium volcanic eruptions. *Journal of Climate*, *29*(8), 2907-2921, *https://doi.org/10.1175/JCLI-D-15-0239.1*

Steinhilber, F., Abreu, J. A., & Beer, J. (2008). Solar modulation during the Holocene. *Astrophysics and Space Sciences Transactions*, *4*(1), 1-6, doi:10.5194/astra-4-1-2008

Stine, S. (1994). Extreme and persistent drought in California and Patagonia during mediaeval time. *Nature*, *369*(6481), 546, https://doi.org/10.1038/369546a0

Swingedouw, D., Terray, L., Cassou, C., Voldoire, A., Salas-Mélia, D., & Servonnat, J. (2011). Natural forcing of climate during the last millennium: fingerprint of solar variability. *Climate Dynamics*, *36*(7-8), 1349-1364, https://doi.org/10.1007/s00382-010-0803-5

Thompson, L. G., Mosley-Thompson, E., Davis, M. E., Zagorodnov, V. S., Howat, I. M., Mikhalenko, V. N., & Lin, P. N. (2013). Annually resolved ice core records of tropical climate variability over the past~ 1800 years. Science, 340(6135), 945-950, DOI: 10.1126/science.1234210

Thomson, D. J. (1982). Spectrum estimation and harmonic analysis. *Proceedings of the IEEE*, *70*(9), 1055-1096, https://doi.org/10.1109/PROC.1982.12433

Torrence, C., & Compo, G. P. (1998). A practical guide to wavelet analysis. *Bulletin of the American Meteorological society*, *79*(1), 61-78, *https://doi.org/10.1175/1520-0477(1998)079<0061:APGTWA>2.0.CO;2*

Torrence, C., & Webster, P. J. (1999). Interdecadal changes in the ENSO–monsoon system. *Journal of climate*, *12*(8), 2679-2690, https://doi.org/10.1175/1520-0442(1999)012%3C2679:ICITEM%3E2.0.CO;2

Toohey, M., & Sigl, M. (2017). Volcanic stratospheric sulfur injections and aerosol optical depth from 500 BCE to 1900 CE. *Earth System Science Data*, *9*(2), 809-831, https://doi.org/10.5194/essd-9-809-2017

Usoskin, I. G., Hulot, G., Gallet, Y., Roth, R., Licht, A., Joos, F., ... & Khokhlov, A. (2014). Evidence for distinct modes of solar activity. *Astronomy & Astrophysics*, *562*, L10,

Utida, G.,et al. "Tropical South Atlantic influence on Northeastern Brazil precipitation and ITCZ displacement during the past 2,300 years". Scientific Reports(2019): in press

Van Der Wiel, K., Matthews, A. J., Stevens, D. P., & Joshi, M. M. (2015). A dynamical framework for the origin of the diagonal South Pacific and South Atlantic convergence zones. *Quarterly Journal of the Royal Meteorological Society*, *141*(691), 1997-2010, **https://doi.org/10.1002/qj.2508**

Villalba, R. (1994). Tree-ring and glacial evidence for the Medieval Warm Epoch and the Little Ice Age in southern South America. In *The Medieval Warm Period* (pp. 183-197). Springer, Dordrecht, https://doi.org/10.1007/978-94-011-1186-7_4

Vuille, M., Burns, S. J., Taylor, B. L., Cruz, F. W., Bird, B. W., Abbott, M. B., ... & Novello, V. F. (2012). A review of the South American monsoon history as recorded in stable isotopic proxies over the past two millennia. Climate of the Past, 8(4), 1309-1321, https://doi.org/10.5194/cp-8-1309-2012

Vuille, M., & Werner, M. (2005). Stable isotopes in precipitation recording South American summer monsoon and ENSO variability: observations and model results. Climate Dynamics, 25(4), 401-413, https://doi.org/10.1007/s00382-005-0049-9

Waliser, D. E., & Gautier, C. (1993). A satellite-derived climatology of the ITCZ. *Journal of climate*, *6*(11), 2162-2174, *https://doi.org/10.1175/1520-0442(1993)006<2162:ASDCOT>2.0.CO;2*

Wang, X., Edwards, R. L., Auler, A. S., Cheng, H., Kong, X., Wang, Y., ... & Chiang, H. W. (2017). Hydroclimate changes across the Amazon lowlands over the past 45,000 years. Nature, 541(7636), 204, https://doi.org/10.1038/nature20787

Wang, B., & Ding, Q. (2006). Changes in global monsoon precipitation over the past 56 years. *Geophysical Research Letters*, *33*(6), **https://doi.org/10.1029/2005GL025347**

Webster, P. J., Magana, V. O., Palmer, T. N., Shukla, J., Tomas, R. A., Yanai, M. U., & Yasunari, T. (1998). Monsoons: Processes, predictability, and the prospects for prediction. *Journal of Geophysical Research: Oceans*, *103*(C7), 14451-14510, **https://doi.org/10.1029/97JC02719**

Wilks, D. S. (2011). *Statistical methods in the atmospheric sciences* (Vol. 100). Academic press.

Wortham, B. E., Wong, C. I., Silva, L. C., McGee, D., Montañez, I. P., Rasbury, E. T., ... & Santos, R. V. (2017). Assessing response of local moisture conditions in central Brazil to variability in regional monsoon intensity using speleothem 87 Sr/86 Sr values. Earth and Planetary Science Letters, 463, 310-322, https://doi.org/10.1016/j.epsl.2017.01.034

Enfield, D. B., Mestas-Nuñez, A. M., & Trimble, P. J. (2001). The Atlantic multidecadal oscillation and its relation to rainfall and river flows in the continental US. *Geophysical Research Letters*, *28*(10), 2077-2080, https://doi.org/10.1029/2000GL012745

Zhou, J. and K. Lau, 1998: Does a Monsoon Climate Exist over South America?. J. Climate, 11, 1020–1040, https://doi.org/10.1175/1520-0442(1998)011<1020:DAMCEO>2.0.CO;2